Global multiple-frequency seismic tomography using teleseismic and core-diffracted body waves

Kasra Hosseini

München 2016

Global multiple-frequency seismic tomography using teleseismic and core-diffracted body waves

Kasra Hosseini

Dissertation
an der Fakultät für Geowissenschaften
der Ludwig–Maximilians–Universität
München

vorgelegt von
Kasra Hosseini
aus Teheran, Iran

München, den 29.03.2016

Erstgutachter: Prof. Dr. Heiner Igel
Zweitgutachter: Prof. Dr. Karin Sigloch
Tag der mündlichen Prüfung: 30.05.2016

Summary

Seismic tomography is the pre-eminent tool for imaging the Earth's interior. Since the advent of this method in the 1980's, the internal structure of Earth has been vastly sampled and imaged at a variety of scales, and the resulting models have served as the primary means to investigate the processes driving our planet. Significant recent advances in seismic data acquisition and computing power have drastically progressed tomographic methods. Broad-band seismic waveforms can now be simulated up to the highest naturally occurring frequencies and consequently, measurement techniques can exploit seismic waves in their entire usable spectrum and in multiple frequencies.

This dissertation revolves around aspects of global multiple-frequency seismic tomography, from retrieving and processing of large seismological data sets to explore the multi-scale structure of the earth. The centrepiece of this work is an efficient processing strategy to assemble the largest possible data sets for waveform-based tomographic inversions. Motivated by the complex but loosely-constrained structure of the lowermost mantle, we aim to increase the spatial resolution and coverage of the mantle in all depths by extracting a maximum of information from observed seismograms.

We first present a method that routinely measures finite-frequency traveltimes of Pdiff waves by cross-correlating observed waveforms with synthetic seismograms across the broad-band frequency range. Large volumes of waveform data of $\approx$ 2000 earthquakes are retrieved and pre-processed using fully automatic software built for this purpose. Synthetic seismograms for these earthquakes are calculated by semi-analytical wave propagation through a spherically symmetric earth model, to 1 Hz dominant frequency. This way, we construct one of the largest core-diffracted P wave traveltime collections so far with a total of 479,559 traveltimes in frequency passbands ranging from 30.0 to 2.7 s dominant period. Projected onto their core-grazing ray segments, the Pdiff observations recover major structural, lower-mantle heterogeneities known from existing global mantle models.

An inversion framework with adaptive parameterisation and locally-adjusted regularisation is developed to accurately map the information of this data set onto the desired model parameters. This broad-band waveform inversion

seamlessly incorporates the Pdiff measurements alongside a very large data set of conventional teleseismic P and PP measurements. We obtain structural heterogeneities of considerable detail in all mantle depths. The mapped features confirm several previously imaged structures. At the same time, sharper outlines for several subduction systems (e.g., Tethyan, Aegean and Farallon slabs) and uprising mantle plumes (e.g., Iceland, Afar and Tristan da Cunha) appear in our model. We trace some of these features throughout the mantle to investigate their morphological characteristics in a large (whole-mantle) context. Moreover, we report the structural findings revealed by our model. This ranges from geometries of slab complexes and subdivisions of Large Low Shear Velocity Provinces at the root of the mantle to tomographic evidence to support the existence of deep-mantle plumes beneath Iceland and Tristan da Cunha.

Zusammenfassung

Seismische Tomographie ist die führende Vorgehensweise um das Erdinnere zu visualisieren. Die Erde wurde seit der Einführung dieser Methode in den 1980er Jahren großräumig in verschiedensten Tiefen und Skalen dargestellt. Die resultierenden Erdmodelle dienten seit dem als Grundlage um die treibenden Kräfte in der Erde zu untersuchen. Jüngste Fortschritte in der seismischen Datenerfassung und zunehmende Rechenleistung haben tomographische Modelle dramatisch verbessert. Breitbandige seismische Wellenformen können nun bis zu den höchsten natürlich vorkommenden Frequenzen simuliert werden. Seismische Wellen werden folglich in ihrem gesamten nutzbaren Spektrum und in mehreren Frequenzen genutzt.

Diese Dissertation beschäftigt sich mit globaler seismischer Tomographie in mehreren Frequenzbändern, beginnend mit dem Herunterladen und Bearbeiten der Daten bis hin zur Beschreibung des Erdinneren auf verschiedenen Skalen. Das Herzstück der Arbeit ist eine effiziente Strategie, möglichst große Datensätze für Wellenformtomographie zu sammeln. Motiviert von der komplexen und weithin unterbestimmten Struktur des tiefen Erdmantels, zielt die Arbeit darauf ab, die räumliche Auflösung und Abdeckung des gesamten Mantels durch maximale Ausnutzung des Informationsgehalts von Seismogrammen zu erhöhen.

Zunächst präsentieren wir eine Methode zur automatisierten Messung der Laufzeiten von Pdiff Phasen, mittels Kreuzkorrelation mit synthetischen Seismogrammen in mehreren Frequenzbändern. Anhand einer eigens entwickelten Software wurden Seismogramme von über 2000 Erdbeben vollautomatisch heruntergeladen und prozessiert. Synthetische Seismogramme (bis zu 1 Hertz dominante Frequenz) wurden mittels einer semianalytischen Methode in einem kugelsymmetrischen Erdmodell berechnet. Aus der Kreuzkorrelation erhielten wir den bisher größten Datensatz von insgesamt 479.559 Pdiff Laufzeiten, aufgeteilt in Passbänder zwischen 30 und 2.7 Sekunden. Bereits eine erste Auswertung, bei der nur die Laufzeitdifferenzen auf die Kern-Mantel-Grenze abgebildet werden, zeigt großskalige Strukturen, die mit bestehenden globalen Mantel-Modellen übereinstimmen.

Ein Inversionsschema wurde entwickelt, inklusive adaptiver Parametrisierung und lokaler Regularisierung, um die Daten auf ein Mantelmodell abzubilden. Die Inversion breitbandiger Wellenformen integriert Pdiff Messungen in einen sehr großen Datensatz konventioneller Messungen von P- und PP-Laufzeiten. Wir erhalten ein detailliertes Modell von Mantelstrukturen welches sich durch alle Tiefen spannt. Diese bestätigen Ergebnisse aus früheren Tomographien, gleichzeitig werden sowohl Subduktions-Systeme (Tethys, Ägäis, Farallon) als auch aufsteigende Manteldiapire (Island, Afar, Tristan da Cunha) in unserem Modell deutlich schärfer abgebildet als bisher. Wir beschreiben den Verlauf dieser Strukturen durch den gesamten Mantel um die geomorphologischen Eigenschaften im Kontext großskaliger Mantelstrukturen zu verstehen. Im weiteren beschreiben und diskutieren wir detaillierte Strukturen in unserem Modell, wie etwa die Geometrie subduzierter Lithosphärenplatten im Mantel und Large Low Shear Velocity-Provinzen (LLVP) an der unteren Kern-Mantel-Grenze, sowie tomographische Beweise für Manteldiapire unter Island und Tristan da Cunha.

Contents

List of Figures

List of Tables

1 Introduction

This chapter is intended to provide an overview on the historical and methodological aspects of the global seismic tomography. In Section 1.1, major discoveries about the Earth's internal structure that led to the seismic tomography, as known today, will be reviewed. This will be followed in Section 1.2 by summarising the variants of global tomographic imaging techniques. Section 1.3 will put the global multiple-frequency inversion technique, the underlying method in this study, in the context of previous developments in finite-frequency tomography. After highlighting the objectives of this study in Section 1.4, the contents of the following chapters will be outlined in the last section.

1.1 A brief history of global seismic tomography

In 1906, Richard D. Oldham discovered the central "core", roughly halfway between the Earth's surface and its centre as shown in Fig. 1.1, on the basis of a so-called "travel-time curve" (Oldham, 1906). The graph represented the relation between the arrival times of a set of teleseismic waves and their corresponding epicentral distances. The arrival times in this plot, although measured from spatially distributed source-receiver pairs, formed coherent curves. Remaining discrepancies were explained by Oldham to be caused by (i) inaccuracies in the distant records, (ii) errors in determining the time of origin, and (iii) non-uniform rates of propagation in different directions. The infer-

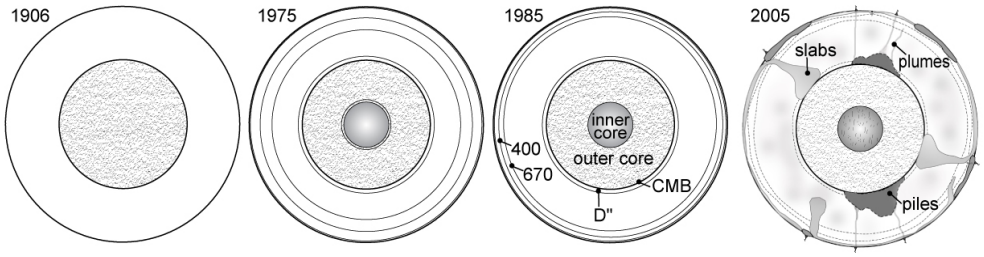

Figure 1.1: Our understanding of the internal structure of Earth has evolved from a homogeneous mantle-core model to detailed maps of its heterogeneities. See text for further discussion. ("we've come a long way" cartoon by E. Garnero, http://garnero.asu.edu/)

ences drawn by Oldham were built upon the assumption that the observed traveltimes have a spatially-invariant component which depends only on the epicentral distance and source depth: $T_{\text{arrival}} = T(\text{distance}, \text{depth}) + dT$. The first component $T(\text{distance}, \text{depth})$ was the basis of many discoveries of the main features of our planet in the twentieth century (Fig. 1.1):

In 1909, A. Mohorovičić inferred the crust-mantle discontinuity, known as Moho discontinuity, from P wave observations generated by regional earthquakes (Mohorovičić, 1909). The radius of the Earth's core was modified by Gutenberg (1913) after its first estimation by Oldham. H. Jeffreys's work on the Earth tides combined with the results of seismological studies led to a "truly" fluid core (Jeffreys, 1926). In 1936, I. Lehman inferred the existence of the inner core by observing unidentified P waves at large epicentral distances (Lehmann, 1936). H. Jeffrey and K. Bullen compiled traveltime tables and generated the first complete radially symmetric Earth model that could accurately predict seismic traveltimes and be used to locate earthquakes (Jeffreys and Bullen, 1940).

Early in the 1970s, analysis of large seismological data sets, enabled by rapidly growing global seismic networks, allowed significant refinements on the spherically symmetric Earth models by using global averages of seismic-wave propagation times, for example, Preliminary Reference Earth Model (Dziewonski and Anderson, 1981), IASP91 (Kennett and Engdahl, 1991) and AK135 (Kennett et al., 1995). This confirmed that, to the first order, the internal structure of the earth can be well approximated by a stratified, spherically symmetric model; however, it was also realised that a full 3-D interpretation was needed to satisfy deviations of the traveltime observations from the radially symmetric models. As a consequence, the other component (dT) became the main ingredient in estimating 3-D heterogeneities inside the earth via imaging techniques called as *seismic tomography*.

On global scales, a linearized seismic tomography method was first used by Dziewonski et al. (1977) to derive a model for large-scale heterogeneities in the lower mantle. Dziewonski (1984) applied this method to ISC delay times (500,000 teleseismic traveltime residuals from 5,000 earthquakes) and created the first reliable global tomographic model. The results, represented as images of two-dimensional slices or $\tau o \mu o \varsigma$, showed the long-wavelength lateral heterogeneities in the P wave velocity structure of the earth. For a comprehensive review of the history of tomography, refer to Nolet (2008) and references therein.

Since then and due to the growth of seismological waveform data holdings (at data centres) and their increasing data quality, the resolution of tomography models (on all scales) has been increasing. These developments have made high-resolution tomographic images one of the main inputs for a broad spectrum of geological and geophysical studies, such as the tomographic evidence for ancient, deep-sinking slabs (Van der Hilst et al., 1991) confirmed later by a global S-wave model (Grand et al., 1997), mantle convection (van der Hilst et al., 1997; Ritsema and Van Heijst, 2000), uprising mantle plumes (Bijwaard and Spakman, 1999; Montelli et al., 2004b; Zhao, 2004; French and Romanowicz, 2015), continental evolution (Ritsema et al., 1999), reconstruction of tectonic plate configurations (Van der Voo et al., 1999a; Sigloch et al., 2008; van der Meer et al., 2010; Sigloch and Mihalynuk, 2013) and temperature/compositional components of structural heterogeneities (Schuberth et al., 2009a,b), to name a few.

Geophysical inverse theory and methods to deal with the under-determined nature of inverse problems were formulated by Backus and Gilbert (1967, 1968, 1970); Jackson (1972). Early global models used ray (infinite frequency or zero wavelength) approximation, similar to geometrical optics, to model the measured arrival times due to the simplicity and computational efficiency of the theory (Dziewonski et al., 1977; Zhou, 1996; Grand et al., 1997; van der Hilst et al., 1997; Obayashi and Fukao, 1997; Kennett et al., 1998; Bijwaard et al., 1998; Boschi and Dziewonski, 2000; Kàrason and Van der Hilst, 2001). However, development of novel inversion techniques combined with the rapid progress in computing power led to a variety of global tomography methods to better exploit the full seismograms, and consequently, to better image the internal structure of the earth in all scales. In the next section, the concept behind these techniques as well as the main features of global tomography methods will be briefly discussed.

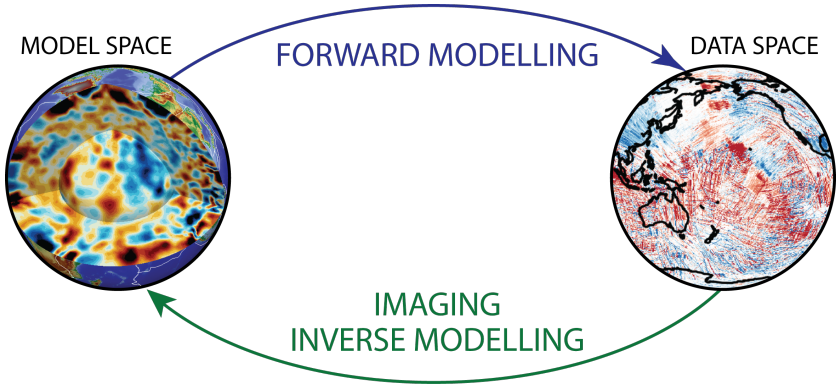

Figure 1.2: Inverse modelling is the reverse of forward modelling! In forward theory, the results of the measurements (data space) are predicted based on a model and a mapping function(s), for example, elastic wave equation, $Data = MappingFunc(EarthProperty)$. In inverse theory, the data is linked to the estimates of the model parameters via modelling and assumed theories, $EarthProperty = MappingFunc^{-1}(Data)$. Imaging is an inverse problem in which one best-fitting element of the model space (e.g., velocity structure) is estimated on the basis of the data space (e.g., traveltime measurements).

1.2 State of the art in global seismic tomography

Seismic tomography is an inverse problem in which (desired) model parameters are linked to the (measurable) seismological observations via modelling techniques (Fig. 1.2). This simple definition highlights the main components in which the tomography models differ fundamentally: what kind of seismological observations are measured (e.g., onset times, cross-correlation traveltimes, phase velocities, time-frequency misfits, instantaneous phase measurements or amplitudes)? what are the desired model parameters (e.g., P or S velocity variations, seismic anisotropy, visco-elastic dissipation or density)? What is the modelling technique (e.g., ray-theory, finite-frequency or adjoint)?

Rays vs. waves Traveltime observations modelled by ray-theoretical assumption allow to invert very large data sets at high resolution. This methodology has been widely used in creating global (P and S) tomography models (Dziewonski et al., 1977; Zhou, 1996; Grand et al., 1997; van der Hilst et al., 1997; Obayashi and Fukao, 1997; Kennett et al., 1998; Bijwaard et al., 1998; Boschi and Dziewonski, 2000; Kàrason and Van der Hilst, 2001; Zhao, 2004; Lei and Zhao, 2006; Amaru, 2007; Li et al., 2008; Auer et al., 2014; Koelemeijer et al., 2016). In this framework, the arrival times of seismic waves

are assumed to be sensitive to only the velocity structure along the geometrical ray path, that is, a curve of minimal traveltime that connects the source and receiver. The main advantages of this method are its simplicity and computational efficiency as well as the availability of large traveltime data sets, for example, ISC (International Seismological Centre) and NEIC (National Earthquake Information Center) catalogues. However, as the theory is based on infinite frequency or zero wavelength approximation, it is only valid when the length of the 3-D heterogeneities are large compared to the wavelength of propagating waves. Moreover, the observations for this method are usually hand-picked onset times; hence, the uncertainties associated with each measurement cannot be easily quantified. To overcome these limitations, two new classes of tomography methods were developed: finite-frequency tomography (Marquering et al., 1998; Dahlen et al., 2000; Hung et al., 2000; Zhou et al., 2004; Montelli et al., 2004b; Sigloch and Nolet, 2006) and full-waveform inversion (Tromp et al., 2005; Liu and Tromp, 2008; Fichtner et al., 2008, 2009b; Tape et al., 2009). Both methods compare the observed seismograms with synthetic waveforms, as opposed to only the onset times. This modification addresses several short-comings of ray-based tomography methods: the measurement technique requires no user-intervention, the quality of the measurements can be better quantified (e.g., cross-correlation factor), multifrequency observations are possible, and in addition to traveltimes, other observables (such as amplitude) can be extracted from the seismogram. Measured observables are projected onto the model parameters by the sensitivity kernels which can correctly account for the frequency-dependent interaction of waves with structural heterogeneities that ray-based methods are unable to accommodate. These kernels can be computed using semi-analytical approaches (Tian et al., 2007b), mode-coupling (Li and Romanowicz, 1996) or fully numerical techniques (Nissen-Meyer et al., 2007; Liu and Tromp, 2008).

Linear vs. nonlinear The inverse problem underlying seismic tomography can be regarded as an optimisation problem in which the goal is to minimise a misfit functional. Depending on the measured observables and complexity of the problem, the misfit can be minimised in either one linear step or iteratively by calculating the misfit gradient at each step. Examples for the linearized seismic tomography framework are ray-based least-squared methods and finite-frequency tomography. Computational efficiency is the main advantage of linearized inversion schemes. This allows for computing the approximate Hessian and incorporating a large amount of data (as one of the main factors in increasing the resolution) into a linear (single-iteration) inversion. However, if the observables are nonlinear in nature or sharp changes in the model parameters are expected (e.g., crustal and uppermost mantle imaging), iterative methods are preferred. One example of non-

linear inversion schemes is the adjoint tomography method in which fully numerical modelling techniques are used to calculate so-called event kernels, that is, simultaneously calculates the interaction between the forward and adjoint (backward) wavefields for one source and all the receivers (Tromp et al., 2005; Tape et al., 2007; Fichtner and Igel, 2008). This computes the gradient of the misfit function that can be used to update the model. One main advantage of this method is the possibility to successively solve the inverse problem through the propagation of wavefields in 3-D models, which is highly beneficial to resolve heterogeneous models with strong parameter gradients. However, for the ambitious data volumes and frequencies used in linearized global models, fully numerical modelling in 3-D reference models remains well beyond reach. As a consequence, the data sets used in adjoint tomography are restricted to low frequencies and few earthquakes. Another limiting factor in this method is the starting model which needs to be sufficiently close to the optimum model to ensure the convergence. The heavy computational cost to estimate individual source-receiver kernels also prohibits the calculation of approximate Hessian; hence, only event-kernels (gradient of the misfit function) are usually computed.

Deterministic vs. probabilistic Tomography models are inherently non-unique due to the limited amount of independent information and uncertainties in the data space (observations). As a result, a variety of models exists that can explain one set of data. The true properties of these random variables (data and model parameters) can be best specified by probability density functions (*pdf*) through probabilistic inversion theory (Tarantola, 2005). However, sampling the *pdf* of model parameters in global tomography is still computationally intractable. By taking certain approximations and simplifying assumptions, one optimal model that explains the observations can be derived based on deterministic inverse theory and by minimising a selected misfit function. This approach has been the basis of the most known inverse solutions, although there have been attempts for the probabilistic inversions as well (Trampert et al., 2004; Mosca et al., 2012; Käufl et al., 2013).

Frequency content Observations in seismic tomography are extracted from the parts of the signal (in frequency or time domain) that carry the imprints of the 3-D distribution of physical properties in the earth. Depending on the sensitivity kernels (the relation between measured data and structural model), observations or more importantly, a combination of them can constrain the earth structure locally or globally. Generally speaking, by increasing the frequency content of these observations, smaller-scale structures can be resolved in more limited regions (narrower sensitivities). Fig. 1.3 compares these two aspects (spatial extent and frequency content) of various

tomographic techniques that are currently being used. The red colour shows the methods that can potentially cover the whole globe. The blue colour identifies the techniques that can either illuminate a limited depth range (surface wave) or provide regional models (regional adjoint).

A major effort in seismic tomography is focused on the construction of multi-scale models that can explain a wide-range of multifrequency measurements, i.e. span the horizontal axis of Fig. 1.3. To this end, two approaches have been proposed. On the one hand, inverting large tomographic data sets that include a variety of observations, different frequency bands and seismic phases, can result in one model that to a very good extent explain the measurements. The challenge in this approach is to accurately map the information of multifrequency measurements through parameterisation and regularisation (in linearized tomographic methods). Hence, inversion meshes of spatially varying element size have been widely used to adapt the "retrievable" resolution in different regions in order to make the joint inversion of high and low-frequency measurements possible (e.g., Nolet and Montelli (2005); Auer et al. (2014); French and Romanowicz (2014); Zaroli et al. (2015)). On the other hand, a composite model that successively includes high-resolution regional models into a smooth 3-D background model has been also suggested (Afanasiev et al., 2016). The drawback of this method is that sharp edges between the global and regional models can exist, and the model as a mix of independent regional tomographic models may not well "explain" the observations. Nevertheless, as there only exists one velocity structure of the earth, the assemblage of the regional models should ultimately result in one high-resolution global model.

Among all the variants of global seismic tomography methods, our inversion framework is built upon multiple-frequency, waveform-based measurements. As shown in Fig. 1.3, these measurements cover the whole frequency spectrum usable for body-wave tomography, and by inverting them jointly, the constrains on the tomographic solution multiplies. As cross-correlation traveltimes retain a near-linear relationship to velocity model perturbations over a large range (Mercerat and Nolet, 2013), we start with a 1D background model and obtain the optimum model in one linear step. We expect that our ability to exploit the highly-resolving short wavelengths will far outweigh the limitation of not being able to iteratively update the solution. Compared to the early global finite-frequency tomography studies, several technical and theoretical developments have been done in our framework which will be explained in the next section.

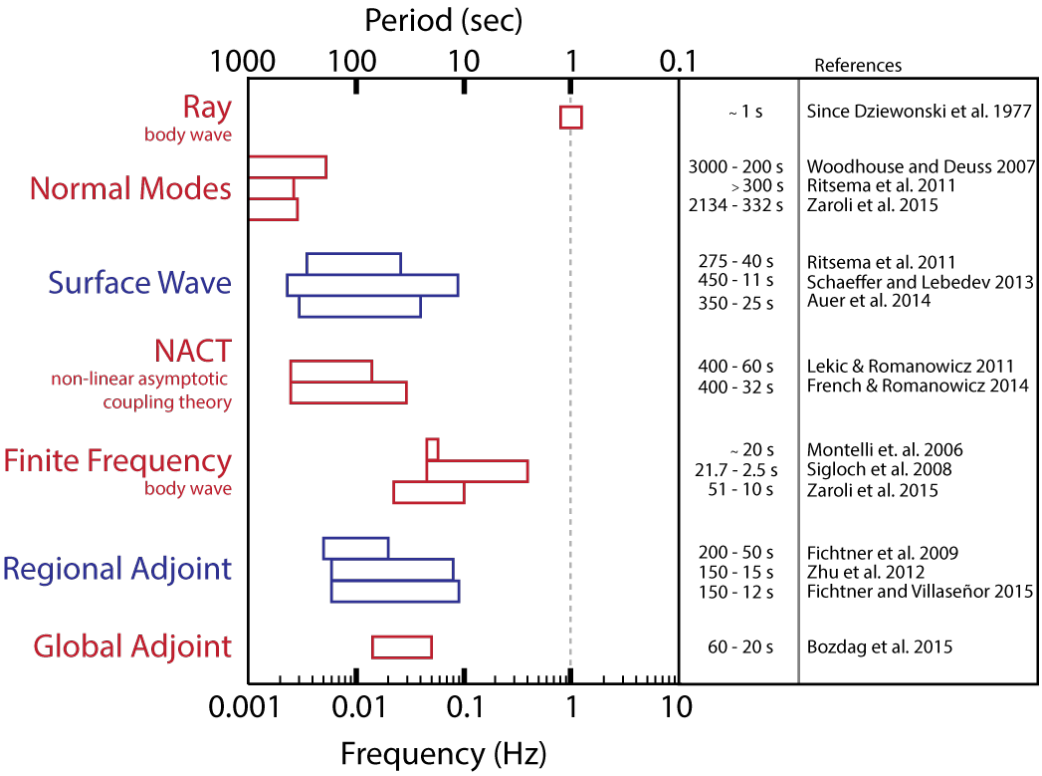

Figure 1.3: Frequency content of seismic waves is the limiting factor for both the resolution and the spatial extent of resolved structures. Here, various tomography techniques are compared as a function of frequency. The trade-off is that long-period seismic waves put constraints on larger scales (e.g., no loss of lateral resolution in case of normal modes) and short-period waves can resolve small-scale structures. The goal in tomography is to create a multi-scale model that can explain the observations at all frequencies. However, this faces several challenges. Refer to text for more discussion. List of references (from top to bottom): Dziewonski et al. (1977); Woodhouse and Deuss (2007); Ritsema et al. (2011); Zaroli et al. (2015); Schaeffer and Lebedev (2013); Auer et al. (2014); Lekić and Romanowicz (2011); French and Romanowicz (2014); Montelli et al. (2006); Sigloch et al. (2008); Fichtner et al. (2009b); Zhu et al. (2012); Fichtner and Villaseñor (2015); Bozdag et al. (2015).

1.3 Global multiple-frequency tomography

Finite-frequency tomography is a waveform-based inversion technique that can correctly account for the frequency-dependent interaction of waves with the structural heterogeneities (i.e., scattering of energy). Spatially extended 3-D sensitivity distribution of waves is calculated based on first-order Born scattering kernels (Marquering et al., 1998; Dahlen et al., 2000; Hung et al., 2000; Zhao et al., 2000). These kernels can accurately account for the diffractive wavefront healing which ray-based methods are unable to accommodate. Moreover, traveltime residuals can be estimated in different frequency bands which constrain the frequency dispersion of seismic waves and contain information about the size of the heterogeneities in the Earth.

Montelli et al. (2004b) was first who demonstrated that the solution of full-fledged global tomography problems by considering physically realistic sensitivity kernels is computationally feasible. That study resulted in the first global tomography model accounting for the frequency dependence of seismic body waves. However, for lack of dedicated measurements, they had to retrospectively assign some finite-frequency content, at the low end of the body-wave spectrum ($\approx 20s$), to pre-existing traveltime data sets.

Sigloch and Nolet (2006) developed a method to measure the finite-frequency body-wave amplitudes and traveltimes in its entire frequency content, from 30.0 down to 2 sec, with lower measurement uncertainties and with the flexibility to identify and include only those of high signal quality. This method generates kind of data that finite-frequency modelling was envisioned for, consistent with the derivation of the kernels and their theoretical definition (Dahlen et al., 2000; Dahlen and Baig, 2002). The new generation of finite-frequency tomography, multiple-frequency tomography as named by Sigloch et al. (2008), was built upon such measurements. By applying this method to North America, Sigloch et al. (2008) created a large multifrequency data set, and they showed that finite-frequency tomography is clearly superior to ray theory in imaging (particularly) the lower mantle.

In this study, we use this multifrequency measurement technique (Sigloch and Nolet, 2006; Hosseini and Sigloch, 2015) in order to construct a global multiple-frequency tomography model based on core-diffracted (Pdiff) and teleseismic (P and PP) measurements. In the next section, the main developments that led to this model will be highlighted.

1.4 Objectives of this study

This work is in the continuation of a joint effort to probe the structural complexities of the mantle (at all depths) by using waveform-based tomography methods. A brief summary follows, highlighting the main developments and technical novelties of this study in creating a new global seismic tomography model of isotropic P wave velocity anomalies (Fig. 1.4 depicts some examples for the velocity heterogeneities extracted from this model):

1. No Data Left Behind (NDLB). A processing strategy efficient enough to assemble the largest-possible data sets for waveform-based tomographic inversions (Hosseini-zad et al., 2012). In practice, this algorithm glues all the steps required for global (and regional) seismic tomography to execute them as automatically and efficiently as possible. A major effort in technical developments of this study has been focused on delivering codes and solutions, each serves as one processing block, to this framework. In short, this algorithm collects and organises the waveform data set for one event, calculates synthetic waveforms on-the-fly, identifies good time-frequency windows, measures the observables and applies the required corrections, calculates sensitivity kernels, and assembles them for matrix inversion.

2. Core-diffracted P waves (Pdiff). Pdiff waves are seismic body waves that dive deep enough to sense the earth's core. These waves are the most highly resolving wave type that extensively sample the lower third of the mantle. However, core-diffracted waves, and Pdiff in particular, have seen very little use in tomography because of the highly dispersive and non-ray-like behaviour of these waves which make their modelling difficult. We developed a processing scheme to measure finite-frequency traveltime and amplitude anomalies of arbitrary seismic body-wave phases in a fully automatic way (item 1), with an initial focus on Pdiff waves. To account for diffraction and non-ray-like behaviour of such core-sensitive waves, Green's functions were calculated by semi-analytical (i.e., theoretically exact) wave propagation through a spherically symmetric reference model, to 1Hz dominant period.

3. Multifrequency measurement technique. The measurement procedure for multifrequency traveltimes of this work is based on that for teleseismic body-waves by Sigloch and Nolet (2006). We showed that this method can be applied to core-diffracted waves, and a maximum of information can be extracted via cross-correlating broad-band seismo-

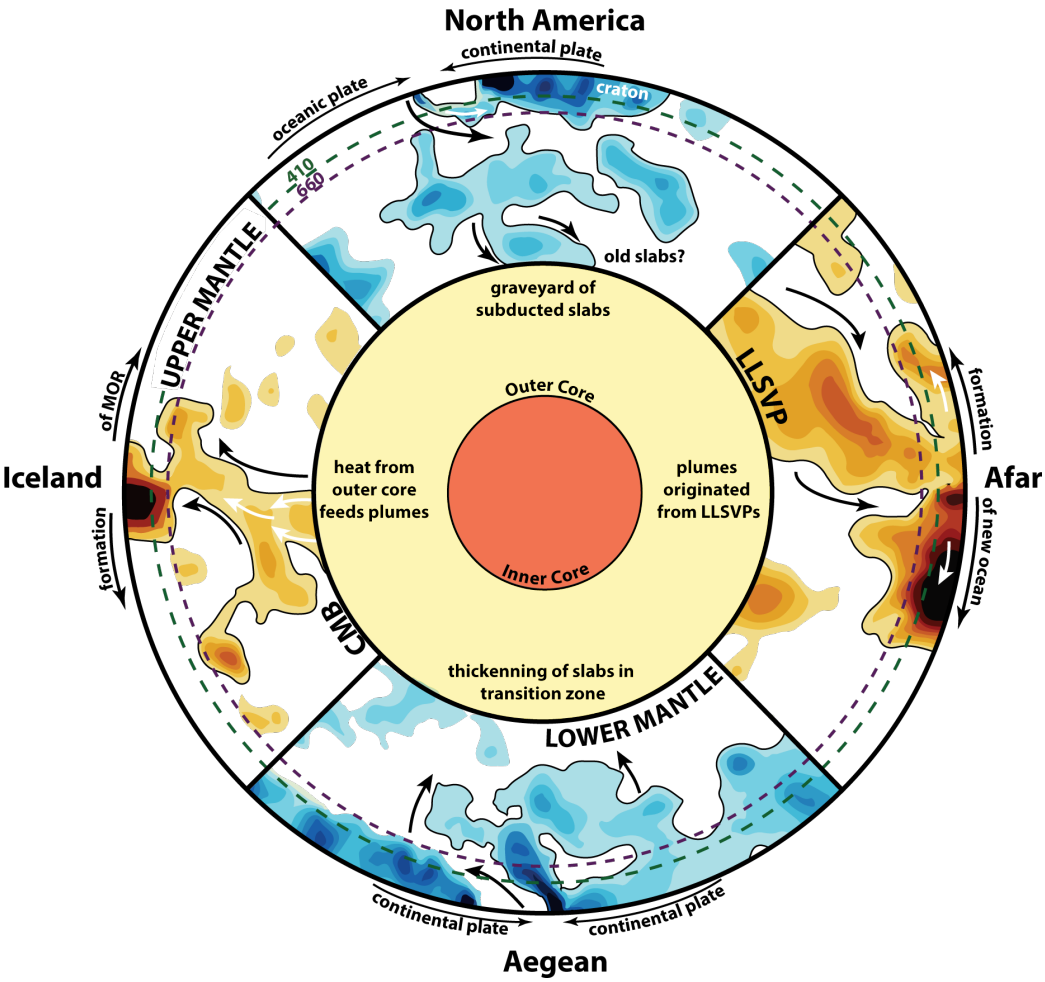

Figure 1.4: Vertical cross-sections beneath North America, Afar, Aegean and Iceland derived from our global multiple-frequency tomography model. The technical and theoretical developments in order to construct this whole-mantle P wave model will be discussed in the following chapters. We will also report the observed structural features (similar to this figure), test their robustness with variety of resolution tests, and interpret them in terms of their morphological characteristics and their (in)consistencies with previous geophysical and geological findings, as schematically shown here.

grams with synthetic waveforms computed by modelling the 3-D wavefields (item 2). This resulted in one of the largest core-diffracted P wave traveltime collection put together so far (Hosseini and Sigloch, 2015).

4. Inversion technique. A framework for joint inversion of the multifrequency measurements and a set of short period traveltimes was designed with the following main features: the model was parameterised adaptively by tetrahedra using the amplitudes of the sensitivity kernels at each node. Such a data-adaptive inversion mesh is crucial to invert large tomographic data sets for high-resolution multi-scale tomographic models. The matrix inversion was done by an iterative conjugate gradient method (similar to previous finite-frequency inversions); however, a scheme for locally adjusted damping parameters was developed and implemented. This method helped to go beyond the limitations of globally constant regularisation in which the highly resolved regions will be over-regularised to account for the lack of data in other locations, or unknown with poor data coverage will be under-regularised to keep the resolution of highly sampled parameters. A two-step approach in selecting the model(s) was employed in which the preferred solution(s) was obtained by using $|m|^2$ and l_∞-norm of the model parameters, and the choice of the regularisation in the selected models was checked by resolution tests through the same inversion procedure on known synthetic inputs.

5. Model interpretation. The multi-scale mantle structure derived from our global multiple-frequency seismic tomography is presented with a focus on the lower mantle heterogeneities and their relation to the shallower depths. The mapped seismic structures in this model are reported, their robustness is tested via a variety of resolution tests, and some of the observed features of these velocity structures are related to previous geophysical and geological findings (Fig. 1.4).

1.5 Thesis outline

Each chapter in this thesis covers one or more aspects of our global multiple-frequency seismic tomography method. As shown in Fig. 1.5, the subsequent chapters combined span all the steps in our algorithm, from data and multi-frequency measurement technique to the inversion and model interpretation. It has been tried to keep the chapters self-contained as follow:

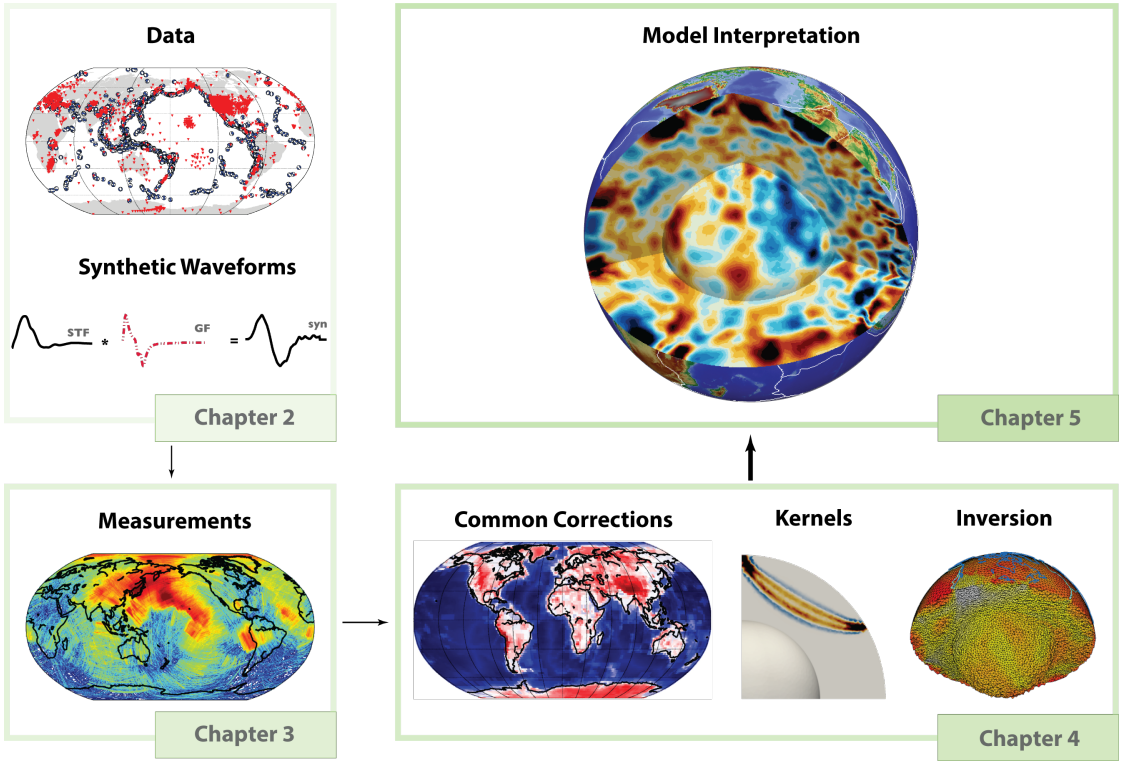

Figure 1.5: Each chapter of this thesis covers one or more aspects of our "No Data Left Behind" processing strategy. Here, only the major steps of this algorithm are shown. Chapter 2 is dedicated to data and synthetic waveforms. In Chapter 3, a multifrequency measurement technique will be presented to derive the traveltime observables from teleseismic and core-diffracted waves. Our inversion framework applied to these observations will be described in Chapter 4, and some of the major structural features of a "preferred" model will be illustrated. Finally, Chapter 5 presents the multi-scale structural heterogeneities derived from our global tomography model with a focus on the features at the lower-third of the mantle and their relation to those in the shallower depths.

In Chapter 2, retrieving and processing of large seismological data sets by using a newly developed tool called obspyDMT will be described with a focus on its functionality, design and technical implementation. The large volumes of broad-band waveform data used throughout this study were retrieved from several data management centres by using this fully automated Python software. obspyDMT also executed the instrument correction to ground displacement, bandpass-filtering, local archiving, and updating of the collection when new waveforms became available on the data centre servers. At the end of this chapter, the relation between the processed real data and their corresponding synthetic waveforms will be discussed.

Chapter 3 presents the main data processing effort of this study to make core-diffracted body waves usable for global waveform tomography, across their entire frequency range. A method is demonstrated that routinely calculates finite-frequency traveltimes of Pdiff waves by cross-correlating large quantities of waveform data with synthetic seismograms, in frequency passbands ranging from 30.0 s to 2.7 s dominant period. Green's functions for $\approx$ 2000 earthquakes, typically comprising thousands of seismograms, are calculated by theoretically exact wave propagation through a spherically symmetric earth model, up to 1 Hz dominant period. The statistics of traveltimes for Pdiff and teleseismic P are presented, including their frequency dependence. The information content of the novel Pdiff measurements is demonstrated by projecting traveltime anomalies on the core-grazing segments of their nominal ray paths. Already from this "proto-tomography" exercise, structural heterogeneity of considerable detail emerges, which is compared to current structural knowledge about the lowermost mantle.

In Chapter 4, a new global seismic tomography model of isotropic P wave velocity anomalies at all mantle depths will be presented. This chapter puts its emphasis on the methodology for joint inversion of the multifrequency cross-correlation measurements and a set of short period traveltime anomalies to image the earth's mantle down to the CMB. Technical developments, such as adaptive parameterisation, inclusion of Pdiff measurements, local regularisation and selection of a preferred model, will be highlighted. Moreover, first-order features of our "preferred" global tomography model will be illustrated and discussed.

Chapter 5 presents the multi-scale lower mantle structure derived from our global seismic tomography model. The geometries of seismically fast anomalies representing subducted slabs still visible in the mantle, low-velocity anomalies and their relation to presumed hotspot locations and the subdivisions of Large Low Shear Velocity Provinces at the base of the mantle will be discussed. Although the main objective of this chapter is to report the

mapped velocity heterogeneities, a conservative model interpretation is also presented for some of the structural features.

2

Retrieving and processing of large seismological data sets

Abstract

We present *obspyDMT*, a software toolbox for query, retrieval, processing and management of (large) seismological data sets. obspyDMT is a stand-alone toolbox not associated with any specific data centre or data exchange protocol. It primarily simplifies and speeds up user-interaction with different data centres and data types, in more versatile ways than existing tools. The user is shielded from the complexities of interacting with different data centres, and provided with powerful diagnostic and plotting tools to check the retrieved data and meta-data information. It seamlessly tacks on to a back-end that facilitates data archival, pre-processing, instrument correction, and quality control – routine but non-trivial tasks that can consume much user-time as well. We describe obspyDMT's functionality, design and technical implementation accompanied by an overview of its use cases. As an example of a typical problem encountered in seismogram preprocessing, we show how its diagnostic plots can be used to systematically check for inconsistencies in response files of two example stations, a procedure scalable for arbitrarily large data sets. Moreover, synthetic seismograms of an example data set are

computed based on obspyDMT's automatically organised meta-data information. obspyDMT is an easy-to-use command line tool. It is free, open-source, community software written in the Python programming language, but no knowledge of Python is required. It is mainly a productivity tool for practising seismologists, but its integrated plotting options also make it an effective teaching tool.

2.1 Introduction

Seismology is a science of Big Data. Since the advent of global digital networks in the 1990's, the growth of seismological waveform data holdings at international data centres has continually accelerated. The data avalanche is a blessing, but it poses challenges to the scientist who needs to find and process these waveforms. Which data are available at the various international data centres? How can subsets of interest be selected, downloaded, organised, pre-processed, instrument-corrected and quality-controlled in a manageable amount of user time? Quality control and instrument corrections are non-trivial tasks – which tools provide adequate diagnostics to verify the integrity of data obtained? Almost every data-driven work flow in seismology begins with these considerations. As a project progresses, local data holdings often need to be updated, repaired, or extended (e.g., troubleshooting of earlier failed requests; adding waveforms made available since initial retrieval; adding (meta-)data from other data centres; downloading corrected meta-data files). Surgical tasks of this kind can easily require more human supervision than the initial retrieval.

For a sense of data volumes, consider the example of Fig. 2.1, which arose in our work on global waveform tomography (Hosseini et al., 2014; Hosseini and Sigloch, 2015). Using the obspyDMT software presented here, we queried the IRIS DMC for about hour-long, broad-band waveform segments that could be obtained for earthquakes exceeding magnitude 5.0. Fig. 2.1(a) plots the data centre's response: since 1990, IRIS' event catalogue lists 1000-3000 such events per year, visualised in obspyDMT's automatically generated map of Fig. 2.1(b). The number of archived broad-band channels has risen to almost 5000 in 2014, and we are offered more than 10^8 waveforms, corresponding terabytes of data (and very long download times). Next, most applications would call for a narrowing down to a desirable subset of data, before launching an actual request.

Besides large volumes, the hallmark of seismological data is heterogeneity. A culture of data sharing from permanent networks and temporary experi-

ments around the world means that waveforms get archived at many different data centres around the globe; in different waveform and meta-data formats; documented and quality-controlled to varying degrees. Archives receive permanent inflows of data from telemetered stations, but also batch-wise contributions from temporary experiments. Many experiments make meta-data available immediately but limit the access to actual waveforms for several years. No general mechanism exists for broadcasting updates about data centre holdings, which instead need to be actively and repeatedly queried by interested users. Data access mechanisms tend to be specific to each centre. Downloads of time-continuous or very long seismograms may be less supported than downloads of short segments around earthquake occurrences.

obspyDMT is free, open-source community software that strives to address these access challenges in a more comprehensive, integrated, and time-saving manner than existing software (e.g., WILBER, WebDC, BREQ_FAST, NetDC, EMERALD (West and Fouch, 2012), IGeoS (Morozov and Pavlis, 2011a,b), SOD (T. J. Owens and Oliver-Paul, 2004) and ObsPyLoad (Scheingraber et al., 2013)). It is an easy-to-use command-line tool for the query, retrieval, and management of seismograms. The user is shielded from the complexities of interacting with different data centres, and provided with powerful diagnostic and plotting tools to check the retrieved data and meta-data, and to execute most routine pre-processing tasks, including instrument corrections. obspyDMT is written in the Python programming language, but no knowledge of Python is required.

This chapter describes obspyDMT's functionality, design and technical implementation accompanied by an overview of its use cases. This includes an example how to link to Instaseis (van Driel et al., 2015), a data base that computes synthetic broad-band seismograms on a regional or global scale, which can be directly compared (or cross-correlated) with real data managed by obspyDMT.

2.1.1 Feature overview

obspyDMT is a stand-alone tool not associated with any specific data centre or data exchange protocol. In a style similar to Unix shells, it issues single-line commands:

```
obspyDMT
```

There are no required options, and omission of any option will trigger a default behaviour. This makes obspyDMT robust to run and friendly

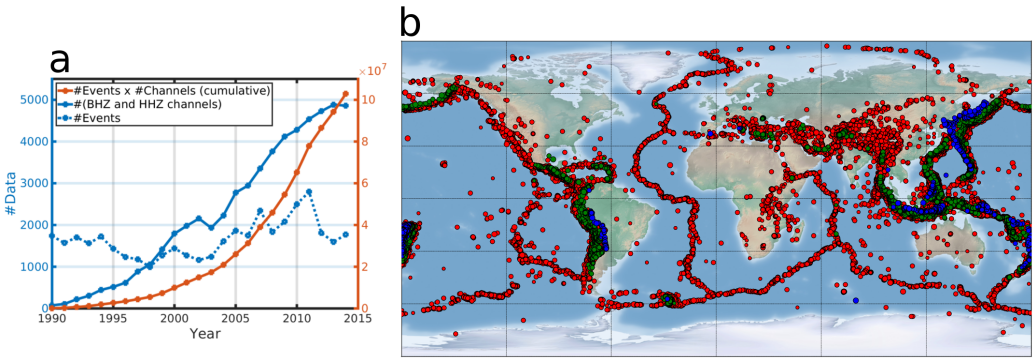

Figure 2.1: Exponential growth of seismological waveform data holdings at international data centres. Using obspyDMT, we queried the IRIS DMC for about hour-long, vertical broad-band (BHZ and HHZ) waveform segments that could be obtained for earthquakes exceeding magnitude 5.0. (a) The data centre's response. The orange line shows cumulative sum of available event-based waveforms for this request, $\sum_{y=1990}^{year} [num\_events(y) \times num\_channels(y)]$. Number of events and available seismograms in each year are shown by dotted and solid blue lines, respectively. (b) Global seismicity map of earthquakes in panel (a) coloured by depth. Red: 0-70 km; green: 70-300 km; blue: $\geq$300 km.

to learn. To produce different functionalities, the command is modified by appended options. For example, the command

```
obspyDMT --datapath iris_events_dir --min_date 1990-01-01
    --max_date 2015-01-01 --min_mag 5.0 --event_info
    --plot_seismicity
```

downloaded a global seismicity catalogue from the IRIS DMC, saved the meta-data in a predefined directory structure, and generated Fig. 2.1 as a diagnostic display of the result.

obspyDMT is part of the ObsPy ecosystem (Beyreuther et al., 2010; Megies et al., 2011; Krischer et al., 2015), an open-source community project that develops Python software for seismological observatories under the GNU Lesser General Public License, hosted by the University of Munich. obspyDMT uses many of ObsPy's utility functions, as well as functions from Python's numpy, scipy and matplotlib libraries (Hunter, 2007), combining them into a more specialised piece of software. While no knowledge of Python is required to use obspyDMT, a software developer may seamlessly integrate it into other Python code. Python also makes it easy to wrap source codes written in other programming languages. For example, ObsPy wraps *evalresp*, IRIS' maturely developed software to correct instrument responses. We begin by listing the functionality of obspyDMT, then compare it to existing tools for data retrieval and management.

2.2 Software functionality

- Query of station meta-data: by absolute time or relative to earthquake occurrences; by geographic area (rectangles or circles); by channel or instrument type; wildcarding (*) is supported; simultaneous queries of different data centres.

- Query of earthquake source meta-data: from different catalogue providers (e.g., NEIC, Global CMT, IRIS DMC, NERIES, NCEDC, USGS, INGV and ISC); event origin information or full moment tensors; by time window, region, event magnitude and/or event depth.

- Diagnostic plots to visualise meta-data; plots are generated by simple inclusion of an option flag. Fig. 2.2 shows an example for a global seismicity map retrieved from the NEIC catalogue.

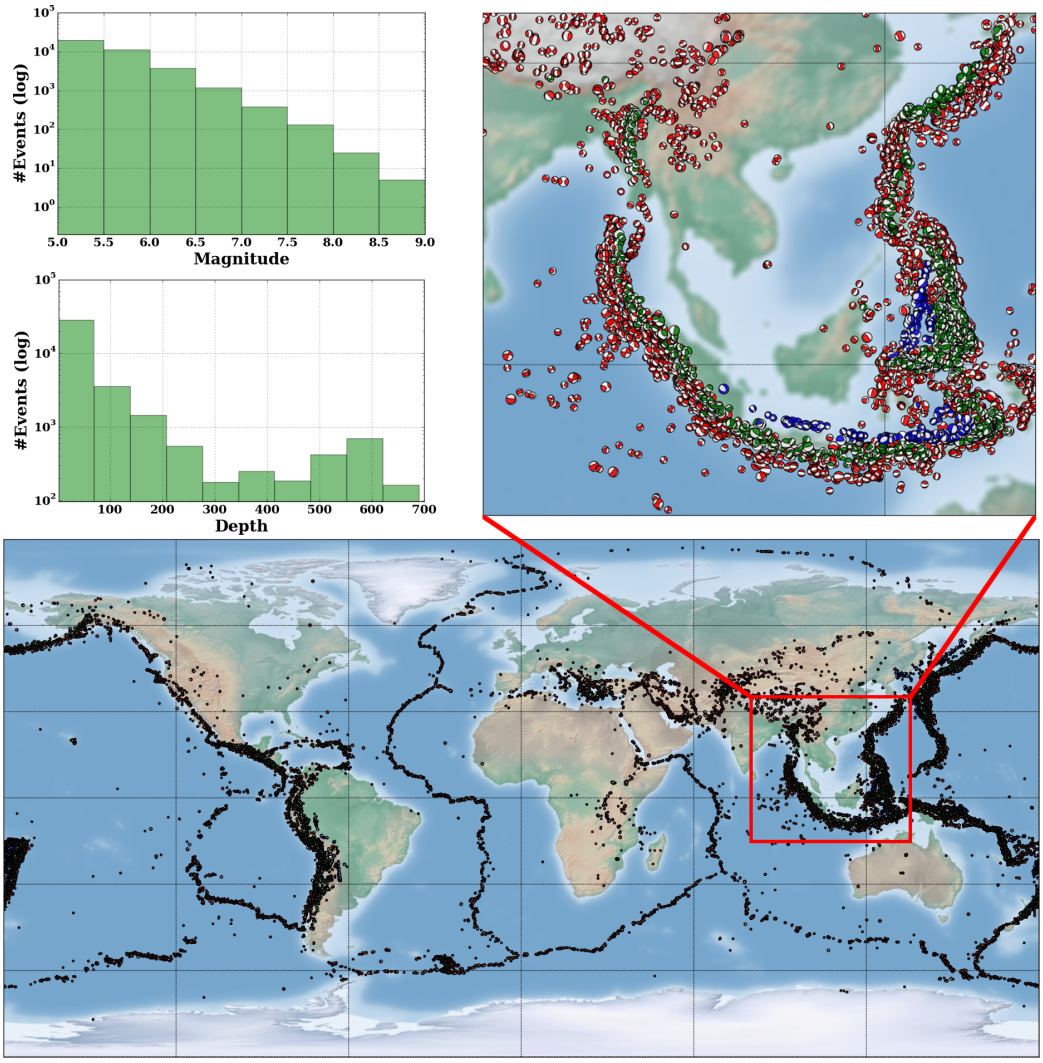

Figure 2.2: Global seismicity map of archived earthquakes in *NEIC* catalogue with magnitude more than 5.0 that occurred between 1976 and 2014. One command queried the NEIC catalogue, stored and organised the retrieved information and generated the seismicity map. (No actual waveform data were queried in this example). The results of some basic statistics (magnitude and depth histograms) are also generated and plotted automatically (top-left panel). Note the rendering of coloured beach balls in the map inset (deepest seismicity in the foreground). The global map also contains beach balls rather than just simple black dots, but they do not become apparent at this zoom level.

- Retrieval of actual waveform data (seismograms) according to the results of meta-data queries. Support for different protocols (FDSN web services, ArcLink). Fig. 2.3 demonstrates a map plot of ray paths between sources and receivers in an example data set.

- Retrieval of time-continuous series of arbitrary length; diagnostic log files. As an example, Fig. 2.4 shows month-long waveforms retrieved from *YV* network for a set of selected stations (RR0*, RR1* and RR2*, that is, all stations that their names start with RR0, RR1 and RR2).

- Parallelised retrieval of waveform data from one data centre for increased speed. Simultaneous retrieval of waveform data from different data centres is also supported.

- Update mode: identical or modified queries can be relaunched; only new or previously failed data will be retrieved from the data centre(s).

- Tolerant of retrieval errors and missing data (includes diagnostic logs).

- Automatic organisation of data, meta-data and log files into standardised directory trees. (At present no tie to any specific database system.)

- Processing the data set using default or user-defined instructions; obspy, SAC (George Helffrich and Bastow, 2013) and/or any other processing tool can be used to customise the processing unit on the waveform level. Process the whole data set directly after retrieval of waveform data or as a separate step; support for parallelised processing.

- Application of instrument responses. Support for various instrument formats (e.g., StationXML and Dataless SEED). Diagnostic plots of analogue and digital filter stages. Option of parallelised instrument correction, taking advantage of multi-core architectures even on desktop processors.

- Retrieval of synthetic seismograms from IRIS' data services products (Trabant et al., 2012) for comparison to real data.

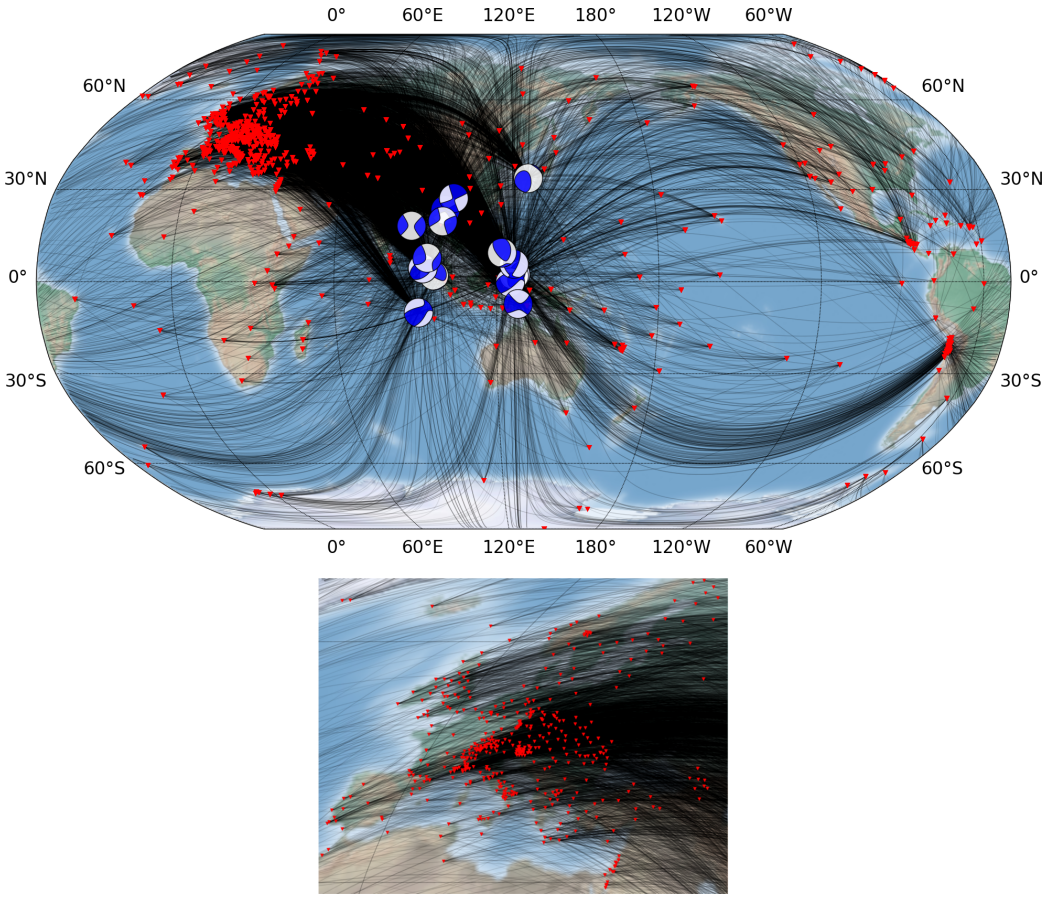

Figure 2.3: Ray paths between 16 earthquakes (beachballs) and stations (red triangles) for an example data set. A small subset of Indonesian earthquakes with magnitude more than 6.0 and shallower than 100 km that occurred between 2014-02-01 and 2014-12-01 was queried from the NEIC catalogue. Waveforms are retrieved from three data centres: broad-band vertical channels (BHZ) with seismic network code *GSN* from IRIS DMC; all BHZ and HHZ channels from European ORFEUS / EIDA and GFZ (GEOFON program). Issuing a single-line command is the only requirement on user time, everything else is done automatically. Specifically, obspyDMT will: **1.** Request event information from the seismicity catalogue. **2.** Generate and populate local directory trees (one per event) with the meta-data retrieved. **3.** Retrieve the waveform data for events and all requested stations and station meta-data. **4.** Save meta-data for events and stations, and additional log files on query success. **5.** Run default pre-processing operations, which consist of removing the trend and mean of the waveforms, tapering, filtering, and deconvolving the instrument response (all customisable). **6.** Save the processed waveforms to local event directories.

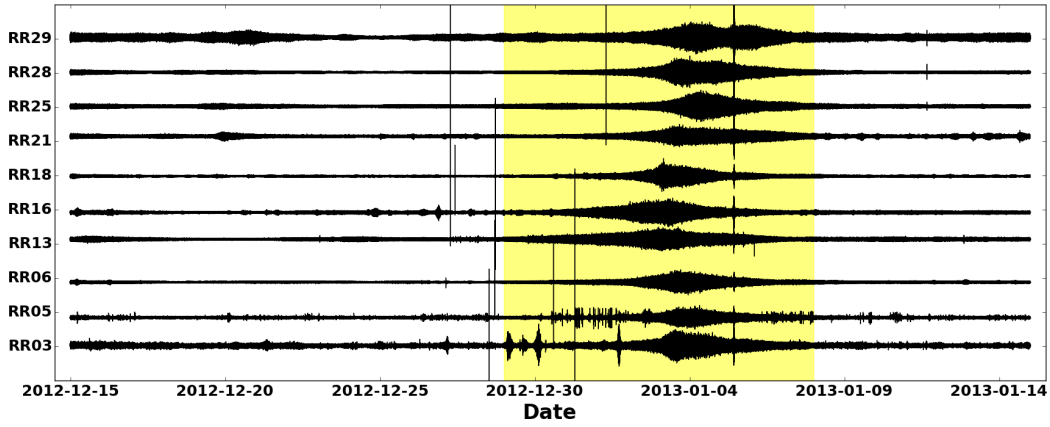

Figure 2.4: Retrieval of time-continuous series of arbitrary length. Ten selected RHUM-RUM stations (Barruol and Sigloch, 2013), queried from *RESIF* data centre, are plotted for a period of 30 days. The cyclone Dumile (yellow box around 2012-12-29 until 2013-01-08) is highlighted. In large (event-based or) continuous data retrieval, it may be needed to downsample waveforms in order to reduce the storage and processing time. obspyDMT can resample retrieved waveforms to any desired sampling rate. It automatically resamples a waveform in several steps in case the desired sampling rate is considerably different from the original one. In downsampling, a sharp low pass filter is applied to suppress aliasing effects due to changes in Nyquist frequency. In this example, waveforms were downsampled from 50 to 10 Hz..

2.2.1 Comparison to existing software

Various community software packages exist for achieving the tasks outlined in Section 2.2, though to our knowledge no other freely available package achieves them all. Table 2.1 compares the features of popular seismological community software to those of obspyDMT. We compare only to tools that include functionality for data retrieval.

All data centres offer such tools, but each is limited to retrieving data from one specific centre. For example, both IRIS DMC in the U.S. and ORFEUS Data Center (ODC) in Europe implement the web-form-based "WILBER" service (for retrieving event-based waveforms) as well as the e-mail-based "BREQ_FAST" service (for time-continuous waveforms). If a user requires data from both centres, they need to be contacted separately. If a user requires event-based as well as continuous data from a centre, it needs to be contacted twice, using two different tools.

obspyDMT is the only tool among those in Table 2.1 that provides access to both data centres (in a single command), and both types of waveform data (in two separate commands). The demand for continuous time series, often in large quantities, has surged with the rapid rise of cross-correlation methods based on ambient noise (Shapiro and Campillo, 2004). obspyDMT provides more convenient access than the e-mail-based tools BREQ_FAST or NetDC.

obspyDMT is also the only tool to offer an "update" mode for waveforms, response files and/or meta-data information: re-launching a previous request will identify and retrieve only matching data that could not be retrieved earlier. Like obspyDMT, SOD, IGeoS and EMERALD are standalone software that runs on the user's computer rather than the data centre server. All four communicate with data centres via the relatively new "webservices" interfaces defined by the International Federation of Digital Seismograph Networks (FDSN). Queries are formulated as URL strings (Uniform Resource Locators) that point to physical data resources over the internet. We refer to this access method as "direct". Compared to older access methods, it can save much human intervention time by freeing the user of clicking through web pages (WILBER, WebDC) or managing e-mails (BREQ_FAST, NetDC). SOD, IGeoS and EMERALD are special-purpose tools in that they retrieve event-based waveforms only.

By also managing the data download and archival to a user's local computer, the standalone tools obspyDMT and EMERALD relieve the user of additional tedious and time-consuming steps. Only obspyDMT and SOD offer instrument correction, but SOD does not generate diagnostic plots of the data or meta-data, unlike obspyDMT or EMERALD.

In summary, obspyDMT primarily simplifies and speeds up user interaction with *different* data centres and data types, in more versatile ways than existing tools. It seamlessly tacks on a back-end that facilitates data archival, pre-processing, instrument correction, and quality control – routine but non-trivial tasks that can consume much user-time as well. It is mainly a productivity tool for the practising seismologist, but its integrated plotting options also make it an effective teaching tool.

2.3 Instrument correction

Modern seismometers measure the ground motion and translate it into digitised voltage signals called *raw counts*. The relation between a recorded signal and ground motion (e.g., displacement) depends on response functions of seismometer's components, such as sensor, amplifier, filter and digitiser. These are called as "stages", and their overall response can be described by a transfer function or frequency response function of the system. For simplicity, we continue with analogue frequency instrument response. Following the nomenclature of *SEED Manual*, the frequency response G can then be written as

$$G(j\omega) = S_d A_0 \frac{\prod_{n=1}^{N}(j\omega - r_n)}{\prod_{m=1}^{M}(j\omega - p_m)} \tag{2.1}$$

r and p stand for zeros and poles of a system. N and M are the number of zeros and poles, respectively. S_d is the stage gain. A_0 is the normalisation factor which scales the amplitude of the poles-and-zeros polynomial to unity at a reference frequency (usually 1 Hz):

$$A_0 \left| \frac{\prod_{n=1}^{N}(j\omega_{ref} - r_n)}{\prod_{m=1}^{M}(j\omega_{ref} - p_m)} \right| = 1 \tag{2.2}$$

The frequency response function G relates the ground motion V (input signal) to recorded raw counts R by: (Scherbaum, 1996)

$$R(j\omega) = G(j\omega) \times V(j\omega) \tag{2.3}$$

in which, $R(j\omega)$ and $V(j\omega)$ are the Fourier transform of raw counts and input signals, respectively. Hence, instrument response correction can be carried out by transforming the raw seismogram $R(t)$ to the spectral domain, dividing $R(j\omega)$ by $G(j\omega)$ (deconvolution in time) and transforming the result back into the time domain. This way, $V(t)$ in the physical unit (displacement, velocity and acceleration) can be obtained.

tool	access method	data sources/interfaces	retrieval modes	archiving	instrument correction	plots
WILBER	web portal	IRIS DMC or ODC/EIDA	E	✗	✗	✗
WebDC	web portal	ODC/EIDA	E	✗	✗	✗
BREQ_FAST	e-mail	IRIS DMC or ODC/EIDA	C	✗	✗	✗
NetDC	e-mail	NCEDC	C	✗	✗	✗
EMERALD	direct	IRIS DMC	E	✓	✗	✓
IGeoS	direct	IRIS DMC	E	✗	✗	✓
SOD	direct	FDSN	E	✗	✓ (gain correction)	✓
obspyDMT	direct	FDSN and ArcLink	C, E, U	✓	✓	✓

Table 2.1: Comparison of seismological data retrieval and management tools. Abbreviations: E: event-based; C: continuous time series; U: update mode. obspyDMT is the only tool among the listed software packages that provides access to both FDSN and ArcLink (in a single command), and both event-based and time-continuous waveform data. "Update" mode for waveforms, response files and/or meta-data information is supported. obspyDMT manages the data download and archival to a user's local computer. Moreover, it offers instrument correction and a customisable processing unit. Diagnostic plots of data or meta-data can be generated by simple inclusion of an option flag. See text for further discussion.

The instrument response of a seismogram is normally provided by data centres in different formats, for example, the SEED format. SEED describes transfer functions of all components in a seismological measuring system including the analogue and digital stages; therefore, it can be used to calculate the frequency response function of a seismic channel ($T(j\omega)$ in eq. 2.3). In practice, this format is usually converted to human readable ASCII files called *SEED RESP* that can be read by other software (e.g., *evalresp*) to correct for instrument response. Recently, *FDSN* defined a new format *FDSN StationXML* which contains the most important and commonly used structures of *SEED* metadata in *XML* representation (FDSN, 2015). Compared to SEED, StationXML simplifies and adds clarification to station metadata, and all data centres which support *FDSN* web services deliver instrument responses in this format. For the rest of this section, we do not differentiate between SEED and StationXML since both formats contain required information to construct the complete frequency response function of a seismogram.

Instrument correction is a routine but non-trivial task. As mentioned above, data formats to deliver instrument response are largely standardised, and seismic analysis programs exist that are capable of removing these instrument responses from raw counts. The problem is the incorrect information often reported in response files.

Groos (2010) reported some inconsistencies in SEED instrument response meta-data and quantified their effects on instrument corrected seismograms. For example, he found that coefficients of asymmetric FIR filters are sometimes given in reverse order, while according to the SEED manual, they should be in forward order. This can cause unwanted delays to waveforms of up to 1 s. Another observed inconsistency by Groos (2010) is in delay time values of FIR filter stages. He observed that, in some cases, reported values in instrument response headers do not follow the SEED definition. According to the SEED manual, corrected filter delay times have to be positive; however, negative or zero values have been detected in response file of some stations which can result in serious errors (1 to 2 s time shift) in corrected waveforms (Groos, 2010). Six years after the publication of this report, such problems are still encountered in response files delivered by data centres.

To systematically check for inconsistencies in response files, diagnostic and plotting tools are included in obspyDMT. Fig. 2.5 shows an example for this. Spectra (amplitude and phase) of the analogue part of the instrument response are compared with the full response spectra for station XAN (network code IC). We refer to the transfer function of all stages as "full-resp", and the transfer function of the analogue part only as "PAZ". In the example of Fig. 2.5, the influence of digital stages can be observed only in the ampli-

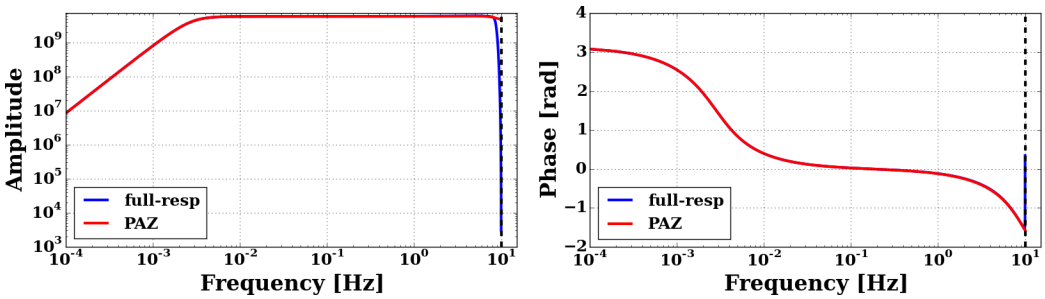

Figure 2.5: Transfer function spectra (amplitude and phase) of a Streckeisen STS-1VBB w/E300 station (IC.XAN) in China. Blue lines show transfer function components computed for all the stages in *StationXML* file; red lines are for the analogue part. The two functions match very well in all frequencies except for the amplitude spectra close to the Nyquist frequency (dashed line).

tude response spectrum close to the Nyquist frequency. In this case, where the desired frequency content is well below the Nyquist frequency, removing only the analogue part of the instrument response would be sufficient.

A similar comparison between the analogue and full response spectra of station LBTB (network code GT) is shown in Fig. 2.6. In this example, a significant discrepancy exists between the phase spectra of analogue part ("PAZ") and full transfer function of the system ("full-resp"). obspyDMT automatically detects such disagreements between "PAZ" and "full-resp" and creates diagnostic reports. At the same time, obspyDMT plots the transfer function of all stages separately in one figure for further investigation by the user. Fig. 2.7 shows this for station GT.LBTB. The phase spectra of two stages (1 and 5) are non-zero. In the "PAZ" phase spectrum of Fig. 2.6, the effect of stage 5 are not considered, which resulted in the observed discrepancy between the "PAZ" and "full-resp". Also, note the amplitude spectrum of stage 5 in Fig. 2.7 close to the Nyquist frequency: similar to the IC.XAN example, the effects of the digital stages on the amplitude spectrum are apparent only close to the Nyquist frequency.

Following the analysis of Groos (2010), obspyDMT also checks for inconsistencies in the "Estimated delay" and the "Correction applied" of the digital filter stages in the instrument response. In modern data loggers, these two values are usually similar, as delay times are removed from the waveforms internally. However, discrepancies have been observed, such as negative or zero values for the corrected delay time. In the example of Fig. 2.6, the estimated delay is reported as 0.63 s, and the applied correction is 0.0 s. obspyDMT

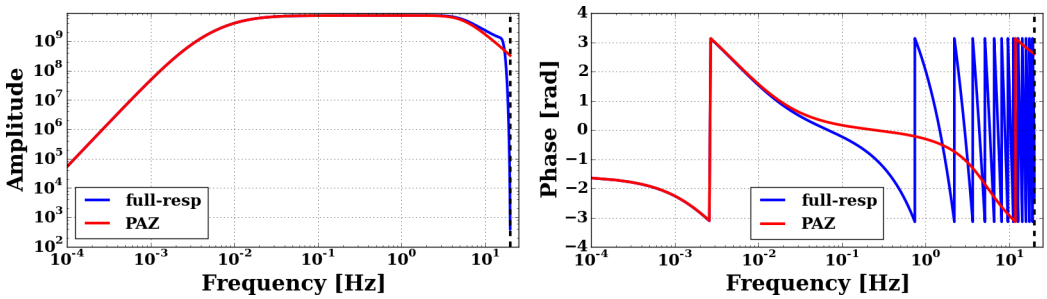

Figure 2.6: Transfer function spectra (amplitude and phase) of a Geotech KS-54000 Borehole seismometer (GT.LBTB) in Botswana, Africa. Blue lines show transfer function components computed for all the stages in the *StationXML* file; red lines are for the analogue part. There is a large discrepancy between the phase spectra of the two transfer functions. The deviation starts to emerge at frequencies around 10^{-2} Hz and increases up to the Nyquist frequency. Fig. 2.7 shows that this difference is caused by one of the digital stages in the instrument response.

collects this information and automatically generates one diagnostic report for the results of all consistency checks.

The above analysis suggests that to account for the amplitude and phase spectra of the instrument responses, all filter stages need to be considered. However, known inconsistencies exist in instrument response files, particularly in the digital anti-alias filter stages, due to false information reported by station operators. These can cause serious but hardly recognisable errors in corrected waveforms (Groos, 2010). obspyDMT's diagnostic tools can help to identify these instrument responses. This is particularly advantageous for large data sets, where manual analysis of individual response files is not feasible.

obspyDMT applies instrument correction using ObsPy's utility functions built for this purpose. It supports the deconvolution of both full and analogue instrument responses. These corrections and any other processing steps can be applied to waveforms either automatically after data retrieval or as a separate step. Since the deconvolution is a numerically expensive process, obspyDMT offers parallelisation. On shared memory multi-core systems (e.g., desktop processors) it can be activated by the simple inclusion of an option flag.

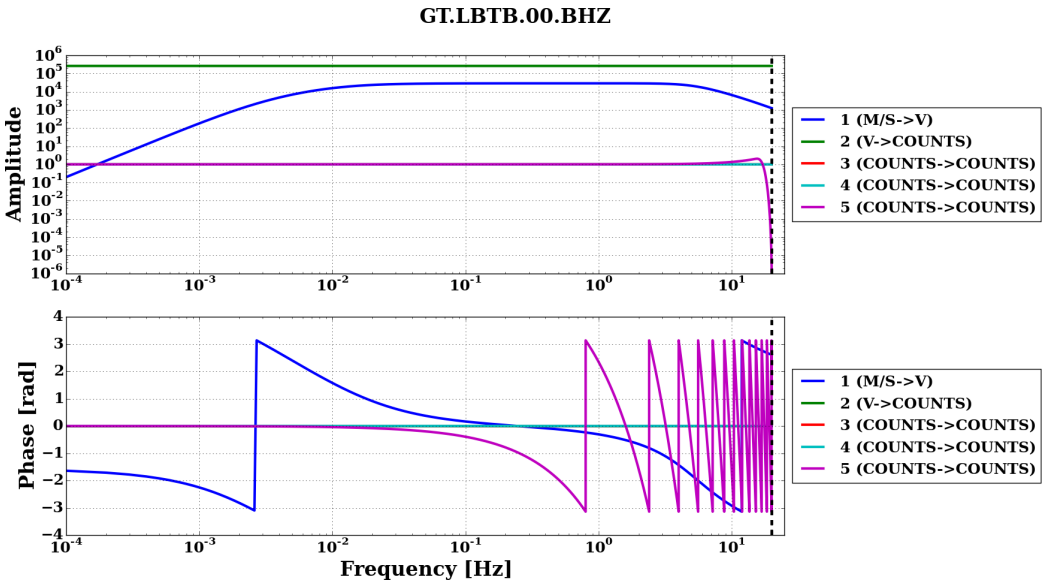

Figure 2.7: Transfer function spectra (amplitude and phase) of each stage in the *StationXML* file of a Geotech KS-54000 Borehole seismometer (GT.LBTB) in Botswana, Africa. In the phase response, two stages (1 and 5) have non-zero values in the considered frequency range. Both stages contribute to the phase spectrum of the complete instrument response ("full-resp") of Fig. 2.6. However, effects of stage 5 on amplitude and phase spectra are not considered in "PAZ" (analogue).

2.4 Synthetic seismograms

obspyDMT organises meta-data information and logfiles of each retrieved and processed data set into standardised directory trees. The stored information can then be used to link an archived data set to other codes. A practical example for this is multiple-frequency tomography. In this method, frequency-dependent observables (phase shifts or amplitudes) are measured by cross-correlating the recorded waveforms with the corresponding synthetic seismograms in multiple frequency bands (Sigloch, 2008; Zaroli et al., 2015; Hosseini and Sigloch, 2015). Synthetic seismograms need to be computed for exactly the same sources and receivers in the data set. This includes source characteristics (epicenter, depth, moment tensor and source time function) and the receiver's geometry (latitude, longitude, elevation and burial).

obspyDMT stores station information in one ASCII file for each event and in the SAC headers (if this format is selected). It automatically updates meta-data information and logfiles of a local data archive if stations are added/removed. Event information is written in QuakeML and ASCII formats. Note that although source and receiver basic information can be retrieved from most data centres, moment tensor solutions and half duration are available in only specific seismicity catalogues. obspyDMT supports *NEIC* and *GCMT* catalogues that include these information. As an example, focal mechanisms of a subset of earthquakes in Japan region queried from the *GCMT* are plotted in Fig. 2.8. In this seismicity map, earthquakes with magnitudes exceeding 5.0 that occurred between 1976 and 2014 are considered.

obspyDMT calculates the half duration of an earthquake on-the-fly based on its magnitude, if the information is not retrievable from the data centre. To have a relation between magnitude and half duration, analytical representations are derived from archived earthquakes in the *GCMT* catalogue as shown in Fig. 2.9. In this figure, three groups of events are selected: 1976-2014, 1976-1990 and 2005-2014, and three exponential functions are fit to each group. The coefficients are stored, and obspyDMT uses them to calculate earthquake's half duration from its magnitude, in case it is not provided by the data centre.

By using stored meta-data information of source and receivers in each directory, corresponding synthetic waveforms can be calculated using forward modelling tools. Here, we use *Instaseis* (van Driel et al., 2015) to generate synthetic waveforms. *Instaseis* allows for near-instantaneous extraction of arbitrary seismograms from databases generated by *AxiSEM* (Nissen-Meyer

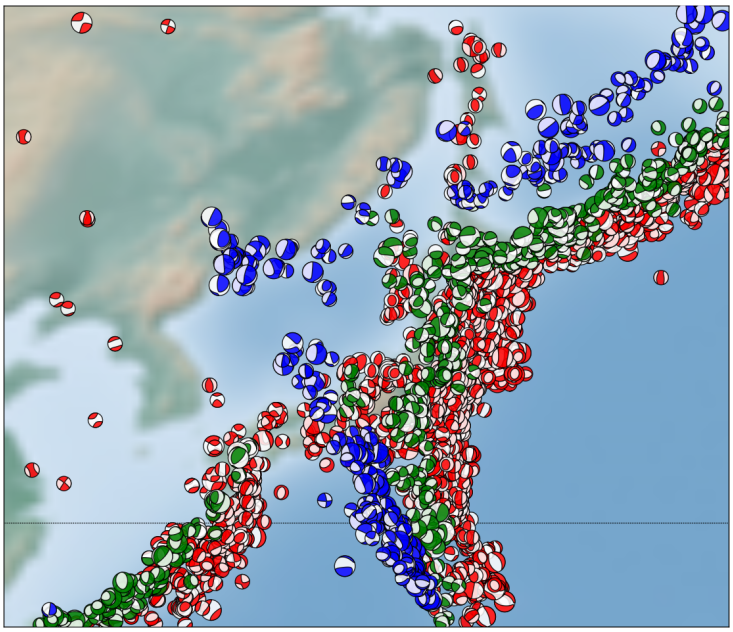

Figure 2.8: Geographical distribution of earthquakes (seismicity) in the Japan region. Only earthquakes with magnitude more than 5.0 that occurred between 1976 and 2014 are queried from the GCMT catalogue (resulting in $\approx$ 3,300 earthquakes). In addition to epicenter and depth information, obspyDMT can retrieve focal mechanisms from *NEIC* and *GCMT* as visualised here. Note the rendering of coloured beach balls in the map (deepest seismicity in the foreground). Red: 0-70 km; green: 70-300 km; blue: $\geq$300 km.

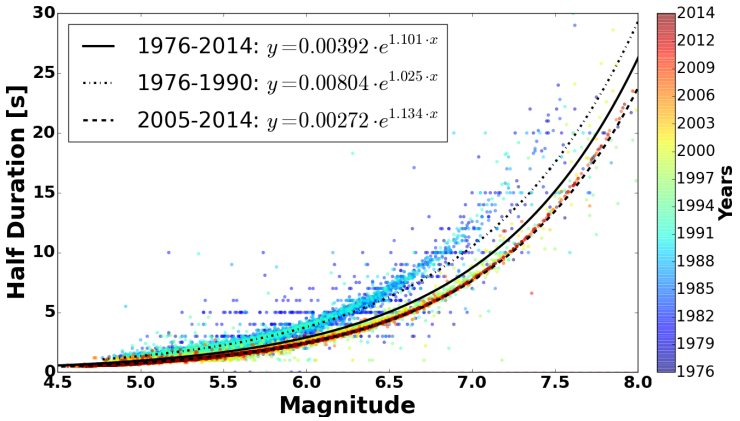

Figure 2.9: Magnitude and half duration of all archived earthquakes in the *GCMT* catalogue since 1976. Three groups are selected: 1976-2014, 1976-1990 and 2005-2014. For each group, an analytic representation is found by fitting an exponential function to the data. This way, obspyDMT can estimate half-duration of an earthquake from its magnitude, in case that it is not available in the seismicity catalogue.

et al., 2014), and it is a convenient method for generating global synthetic waveforms efficiently.

Fig. 2.10 shows the results for an example data set. The local data archive contains an earthquake with magnitude 6.9 *Mw* in the Fiji Islands Region (2014/07/21 14:54:41, at 19.802°S, 178.4°W, 615 km depth). We queried the IRIS DMC about hour-long, vertical broad-band (BHZ and HHZ) waveform segments that could be obtained for this earthquake. Instaseis was then used to compute synthetic waveforms based on stored meta-data information of earthquake and stations in the data set.

2.5 Conclusion

We presented obspyDMT, a new software for query, retrieval, processing and management of (large) seismological data sets. Its functionality, design and technical implementation were described and compared with existing seismological data retrieval and management tools. We listed its main functionalities, such as query of station and earthquake source (full moment tensor and event origin) meta-data, retrieval of actual event-based or time-continuous waveform data from various data centres in one command line, update mode, customisable processing unit, and automatic organisation of (meta-)data and

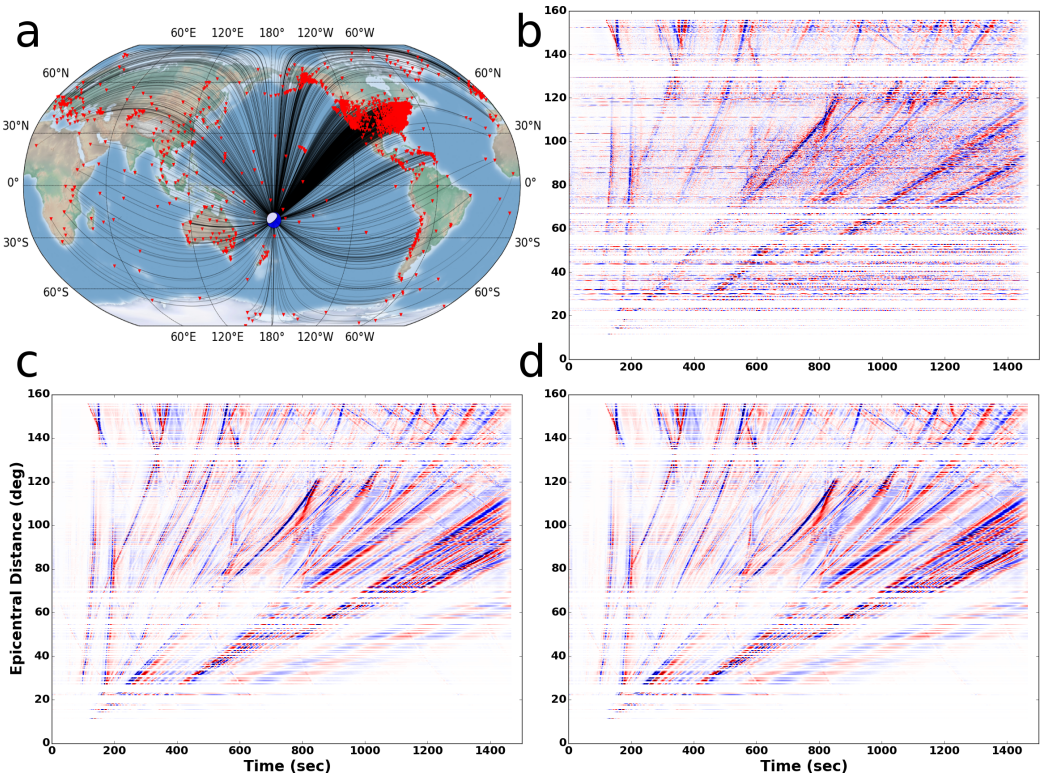

Figure 2.10: Observed versus modelled broad-band seismograms for an earthquake with magnitude 6.9 *Mw* in the Fiji Islands Region (2014/07/21 14:54:41, at 19.802°S, 178.4°W, 615 km depth). obspyDMT saves source and receiver meta-data information in a pre-defined structure. This way, local data holdings can be seamlessly linked to other external software. (a) Ray coverage map generated with the plotting tools of obspyDMT. (b) Observed broad-band waveforms aligned on their ray-theoretical P and Pdiff arrival times. Each line shows a seismogram (vertical component) filtered between 200 and 2 s. Positive samples are blue, negative samples are red. (c) Broad-band Green's functions calculated with *Instaseis* using stored meta-data information of the data archive. (d) Broad-band synthetics, the convolution of the Green's functions in panel (c) with the source time function generated based on the earthquake's half duration.

logfiles into standardised directory trees. In all these use cases, issuing a single line command is the only requirement for the end user, everything else is done automatically. At the same time, the user is provided with powerful diagnostic and plotting tools to check the retrieved data and meta-data information. For large seismological data sets, data retrieval and processing can be parallelised on multi-core architectures by the simple inclusion of an option flag. Using obspyDMT's diagnostic plots of analogue and digital filter stages, we checked the spectra (amplitude and phase) of two example response files. Moreover, synthetic seismograms of a data set were computed based on obspyDMT's automatically organised meta-data information.

3

Multifrequency measurements of core-diffracted P waves (Pdiff)

Abstract

The lower third of the mantle is sampled extensively by body waves that diffract around the earth's core (Pdiff and Sdiff phases), which could deliver highly resolved tomographic images of this poorly understood region. But core-diffracted waves – especially Pdiff waves – are not often used in tomography because they are difficult to model adequately. Our aim is to make core-diffracted body waves usable for global waveform tomography, across their entire frequency range. Here we present the data processing part of this effort. A method is demonstrated that routinely calculates finite-frequency traveltimes of Pdiff waves by cross-correlating large quantities of waveform data with synthetic seismograms, in frequency passbands ranging from 30.0 to 2.7 s dominant period. Green's functions for 1857 earthquakes, typically comprising thousands of seismograms, are calculated by theoretically exact wave propagation through a spherically symmetric earth model, up to 1 Hz dominant period.

Out of 418,226 candidates, 165,651 (39.6%) source-receiver pairs yielded at least one successful passband measurement of a Pdiff traveltime anomaly, for a total of 479,559 traveltimes in the

eight passbands considered. Measurements of teleseismic P waves yielded 448,178 usable source-receiver paths from 613,057 candidates (73.1% success rate), for a total of 2,306,755 usable teleseismic dT in eight passbands. Observed and predicted characteristics of Pdiff traveltimes are discussed and compared to teleseismic P for this very large data set.

Pdiff measurements are noise-limited due to severe wave attenuation with epicentral distance and frequency. Measurement success drops from 40-60% at 80° distance, to 5-10% at 140°. Frequency has a 2-3 times stronger influence on measurement success for Pdiff than for P. The fewest usable dT measurements are obtained in the microseismic noise band, whereas the fewest usable teleseismic P measurements occur at the highest frequencies. dT anomalies are larger for Pdiff than for P, and frequency dependence of dT due to 3-D heterogeneity (rather than just diffraction) is larger for Pdiff as well. Projecting the Pdiff traveltime anomalies on their core-grazing segments, we retrieve well-known, large-scale structural heterogeneities of the lowermost mantle, such as the two Large Low Shear Velocity Provinces, an Ultra-Low Velocity Zone west of Hawaii, and subducted slab accumulations under East Asia and Central America.

3.1 Introduction

Core-diffracted waves are seismic body waves that dive deep enough to sense the earth's core, and by interaction with this boundary become dispersive. In ray-theoretical modelling, the transition from teleseismic to core-diffracted wave occurs at the epicentral distance where the deepest ray segment no longer turns in the mantle, but starts to graze the core-mantle boundary (CMB). For P waves, this happens at ≈98° epicentral distance if source and receiver are located near the surface. In reality, ray theory is a poor approximation of the true, finite-frequency sensitivity of a core-diffracted wave, which resembles a spatially extended banana in the mantle, but flattens elliptically on top of the CMB due to diffraction (Liu and Tromp, 2008). Actual body waves already sense the core when the banana's lower lobe extends to the CMB, which happens at significantly smaller distances than 98°.

Core-diffracted waves, and Pdiff waves in particular, have been used to study lowermost mantle structure (Su and Dziewonski, 1997; Masters et al., 2000; Ritsema and van Heijst, 2002; Li et al., 2008), but they have seen very

little use in tomography, despite being the most highly resolving wave type that extensively samples the lower third of the mantle. The problem is that modelling their wave propagation and non-ray-like sensitivities to a reasonable approximation is challenging, requiring computationally expensive forward modelling techniques. Global P wave tomographies often include data in the far teleseismic range, which effectively start to sense the core (generally neglected by the sensitivity modelling), but they stop short of including "real" Pdiff data. Sparser sampling and poorer modelling result in coarser image resolution and significant discrepancies across tomographic models, even for large-scale features. Hence, our knowledge of structural detail in the lowermost mantle is lacking compared to shallower levels. For example, many regional and global tomographies have proposed detailed tectonic or paleogeographic interpretations of slab geometries imaged at upper and mid mantle depths (e.g. for Tethyan slabs:Van der Voo et al. (1999b); Hafkenscheid et al. (2006); for North America: Grand (2002); Ren et al. (2007); Pavlis et al. (2012); Sigloch and Mihalynuk (2013); globally: Li et al. (2008); van der Meer et al. (2010)). The same has rarely been attempted for slabs in the lower third of the mantle (Van der Voo et al. (1999a); van der Meer et al. (2010)), despite agreement between virtually all global tomography models that extensive fast-velocity provinces are present at these depths.

To our knowledge, the only global P wave tomographies to explicitly model and include Pdiff traveltime data were by Wysession (1996a) and Kàrason and Van der Hilst (2001), both using a set of 543 differential Pdiff-PKP measurements. Wysession (1996a) treated the mantle path by ray theory and sensitivity at the CMB by an approximate elliptical Fresnel zone of constant value. Kàrason and Van der Hilst (2001) improved on this by constructing approximate 3-D sensitivity kernels instead of assuming a constant Fresnel zone, and inverted for 3-D mantle structure rather than a 2-D map of velocity anomalies on the CMB. Resolution was obviously limited with only 543 measurements (compared to half a million presented here). The same kernels and data set were reused by Li et al. (2008).

A few global S-wave tomographies explicitly include Sdiff data. Ritsema et al. (2004, 2011) include cross-correlation traveltime measurements of SH-diff waves and model them by ray-theoretical sensitivities. Mégnin and Romanowicz (2000) and Panning and Romanowicz (2006) include SH-diff data in their waveform inversion, modelling sensitivities by mode coupling in the NACT approximation, which features spatially extended sensitivities in the source-receiver plane, but no sensitivity perpendicular to it. Wave periods in these models were limited to 30 s and longer.

Most global tomographies include non-diffracted wave types that sample the lowermost mantle, for example, core phases, core-reflected phases, long-

range teleseismic waves near the diffraction limit, or normal modes. The structural findings from these data have converged robustly on certain very large scale features in the lower mantle, such as Large Low Shear Velocity Provinces (e.g., Woodhouse and Dziewonski (1989); Masters et al. (2000); Mégnin and Romanowicz (2000); Grand (2002); Ritsema and van Heijst (2002); Montelli et al. (2006)), but resolution remains limited by the long wavelengths used and/or by modelling mismatches inherent in using approximate sensitivities.

We aim to improve on the state of the art as follows:

1. Model and measure core-diffracted body waves across their entire spectrum, up to the highest occurring frequencies. The goal is maximum spatial resolution.

2. "No data left behind": a processing strategy efficient enough to assemble the largest possible data sets (Hosseini-zad et al., 2012).

3. Use of Pdiff in addition to Sdiff.

4. Better approximation of true wave sensitivities by 3-D Born-Fréchet kernels.

Items 1 and 2 aim for maximum spatial resolution and coverage globally. In terms of wave type, we started with Pdiff because it will integrate seamlessly with our teleseismic P wave inversions, but the processing methods presented here carry over to Sdiff with only minimal changes. For the ambitious data volumes, frequencies and distances targeted, fully numerical modelling in global 3-D reference models (e.g., Komatitsch and Tromp (2002a)) remains well beyond reach, but the semi-analytical modelling of 3-D wave fields and sensitivities in spherically symmetric earth models is becoming feasible. We discuss the forward modelling of core-diffracted seismograms, deferring the calculation of Born-Fréchet sensitivity kernels to Chapter 4.

Section 3.2.1 introduces the observational characteristics of Pdiff waves: strong dispersion and attenuation as functions of frequency and epicentral distance. Section 3.2.2 describes our successful adoption of two recent numerical packages for computing broad-band Green's functions: *Yspec* (Al-Attar and Woodhouse, 2008) and *AxiSEM* (Nissen-Meyer et al., 2014). In practice, the success of fitting broad-band waveforms depends not only on accurate Green's functions but equally on reliable estimates of source time functions and source depths. We compute traveltime measurements by cross-correlation in multiple frequency bands – essentially frequency-dependent phase shifts. Section 3.3 analyses the global data set of multifrequency traveltimes obtained so far: 479,559 P-diffracted and 2,306,755 teleseismic P

measurements. We discuss how measurement success depends on epicentral distance, frequency band and earthquake magnitude. The statistics of traveltimes for Pdiff and teleseismic P are presented, including their frequency dependence. The information content of the novel Pdiff measurements is demonstrated by projecting traveltime anomalies on the core-grazing segments of their nominal ray paths. Already from this "proto-tomography" exercise, structural heterogeneity of considerable detail emerges, which in Section 3.4 is compared to current structural knowledge about the lowermost mantle.

3.2 Waveform data and processing methods

3.2.1 Waveform recordings of core-diffracted P waves

We start by discussing the nature of P-diffracted waves. As the travel distance of a teleseismic P wave increases and transitions into the core-diffracted regime, the character of the waveform changes. Fig. 3.1 illustrates this for broad-band data from a deep earthquake of magnitude 7.5 in Southern Sumatra (2009/09/30 10:16:09, 0.72°S, 99.87°E, depth: 82.0 km). Sharply defined pulses recorded in the teleseismic distance range ($\Delta < 90°$) morph into increasingly emergent oscillations at distances exceeding 100°. This is clearly observable for the isolated (blue) P pulse arrival in the real data (Fig. 3.1a), and even more evident in the modelled Green's functions of Fig. 3.1c. (Broad-band Green's functions were computed with the *Yspec* software of Al-Attar and Woodhouse (2008), described in Section 3.2.2.) At ranges $\Delta < 100°$, two surface phases pP and sP (in red) are clearly distinguished 20-40 s after the P arrival, whereas in the Pdiff range these two pulses are smeared together. In other words, high-frequency content is lost disproportionately with distance in the core-diffracted range, while this is not the case in the teleseismic range. The increasingly emergent and lowpassed character of the Pdiff pulses in Figs 3.1(a)-(c) indicates that ray-theoretical processing methods such as manual or automated onset picking would be inadequate because they rely on sharp, impulsive onsets. The emergent onsets are a manifestation of the different physics of diffracted wave propagation, for which the ray-theoretical approximation breaks down.

The dependence of wave amplitude on source-receiver distance is not apparent in Fig. 3.1 because each trace is energy-normalised, but it differs fundamentally between P and Pdiff (Knopoff and Gilbert, 1961; Sacks, 1966). In a computational experiment, we calculated broad-band Green's functions as in Fig. 3.1c, except that an explosive source was used, 100 km deep in

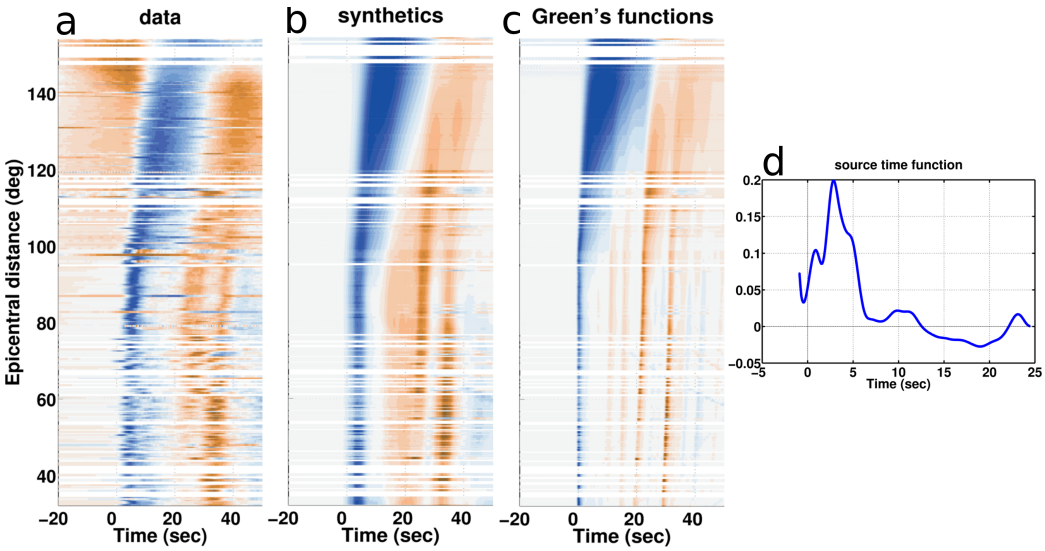

Figure 3.1: Observed versus modelled broad-band seismograms of teleseismic and core-diffracted P waves. Record section of a deep magnitude 7.5 earthquake in Southern Sumatra (2009/09/30 10:16:09.2, at 0.72°S, 99.87°E, 82 km depth), recorded on seismic networks globally. (a) Observed broad-band waveforms aligned on their ray-theoretical P-arrival times. Each line shows a seismogram (vertical component) of normalised RMS amplitude, from 20 s before to 50 s after P-arrival; positive samples are blue, negative samples are red. Waveforms include the direct P phase (blue), and in its wake the pP and sP surface reflections (red). The Pdiff epicentral distance range >120° is particularly densely sampled by several hundred USArray stations. The increasingly broad and emergent pulses beyond distances of 100° result from diffraction around the earth's core. Red samples preceding the P-arrival are a filter response resulting from highpass filtering at 100 s corner period, which serves to suppress low-frequency noise. (b) Broad-band synthetics, the convolution of the Green's functions in panel (c) with the source time function in panel (d). (c) Broad-band Green's functions (up to 1 Hz dominant period) computed in a spherically symmetric earth model by the *Yspec* method of Al-Attar and Woodhouse (2008). (d) The broad-band source time function (amplitude normalised), which was deconvolved from panels (a) and (c).

order to cleanly isolate the P pulse from its echoes. The vertical component waveforms were filtered to eight overlapping frequency passbands with dominant periods ranging from 30.0 to 2.7 s. (The filters are used throughout this study and described in Section 3.2.3.) RMS amplitudes of the bandpassed Green's functions were measured at epicentral distances from 40° to 150° in increments of 1°.

Fig. 3.2 shows the result: with increasing travel distance, amplitudes drop much more severely for Pdiff than for P. This is true in any frequency band, but particularly pronounced for high frequencies. Straight lines in this lin-log plot indicate exponential loss of energy with distance, the negative line slope being the attenuation constant in the exponent. Slopes in the P-diffracted range are steep and strongly dispersive – in the far Pdiff range, higher frequencies can be suppressed by orders of magnitude. This creates a signal-to-noise challenge for Pdiff measurements, and Section 3.3.1 investigates its practical consequences.

The Pdiff slopes of Fig. 3.2 are found to be in good agreement with analytical predictions of (Aki and Richards, 2002, p. 457), superimposed as dash-dotted lines. They predict the amplitude A of core-diffracted P waves to be proportional to

$$A \propto \exp\left[-\omega^{1/3}\lambda \sin(\pi/3)(\Delta_0 - \Delta_d)\right] \tag{3.1}$$

where ω is the angular frequency, λ is a positive constant and Δ_0 is the source-receiver distance. In the teleseismic range, the P and PcP pulses approach each other in time with increasing Δ_0 until they merge at Δ_d, which is called the shadow boundary. Beyond Δ_d, the rays start to creep around the CMB as diffracted P waves. With increasing frequency and/or distance (both in the exponent), the wave amplitude of Pdiff attenuates rapidly. To create the dash-dotted lines in Fig. 3.2, we estimated the constant λ by fitting above analytical solution to our results for the highest frequency band (2.7 s). This λ value was then used to calculate slopes for the other two frequency bands (5.3 s and 10.6 s), and the result is very consistent with the prediction.

Compared to the core-diffracted distance range, amplitude decrease in the teleseismic range is moderate, caused mainly by geometrical spreading. Intrinsic attenuation – in the real earth and in this simulation – does cause exponential loss of amplitude with travel distance and with frequency, but in practice the effect is mild (the coloured lines barely diverge), thanks to relatively low intrinsic attenuation in the mantle.

The transition from the P to the Pdiff regime in Fig. 3.2 occurs at a significantly smaller distance than predicted by ray theory. The second dashed line, around 98°, marks the predicted onset of core-grazing rays for the deep

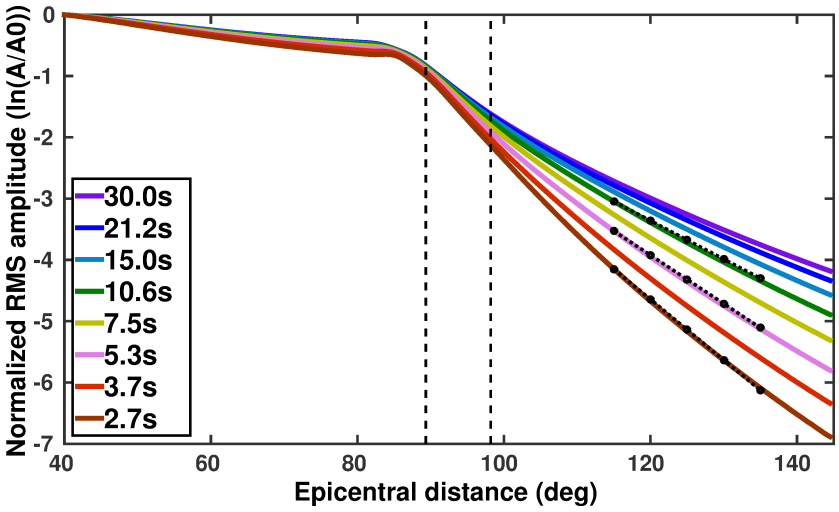

Figure 3.2: P-diffracted waves are highly attenuative and dispersive compared to teleseismic P waves – the effect of diffraction around the earth's core. As a function of epicentral distance, the logarithmic RMS amplitudes $\ln(A/A_0)$ of Green's functions are plotted. (Explosive source, 100 km deep, vertical receiver component, computed up to 1 s dominant period in velocity model IASP91 including PREM attenuation.) Coloured lines distinguish eight frequency passbands, labelled by their dominant periods. Amplitudes A in each band are normalised to the amplitude A_0 of a P wave at 40°distance. In this lin-log plot, straight lines indicate exponential loss of wave amplitude with distance, and negative line slopes represent the attenuation constants in the exponent. Divergence of coloured lines in the Pdiff range indicates frequency dispersion. Dash-dotted slopes are ray-theoretical predictions (Aki and Richards, 2002, p. 457), vertical dashed lines predict the distances at which a ray-theoretical P wave would first hit the D'' and the CMB, respectively.

source depth used (100 km depth). However, waves in our physically more realistic simulation have volumetrically extended, banana-like sensitivities to mantle structure, and start to sense the core at distances as small as 85°. "Teleseismic" waves at those distances are not well modelled by ray theory.

3.2.2 Modelling core-diffracted waves

Broad-band waveform tomography on a global scale has three modelling requirements:

1. Green's functions;
2. source time functions;
3. sensitivity kernels.

The main obstacle to exploiting core-diffracted waves has been modelling them to a sufficiently realistic degree. We employ recently developed, semi-analytical tools for forward wave propagation and discuss the computation of Green's functions and source time functions. Sensitivity kernels are required for inversion of the data in a linearized optimisation problem. (Unless global search approaches are used, which only rely on a large number of forward calculations but are computationally out of reach for the number of parameters required in 3-D inversions.) Tomographic inversion of our Pdiff data will be the topic of the following chapters, but we briefly discuss how the numerical tools for Green's function and kernel computations relate.

An observed seismogram is the convolution of an earthquake's source time function with the earth's Green's function between a given source-receiver pair. Waveform tomography compares this to a predicted seismogram, which is a Green's function computed in a reference earth model convolved with an estimate of the earthquake's source time function. Fig. 3.1 shows a typical broad-band data example for observed seismograms (Fig. 3.1a) and their predicted counterparts (Fig. 3.1b), which in turn are the convolution of the computed Green's functions (Fig. 3.1c) with a source time function estimate (Fig. 3.1d).

3.2.3 Green's functions

We compute Green's functions by simulating wave propagation in a broad-banded spectrum from 0.2 mHz to 1 Hz in the spherically symmetric earth model IASP91 (Kennett and Engdahl, 1991) with density and attenuation from PREM (Dziewonski and Anderson, 1981).

Two numerical software packages are suitable for these calculations: *Yspec* (Al-Attar and Woodhouse, 2008) and *AxiSEM* (Nissen-Meyer et al., 2007, 2014). *Yspec* is very efficient for calculating synthetic seismograms in spherically symmetric earth models using the direct radial integration method (Woodhouse, 1980; Friederich and Dalkolmo, 1995), which can account for the full physics of such media including viscoelastic damping (used here) and transverse isotropy (not used here). *AxiSEM* is a spectral-element code that computes 3-D global seismic wavefields for full moment tensor sources in viscoelastic (van Driel and Nissen-Meyer, 2014a), anisotropic (van Driel and Nissen-Meyer, 2014b) media across the observable frequency band at a reasonable computational cost.

Both *Yspec* and *AxiSEM* are semi-analytical methods that solve the full physics of wave propagation, but make use of the earth model's assumed spherical symmetry to analytically reduce the cost of computing 3-D wavefields – as compared to fully numerical simulations of wave propagation in 3-D heterogeneous earth models (e.g., Komatitsch and Tromp (2002a); Fichtner et al. (2009a)). Aside from numerical imprecisions, either approach computes 3-D wavefields that are theoretically exact within its modelling assumptions, but only the semi-analytical computations are efficient enough for our application.

Yspec and *AxiSEM* have been benchmarked against each other between 1 mHz and 1 Hz, yielding virtually indistinguishable seismograms (Nissen-Meyer et al., 2014). Since the implementation of attenuation and anisotropy in *AxiSEM* were not yet complete, all traces in this study were calculated with *Yspec*, which was very efficient for our forward modelling purposes. An example of its broad-band Green's functions is shown in Fig. 3.1c. *Yspec* took $\approx$ 480 CPU hours for our typical event of $\approx$ 3000 seismograms (1000 stations, 3 components), up to a dominant frequency of 1 Hz. This is an order of magnitude faster than *AxiSEM* for a single event. Computation scaled linearly with the number of sources, and we computed 2000 earthquakes for this study, expending a total of $\approx 10^6$ CPU hours. Sensitivity kernels are much more expensive to compute than Green's functions. For our present application, only *AxiSEM* is suitable for sensitivity kernel calculations thanks to its efficiency in computing and storing the spatiotemporal evolution of the 3-D wavefields. Hence, for the inversion stage, we will switch to *AxiSEM*.

AxiSEM and *Yspec* are semi-analytical, theoretically exact methods that include the full physics of wave propagation but exploit (spherical) symmetry in the background model for efficient computation. By contrast, our earlier studies used asymptotic (and therefore approximate) forward modelling methods, also assuming spherical symmetry. For teleseismic P measurements, Sigloch and Nolet (2006) used the WKBJ method of Chapman

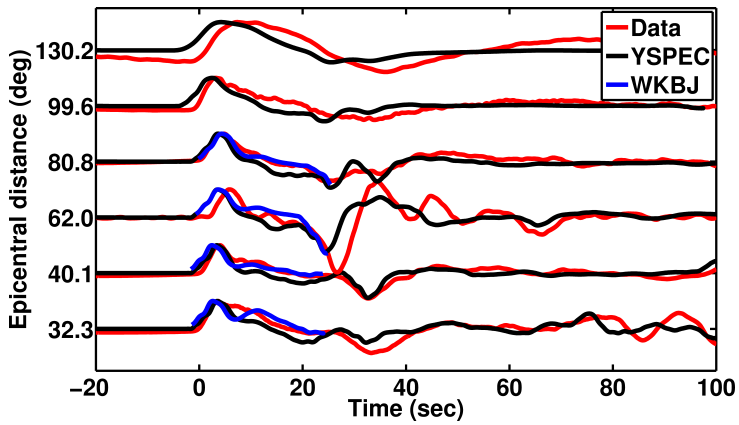

Figure 3.3: Broad-band waveform modelling, a comparison of methods for selected seismograms of the Sumatra event in Fig. 3.1. All synthetics for this study were computed by the semi-analytical *Yspec* software of Al-Attar and Woodhouse (2008) (in black) to a dominant period of 1 s. Our previous teleseismic studies used the asymptotic WKBJ method (blue), which is seen to be broadly consistent, but differs in detail and is not suited to computing core-diffracted waveforms. The broad-band observations are shown in red.

(1978); and for triplicated body waves, Stähler et al. (2012) used the reflectivity method by Fuchs and Müller (1971). Fig. 3.3 compares broad-band observations, WKBJ synthetics, and *Yspec* synthetics for the Sumatra event of Fig. 3.1. While agreeing in their basic characteristics, there are clear differences between WKBJ and *Yspec* synthetics in the teleseismic range, where both are applicable. (WKBJ does not compute core-diffracted waves.) Differences between *AxiSEM* and *Yspec* are much smaller (Nissen-Meyer et al., 2014) than the difference between *Yspec* and the asymptotic WKBJ method.

Source time functions

For fitting waveforms at the high frequencies included here, equally important as Green's functions are good estimates of earthquake source parameters, especially depth and source time function. This becomes clear on the data example of Fig. 3.1. Source depth determines the temporal spacing of the P, pP and sP pulses, a nonlinear effect that affects all frequency bands and is pronounced in practice, as depth estimates from earthquake catalogues are afflicted by large uncertainties. The source time function broadens and modulates the pulses – in this case, a ≈ 7 s long source time function convolves pulses spaced by about 20 s (P and pP) or 10 s (pP and sP), see Fig. 3.1c

versus Fig. 3.1b. This is the benign case of a 82-km deep earthquake, but most sources are shallower and their depth phases are smeared together by the source wavelet, in practice affecting all frequency bands of relevance to us.

No earthquake catalogue has been delivering source time function estimates, and hence we expend a significant effort on deconvolving them from data and Green's functions, in a linearized procedure described by Sigloch and Nolet (2006). For this study, source time functions for 1857 events since 1999 were deconvolved from teleseismic P waves and were subsequently used to calculate predicted seismograms at all distance ranges. As an important side benefit, this yields significantly more confident depth estimates than routine catalogue determinations – a parameter of great importance even for waveform tomography at relatively lower frequencies, where source time functions are somewhat less critical. On the downside, source deconvolution is currently the bottleneck of our processing chain because it requires the most human supervision. We are moving towards a more automated and fully probabilistic scheme (Stähler and Sigloch, 2014), with the goal of producing a community catalogue of source parameters for waveform tomography. Recently, the *SCARDEC* project has been publishing an increasing number of source time function solutions for current earthquakes, using the method of Vallée et al. (2011). For earlier years, we have been able to compare a limited subset to our own solutions and find them to be qualitatively consistent. A quantitative comparison is ongoing.

Multifrequency cross-correlation traveltimes for tomography

The measurement procedure for multifrequency traveltimes is again based on that for teleseismic body waves by Sigloch and Nolet (2006). A brief summary follows, highlighting Pdiff-related adaptations.

1. Processing proceeds earthquake by earthquake, typically on events exceeding magnitude $m_b > 5.5$. A pre-requisite is an estimate of the broad-band source time function (Section 3.2.3).

2. A predicted broad-band seismogram or *matched filter* for a receiver r at an arbitrary distance range is computed by convolving its broad-band Green's function (from *Yspec* or *AxiSEM*) with the event's broad-band source time function.

3. Broad-band observed and predicted seismograms are passed through the same filter bank of bandpass filters. We use Gabor filters in eight

overlapping frequency bands, with dominant periods ranging between 30.0 and 2.7 s (Fig. 3.4a).

4. The cross-correlation function between bandpassed observed and predicted waveforms is computed in each passband b. The time shift that maximises this function is defined to be the *finite-frequency traveltime anomaly* $dT_{r,b}$ (Dahlen et al., 2000). The tomographic inversion will use these traveltime anomalies as its measure of misfit, to be minimised in a least squares sense. $dT_{r,b}$ from all wave paths and frequency bands are required to jointly fit the (not frequency dependent) 3-D earth model solution.

Gabor filters are Gaussian functions in the log-frequency domain of constant fractional bandwidth and good spectral concentration characteristics. We space adjacent centre frequencies by $\sqrt{2}$, see Sigloch and Nolet (2006) for filter details. Fig. 3.4b demonstrates the filtering of observed and predicted Pdiff waveforms (broad-band data from the Sumatra event of Fig. 3.1) to three passbands in this filter bank. We do not go beyond 2.7 s dominant period because the number of successful fits becomes very small. Hence, it is effectively the nature and complexity of the real-world signal (shallow reverberations, uncertainty in source time function, etc.) that sets the upper frequency limit, rather than computational limitations (in fact our Green's functions are calculated up to 1 s dominant period).

Cross-correlation time windows are chosen as a fixed multiple of each filter's impulse response (IR) duration. Here we choose a length of 1.5*IR, marked by the vertical dashed line in Fig. 3.4. Empirically this choice yields robust results but other correlation window lengths are possible as long as sensitivity kernel computations mirror these choices. Cycle skipping is a potential problem in waveform cross-correlation, but we largely avoid it by first roughly aligning observed and predicted seismograms in the lowest frequency passband, and for the higher bands permitting only small time shifts relative to those initial lags. This indirectly exploits the broad-band nature of the signal to achieve more robust measurements.

As misfit measure for tomography, cross-correlation traveltimes have very favourable properties. They are robust in that cross-correlation or matched filtering is the optimal way of detecting a signal of known shape in white Gaussian noise (Sigloch and Nolet, 2006, and signal processing references therein). This robustness is important in environments of high ambient noise, such as Pdiff waves at long distance ranges and high frequencies. Cross-correlation traveltimes also retain a near-linear relationship to velocity model perturbations over a larger perturbation range than direct waveform differences (samplewise *L2* misfit) (Mercerat and Nolet, 2013).

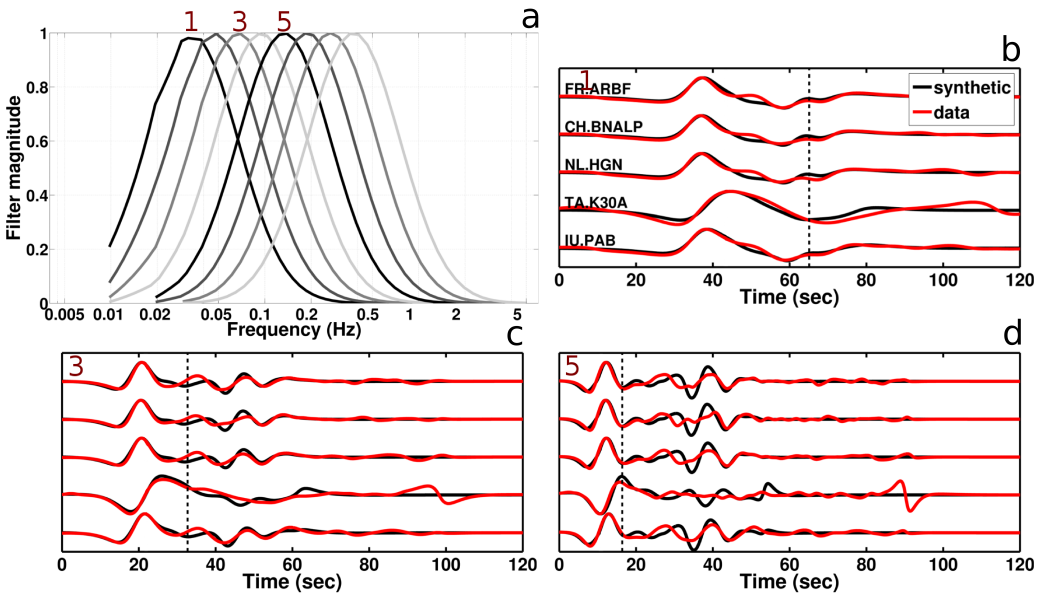

Figure 3.4: Procedure for multifrequency measurements of traveltimes. (a) Frequency responses of the eight bandpass filters used, Gabor filters of constant fractional bandwidth. Centre periods range from 30.0 to 2.7 s (0.033 to 0.37 Hz) and are spaced by factors of $\sqrt{2}$. (b) Selected observations (red) and *Yspec* synthetics (black) for the Sumatra event, filtered to the lowest frequency band, that is, 30.0 s dominant period. Dashed line marks 1.5 times the duration of each filter's impulse response, which we chose as the length of the correlation time window. The finite-frequency traveltime anomaly is defined as the time delay that maximises the cross-correlation of observed and predicted waveforms within this time window. (c) Same as (b), but filtered to 15 s dominant period (band 3). (d) Same as (b), but filtered to 7.5 s dominant period (band 5).

3.2.4 Pdiff wave dispersion caused by mantle heterogeneities

Interaction with the CMB makes P-diffracted waves dispersive in a spherically symmetric earth, in contrast to teleseismic P waves. However, in a planet with lateral velocity variations, dT observations of teleseismic P waves also become dispersive, provided their wave lengths are of the same length scale as the mantle heterogeneity they interact with (Nolet and Dahlen, 2000). Dispersion observed on Pdiff traveltimes will be a superposition of the two effects: diffraction around the core and finite-frequency effects caused by a 3-D heterogeneous earth.

Fig. 3.5 demonstrates the dispersion that arises from different spherically symmetric reference models. Besides the IASP91 model used throughout this study, we considered two models with differing velocity gradients in the D'' layer (2740-2899 km). The positive gradient model (blue in Fig. 3.5a) results in a P wave velocity at the CMB that is 2.8% faster than in IASP91. The negative gradient model (red) produces a 2.8% slower v_p at the CMB. The absolute gradient values were chosen as plausible regional variations from the global average of IASP91, following Thorne et al. (2013), who stated 2.8% as characteristic S-velocity variations in D'' (but tomographic models tend to underestimate dv/v, hence we adopted the full 2.8% for dv_p/v_p).

As expected, the fast gradient produces early arrival times compared to IASP91 (blue versus black waveforms in Fig. 3.5b), and the negative gradient produces delayed arrivals (red versus black waveforms). The advance and delay are 2.2 s and -2.3 s in the lowest frequency band (30 s period), and larger (3-4 s) in the higher frequency bands – this is traveltime dispersion caused by diffraction around the symmetric core. An actually observed Pdiff waveform (grey dashed, from the example M_w=7.5 Sumatra event to USArray station J23A, *cf.* map in Fig. 3.6a) shows the same sign of dispersion as the positive gradient model: increasingly early arrivals as frequency increases. This suggests an anomalously fast wave path in the lowermost mantle, for which IASP91 would be too slow a model – a plausible scenario for a core-grazing path beneath the northern Pacific (the blue path in Fig. 3.7a), because tomographic models generally infer an anomalously fast lowermost mantle beneath this region (e.g., Woodhouse and Dziewonski (1989); Masters et al. (2000); Mégnin and Romanowicz (2000); Grand (2002); Montelli et al. (2006); Ritsema et al. (2011)). The fast anomalies seem to be quite strong judging by the observed dispersion: with increasing frequency, the relative dT advance of the observed seismogram (dashed) w.r.t. to IASP91 is larger than for the fast gradient model (blue waveforms) w.r.t IASP91.

Fig. 3.6 investigates the magnitude of Pdiff traveltime dispersion that cannot be explained by spherically symmetric structure and must be due to

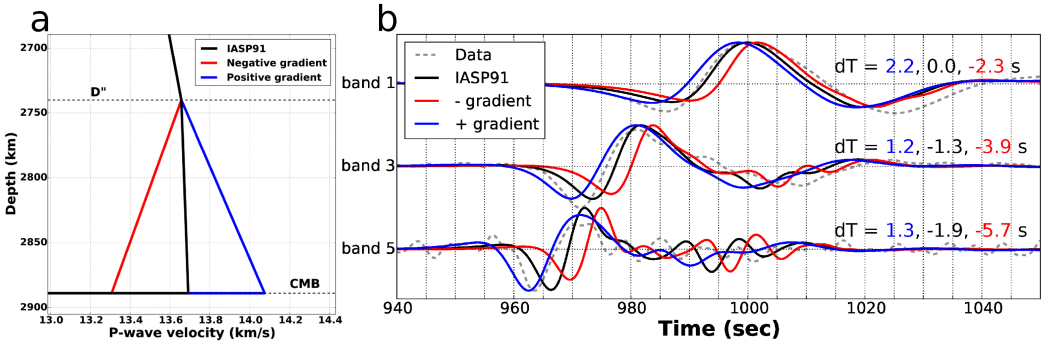

Figure 3.5: Observed and predicted traveltime dispersions of Pdiff, for different P-velocity models of the lowermost mantle. (a) P wave velocities in the D'' layer region according to spherically symmetric reference model IASP91 (black), and two perturbed models featuring linear gradients that result in 2.8% faster velocities at the CMB than IASP91 (blue), or 2.8% slower velocities (red). (b) Observed (dashed) and predicted Pdiff seismograms for a wave path from the example Sumatra event to a station at 131.7° epicentral distance (USArray station J23A, shown in Fig. 3.6a. This is the blue wave path in Fig. 3.7a). *Yspec* synthetics were calculated through IASP91 and the two alternative models, and are shown for frequency passbands 1 (dominant period 30.0 s), 3 (15.0 s) and 5 (7.5 s). Traveltime delays $dT = T^{\mathrm{obs}} - T^{\mathrm{syn}}$ of the observed (dashed) seismograms relative to the synthetics, as computed through the fast model (blue), IASP91 (black), and the slow model (red). A single floating time shift dT_0 between data and synthetics, which is due to uncertainties in absolute earthquake timing, has been arbitrarily fixed such that $dT_{\mathrm{IASP91}} = 0\ s$ in the lowest frequency band, that is, the observed arrival coincides with the IASP91-predicted arrival in this band (which facilitates visual comparison of the waveforms). The observed dT is dispersive: to higher frequencies (T = 30, 15 and 7.5 s) the dashed waveform arrives increasingly early (dT = 0.0, -1.3 and -1.9 s) w.r.t. IASP91. Comparison to the alternative models suggests a seismically fast wave path – the blue velocity profile produces dispersion of the same sign (increasingly advanced relative to IASP91), although of insufficient magnitude to explain this particular observation. See text for further discussion.

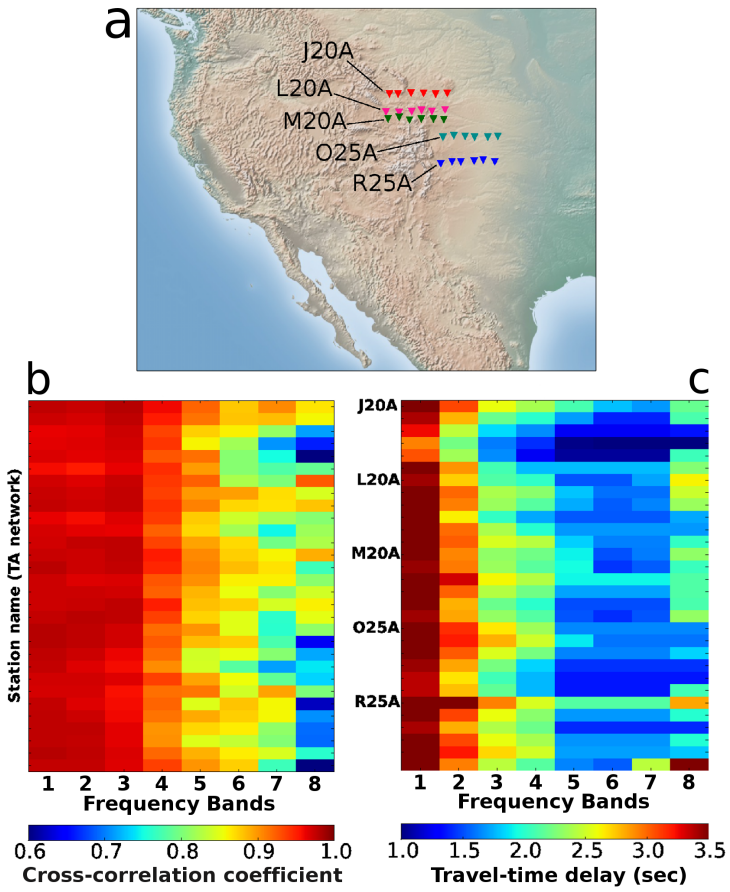

Figure 3.6: Example traveltime dispersion patterns for Pdiff waves, observed on a cluster of neighbouring USArray stations for the Sumatra event of Fig. 3.1. (a) 30 spatially neighbouring USArray stations grouped as five linear sub-arrays of constant latitudes J, L, M, O, R. (b) Each pixel shows the cross-correlation coefficient x_c (in colour) for one finite-frequency measurement. Stations in the same sub-array are grouped in neighbouring matrix rows. Most stations (30 rows) and frequency bands (8 columns) yielded measurements of sufficiently high quality ($x_c \geq 0.8$) for an interpretation of traveltime anomalies to be meaningful. The centre periods of frequency bands 1 to 8 are (in seconds): 30.0, 21.2, 15.0, 10.6, 7.5, 5.3, 3.7, 2.7. (c) Traveltime delays dT in seconds. A change of colour *within a row* indicates a frequency-dispersive wave path. Patterns that change from row to row cannot exclusively reflect a biassed reference model and must be partly due to 3-D heterogeneity somewhere along the wave path. A lowermost mantle contribution is suspected because the dispersion here exceeds the 0.1-0.3 s typically observed for teleseismic P waves by Sigloch and Nolet (2006). However, the columnwise "banded" structure of very large delays in the lowest bands is probably due either to IASP91 being a biassed reference model (*cf.* Fig. 3.5) or to imperfect ellipticity corrections for the Pdiff arrivals.

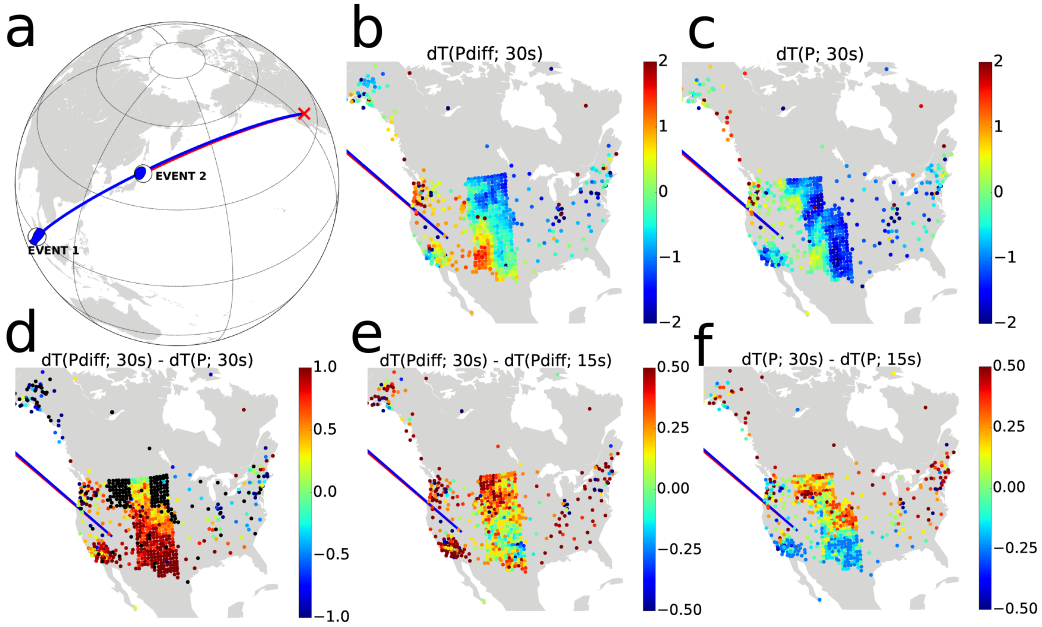

Figure 3.7: The signature of the lowermost mantle in traveltime measurements. (a) Comparison of two events at almost identical backazimuths from USArray. Event 1 occurred at core-diffracted distances (Southern Sumatra, Indonesia, 2009/09/30 10:16:09.25, 0.72°S, 99.87°E, 82 km depth, 7.5 Mw). Event 2 occurred at teleseismic distances (Hokkaido, Japan region, 2009/06/05 03:30:33.06, 41.82°N, 143.45°E, 28 km depth, 6.4 Mw). Panels (b)-(f) plot dT anomalies in seconds as coloured dots (note that the colour scale changes from panel to panel). Stations lacking data for one event or the other are marked in black. Corrections for ellipticity, crust and station elevation were applied. (b) Event 1, Pdiff traveltime anomalies in the lowest frequency band: $dT(\text{Pdiff}; T_d = 30\ s)$. (c) Event 2, P anomalies in the lowest frequency band: $dT(\text{P}; T_d = 30\ s)$. (d) Differential traveltimes in the lowest frequency band: $dT(\text{Pdiff}; T_d = 30\ s) - dT(\text{P}; T_d = 30\ s)$. This should subtract out most upper-mantle contributions. (e) Event 1, traveltime dispersion for Pdiff: $dT(\text{Pdiff}; T_d = 30\ s) - dT(\text{Pdiff}; T_d = 15\ s)$ (f) Event 2, traveltime dispersion for P: $dT(\text{P}; T_d = 30\ s) - dT(\text{P}; T_d = 15\ s)$.

3-D heterogeneity, using a cluster of stations in the vicinity of station J23A just discussed. Traveltime measurement results of our processing scheme are shown for a set of 30 spatially neighbouring USArray stations that recorded the M_w=7.5 Sumatra event. The 30 stations subdivide into 5 parallel lines {J, L, M, O, R}, each at constant latitude and featuring a station spacing of ≈70 km (Fig. 3.6a). Most wave paths yielded sufficiently high cross-correlation coefficients for dT results to be considered robust in at least the lower six frequency bands, from T_d=30.0 s to 5.3 s period – Fig. 3.6b.

The traveltime anomalies dT in Fig. 3.6c vary significantly across neighbouring stations – this could be mantle, crustal, or near-source effects. But the dT vary almost equally strongly with frequency – a colour change within a row indicates frequency dispersion and hence laterally heterogeneous 3-D structure somewhere on the wave path (rather than diffractive dispersion from the spherically symmetric core). 30 s to 7.5 s is a frequency window where dispersion is not expected to be dominated by reverberations in sediments (Zhou et al., 2003) or finite-frequency effects of heterogeneous crust (Ritsema et al., 2009) and should thus represent "useful" signal for mantle tomography. Frequency dependence of dT due to wave propagation in the crust is not modelled because we apply ray-theoretical crustal corrections, but the expected error is small. In continental crust of 35-45 km thickness beneath the stations in Fig. 3.6 (Bassin et al., 2000), the difference between ray-theoretical and true traveltime in the crust is predicted to be less than 0.1 s for the short wave periods ($T < 30$ s) used here (Ritsema et al., 2009). Unmodelled dT variations across neighbouring stations, which sit on a similar crust, would be even smaller.

The observed frequency dependence of Pdiff traveltimes in Fig. 3.6 is relatively strong compared to the typical 0.1-0.3 s observed for teleseismic P waves in this period range (Sigloch and Nolet, 2006). This suggests a significant contribution from heterogeneities in the lowermost mantle. To investigate further, Fig. 3.7 compares frequency-dependent dT recordings on USArray from two earthquakes at almost identical backazimuths: Event 1 at core-diffracted distance, Event 2 at teleseismic distance. Pdiff traveltime patterns in Fig. 3.7b resemble teleseismic traveltime patterns in Fig. 3.7c, suggesting an origin mostly in the upper(most) mantle and crust, which are sampled in similar geometries by both wave types.

Stationwise subtraction of dT of Event 2 from Event 1 (Pdiff minus P) should thus enhance the non-upper mantle contribution. Indeed the differential dT pattern in Fig. 3.7d is quite different. The systematic north-south gradient (green to red), more or less parallel to the event backazimuth and "banded" with epicentral distance, which may indicate that our spherically symmetric reference model needs adjustment, or may be a signature of the

elliptic earth (the dT have been corrected for ellipticity, though technically not completely correct for core-grazing waves (Kennett and Gudmundsson, 1996)). However, the pattern in Fig. 3.7d is not exclusively banded and contains additional 3-D signature, presumably of lower-mantle origin.

The last two panels show traveltime dispersion, where dT measured in the 30 s band is subtracted from dT in the 15 s band. Fig. 3.7e shows this for the diffracted data of Event 1, that is, $dT(\text{Pdiff}; T_d = 30\ s) - dT(\text{Pdiff}; T_d = 15\ s)$, and Fig. 3.7f for the teleseismic Event 2, that is, $dT(\text{P}; T_d = 30\ s) - dT(\text{P}; T_d = 15\ s)$. Such dispersion arises because wave sensitivity to mantle structure is frequency dependent (the size of the Fresnel zone relative to structural anomalies changes). Again the dT dispersion patterns should be similar if due to upper mantle structure, which is sensed similarly by both wave types, and different if caused by 3-D heterogeneities deeper down. The dispersion observations are seen to resemble each other in some aspects, but substantially differ in others (e.g., red in California for Pdiff, blue for P). Also, note the larger magnitude of dispersion (more intense colours) for Pdiff than for P. Hence, beyond the known, strongly dispersive signature of the *upper* mantle under USArray (Sigloch and Nolet, 2006; Sigloch, 2008), there seems to be a clear lower-mantle signature present to be exploited by Pdiff-tomography.

3.3 Global data set of multifrequency traveltime measurements

We present the global data set of P-diffracted and teleseismic P wave dT anomalies assembled so far, and assess the factors that determine measurement success: mainly source-receiver distance, source magnitude and frequency band. Measurement success is defined as the cross-correlation coefficient x_c between observed and synthetic waveforms exceeding $x_c \geq 0.8$ – a heuristic value obtained from earlier multifrequency inversions (Sigloch et al., 2008; Tian et al., 2009).

Fig. 3.8 shows the 1857 events and 4085 broad-band stations that contributed at least one usable measurement. 418,226 unique source-receiver paths for Pdiff yielded 479,559 successful, bandpassed Pdiff traveltime measurements. 613,057 unique paths for teleseismic P yielded 2,306,755 usable P wave traveltimes. Source and receiver coverage reflects our "No data left behind" philosophy, in that we considered every event of magnitude $m_b \geq 5.8$ that occurred between 1999 and 2010 – plus many earlier or smaller events if they occurred in unusual locations. Work is ongoing on the most recent

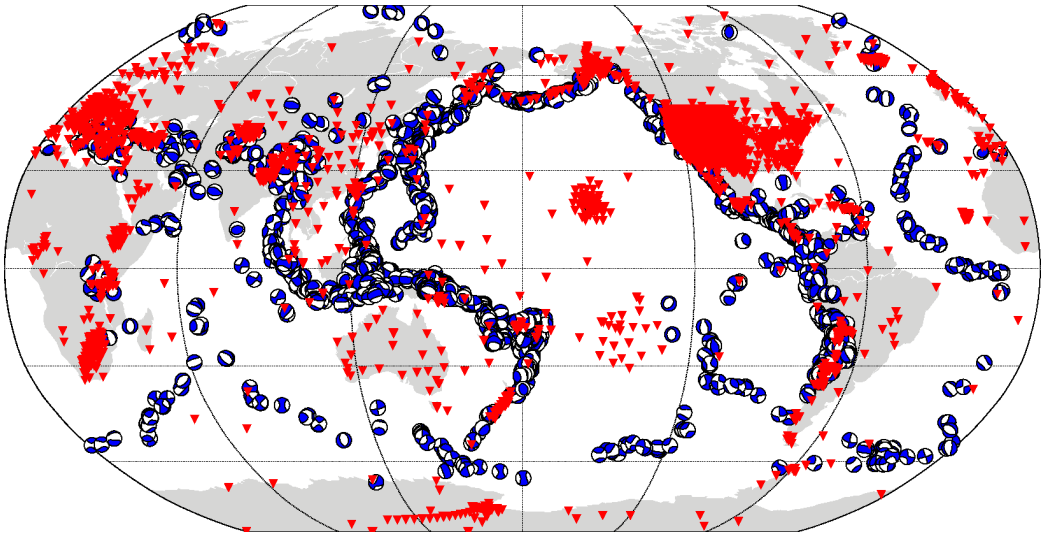

Figure 3.8: Global distribution of the 1857 earthquake sources (blue beachballs) and 4085 broad-band receivers (red triangles) used in this study. Each source and receiver contributed to at least one successful measurement ($x_c \geq 0.8$) in at least one frequency band. For each source, a broad-band source time function was deconvolved from the waveform data.

years, as the deconvolution of source time functions still requires human supervision.

The large volumes of broad-band waveform data were retrieved from the IRIS and ORFEUS data management centres using fully automated Python software built for this purpose: *ObsPyLoad* and its successor *obspyDMT*, freely available at `http://kasra-hosseini.github.io/obspyDMT` (hosted in *GitHub*, a community-standard repository) and described in Scheingraber et al. (2013). *obspyDMT* also executed the instrument correction to ground displacement, bandpass-filtering between 0.01 Hz and 3.5 Hz, local archiving, and updating of the collection when new waveforms became available on the IRIS and ORFEUS servers.

Green's functions for the 1857 events, in the broad spectrum of 0.2 mHz to 1 Hz and of 85 min duration, were computed with the *Yspec* software including attenuation (Al-Attar and Woodhouse, 2008). Per event, this took about 20 hr on 24 cores (480 core-hours). These Green's functions were convolved with source time functions for the 1857 events, obtained by the linearized method of Sigloch and Nolet (2006).

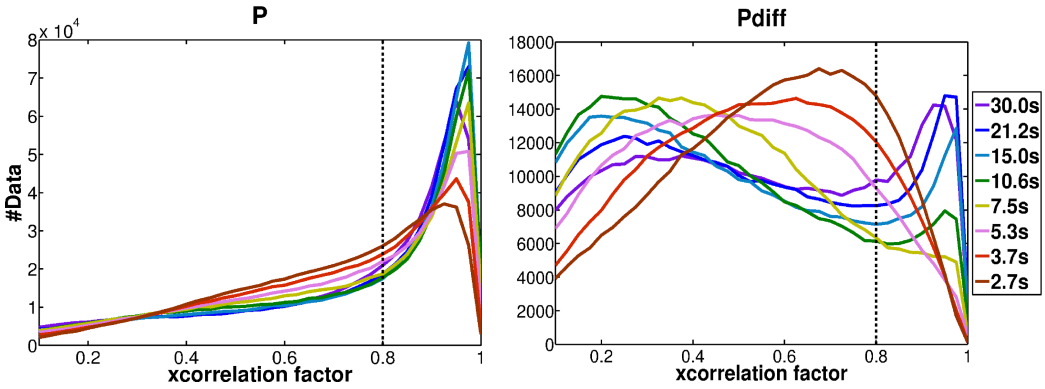

Figure 3.9: Histograms of measurement success for P versus Pdiff. The metric is the cross-correlation coefficient x_c, which from our experience should exceed $x_c \geq 0.8$ in order to be adequate for tomography. Left: histogram of x_c values achieved for teleseismic P-measurements (distance range 32°-95°) in each of the eight frequency passbands. The values peak well above $x_c > 0.9$, indicating highly likely measurement success. The higher the frequency, the fewer usable measurements are achieved. Right: same as left, but for Pdiff waves (distance range 97°-160°). Compared to teleseismic P, a much lower fraction of measurements achieves high $x_c \geq 0.8$, especially in the higher frequency bands, where diffraction dramatically lowers the signal-to-noise ratio.

3.3.1 Measurement success as a function of epicentral distance, source magnitude and frequency band

Fig. 3.9 shows histograms of the cross-correlations achieved in P- versus Pdiff measurements. High cross-correlations are more often achieved in the low-frequency passbands. This is true for both P and Pdiff, but significantly more pronounced for Pdiff, as expected from its frequency-dependent attenuation properties of Fig. 3.2.

At the chosen quality threshold of $x_c \geq 0.8$, the fewest successful P-measurements are made in the highest frequency band, whereas the fewest successful Pdiff measurements are made at dominant periods around 7.5 s, the band of the secondary microseismic noise. This becomes more evident in Fig. 3.10, which shows the number of successful measurements versus dominant period. For teleseismic P, the number increases with dominant period, whereas good Pdiff measurements are least common in the microseismic noise band (shaded yellow) rather than at the shortest periods.

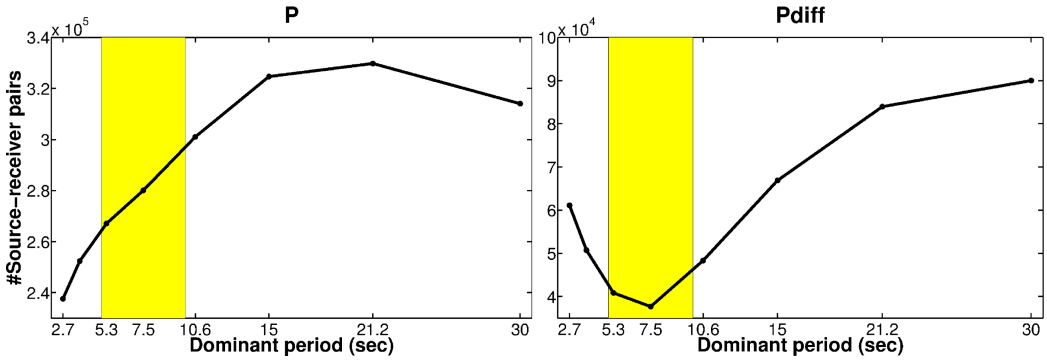

Figure 3.10: Histograms of satisfactory P and Pdiff measurements, as a function of frequency band. A measurement is included only if it achieved cross-correlation coefficient $x_c \geq 0.8$. Yellow shading marks the secondary microseismic noise band. Left: for teleseismic P waves, measurement success increases (almost) monotonously with wave period. Right: for Pdiff waves, measurement success is lowest in the band of the secondary microseismic noise.

Fig. 3.11 plots the percentage of successful measurements versus epicentral distance. In the teleseismic range, receiver distance has no significant influence on measurement success. Frequency band has a moderate influence: at the lowest frequencies, about 55% of attempted source-receiver pairs yield a good measurement, but only about 40% in the highest frequency band. By contrast, measurement success in the P-diffracted range drops precipitously as receiver distance increases. Frequency band is seen to have a relatively larger influence than for teleseismic P: measurement success is 2-3 times better in the lowest bands than in the high or microseismic noise bands. The much lower success with distance mirrors the exponential drop of Pdiff wave amplitude with distance in Fig. 3.2. Since the level of random noise in a recording is largely independent of epicentral distance, signal-to-noise ratio decreases as distance increases, and observed waveforms tend to become dominated by noise, no longer fitting the synthetics. This also explains the minimum of usable measurements in the microseismic band, where absolute noise levels exceed those in higher or lower frequency bands, so that signal-to-noise ratio drops below usable levels sooner as a function of distance.

Large earthquakes generate large wave amplitudes, and hence we expect a strong positive effect of earthquake magnitude on measurement success for Pdiff – stronger than for teleseismic P. Fig. 3.12 confirms this. Percentage of successful measurements is plotted against source magnitude, separately for

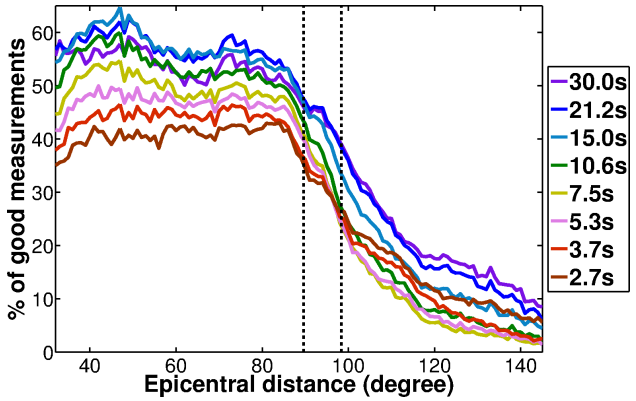

Figure 3.11: Percentage of successful dT measurements ($x_c \geq 0.8$), as a function of epicentral distance and frequency band. In the teleseismic P-range, measurement success depends more on the frequency band than on epicentral distance, and varies between 55 and 40% in the lowest and highest bands, respectively. In the P-diffracted range, measurement success rate drops sharply with increasing distance, mirroring the exponential drop in signal amplitudes of Fig. 3.2. Success rate is lowest in the secondary microseismic noise band (yellow and pink lines, consistent with Fig. 3.10).

receivers in the close (32°-60°) and far (60°-95°) teleseismic ranges, and in the close (95°-120°) and far (>120°) Pdiff ranges. The results for the two teleseismic groups are very similar: about 30-40% of source-receiver pairs yield successful measurements for the weakest events of M_w = 5.5 (percentage averaged over all frequency bands). Success rates decrease with event size, but level off at 60% for M_w = 6.5, and even drop again for the largest events (because their true source time functions are more complex than accommodated by our simple point source estimates).

The systematics are different for Pdiff: below magnitude $M_w < 6$, only a small fraction of measurements are successful, especially in the far teleseismic range. Measurement success increases strongly with event magnitude, again confirming that Pdiff measurements are limited mainly by signal-to-noise ratio. Magnitude 8 events produce remarkable success ratios of $> 35\%$ even in the far teleseismic range, which equals the success ratios for teleseismic P. In order to achieve $> 35\%$ good measurements, event magnitudes M_w must be approximately 5.5, 5.7, 6.5, and 8.0 for the near-P, far-P, near-Pdiff, and far-Pdiff ranges, respectively.

Fig. 3.13 shows histograms of measured traveltime anomalies dT in the P- versus Pdiff ranges, sorted by frequency band (colours). The dT are

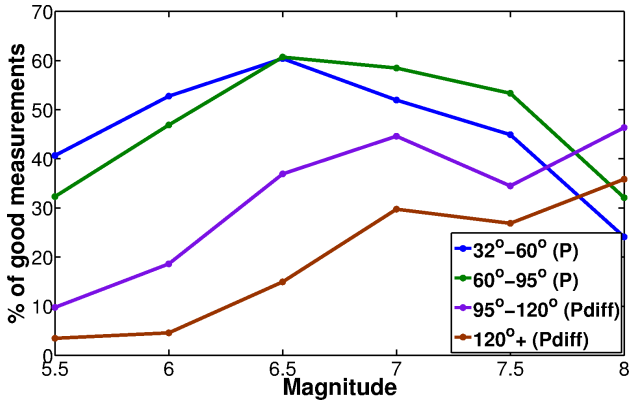

Figure 3.12: Percentage of successful dT measurements ($x_c \geq 0.8$), as a function of earthquake source magnitude M_w and epicentral distance range. In the core-diffracted range (red and purple lines), the rate of successful measurements grows with earthquake magnitude. In the teleseismic P range (green and blue), this is only true for small magnitudes ($M_w < 6.5$). For larger events the success rate drops again, because our point-source approximation becomes inadequate.

corrected for the earth's ellipticity, for station topography, and for crustal structure using crustal model CRUST2.0 (Bassin et al., 2000). Standard deviations range between 1.44 and 2.14 s for teleseismic dT (depending on frequency band), and between 1.92 and 3.94 s for P-diffracted dT. The relative differences between frequency bands and distance ranges are real, but the absolute dT values are conservative estimates because the mean of the dT has been removed eventwise. A non-zero mean could result from a misestimated origin time rather than from 3-D structural heterogeneity, the signal of interest. On the other hand, removing the mean may discard some signal that is truly due to earth structure, hence "conservative". The mean was not calculated on all measurements – this would yield decidedly non-Gaussian histograms because the mean would be skewed by a few spatially concentrated station clusters, mainly USArray. Instead, it was calculated on the rather evenly distributed Global Seismographic Network in the lowest frequency band, and subsequently removed from the dT values of all stations and all bands, yielding the largely Gaussian histograms of Fig. 3.13.

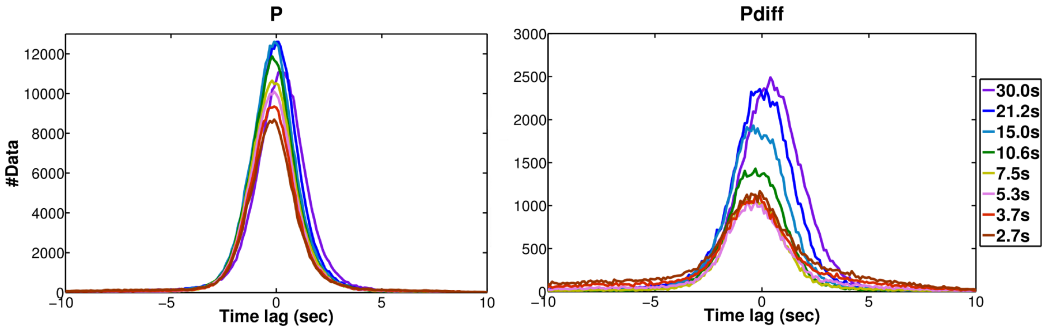

Figure 3.13: Histograms of multifrequency traveltime anomalies dT. The mean of dT was removed eventwise, and topographic, crustal and ellipticity corrections were applied. Only measurements that yielded $x_c \geq 0.8$ are included. Left: dT of teleseismic P waves. Their standard deviation σ_T ranges between 1.44 and 2.14 s, depending on frequency band. Right: dT of core-diffracted Pdiff waves, with σ_T ranging between 1.92 and 3.94 s.

3.3.2 Global mantle heterogeneity inferred from Pdiff traveltime anomalies

We turn to the structural information contained in our large, global set of P-diffracted traveltime data. Out of 418,226 candidate Pdiff source receiver-paths, 165,651 yielded at least one successful passband measurement. 3,345,808 attempts at measurements (418,226 paths times 8 frequency bands) yielded 479,559 multifrequency dT values of $x_c \geq 0.8$. The dTs are corrected for the effects of ellipticity, crust and station elevation.

Fig. 3.14 plots the coverage of the CMB by nominally core-grazing segments of 479,559 Pdiff paths that yielded successful measurements. Showing the Fresnel zones of finite-frequency kernels instead of rays would be a more faithful approximation of true measurement sensitivities near the CMB, but this major computational effort was not complete at the time of writing. The CMB was subdivided into blocks of 0.5°, that is, 720 x 720 blocks, and for each block, the lengths of all core-grazing segments visiting it are summed up, yielding a measure of how well each block is sampled. This is equivalent to plotting the cumulative column density (sum over each column) of an inversion matrix.

The lowermost mantle under the northern Pacific and East Asia are most densely sampled (dark red). The oceans of the southern hemisphere, especially the southern Atlantic, are the most poorly sampled. Overall, however, the lowermost mantle is better sampled under the oceans than under the

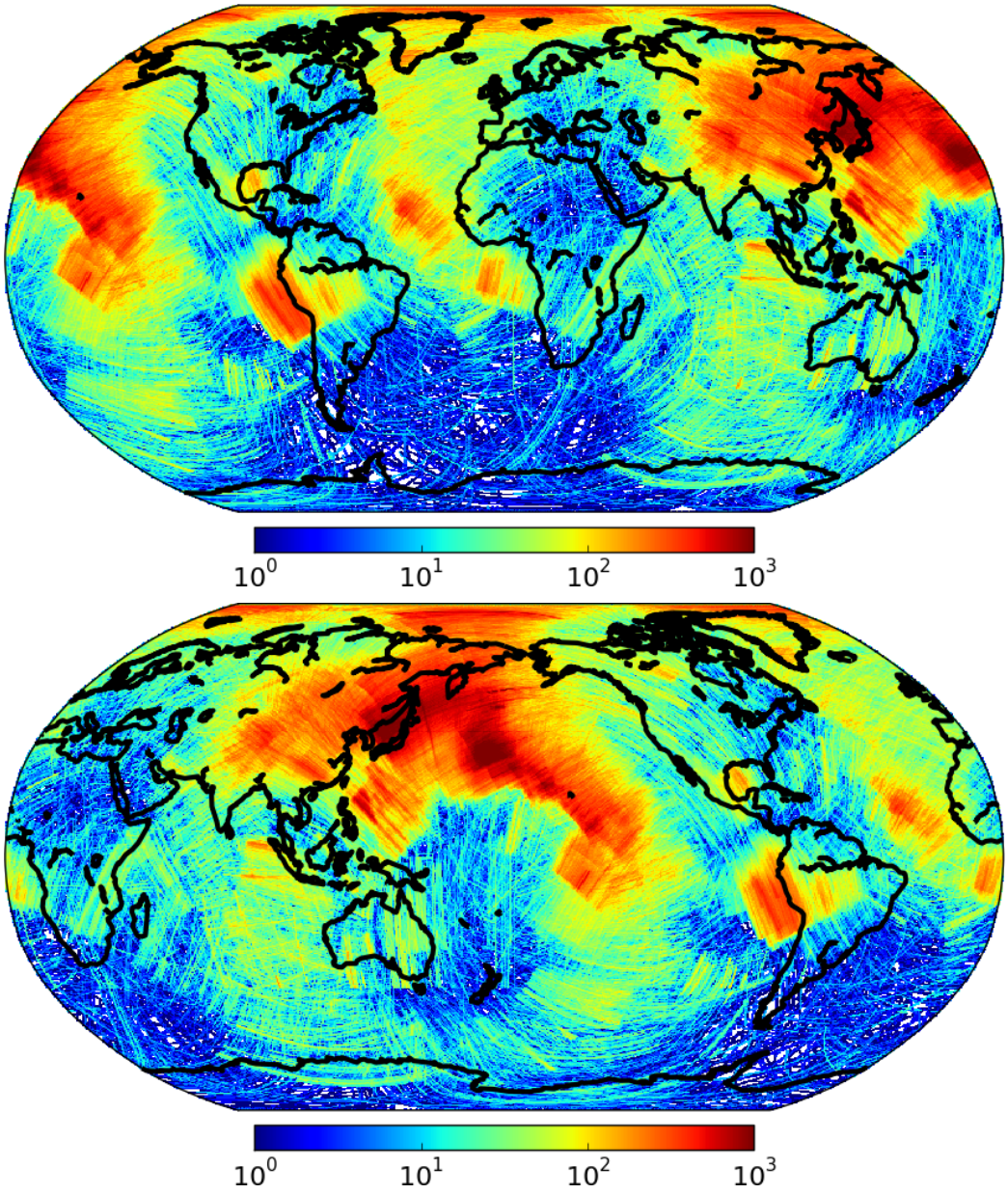

Figure 3.14: Sampling of the lowermost mantle by our data set of 479,559 Pdiff traveltime anomalies. The same data are shown in two different map views, Atlantic-centred at the top, Pacific-centred at the bottom. Each line represents the core-grazing segment of a ray-theoretical Pdiff path that yielded a successful measurement (i.e. $x_c \geq 0.8$ in any frequency band). Density of ray path coverage is indicated by colours (note that the colour scale is logarithmic). The CMB under oceans tends to be better sampled than under continents, especially in the southern hemisphere. The true sensitivity of a Pdiff wave to core-mantle boundary structure is ellipsoidal rather than ray-like – covering a broader area of the CMB and extending hundreds of kilometres into the overlying mantle.

continents. The heavy footprint of USArray appears as localised, red-yellow patches, with the clearest example located under South America and the adjacent Pacific (from paths that originate from seismicity in South Sandwich). Fig. 3.14 also permits to gauge the extent to which wave paths cross, an important proxy for tomographic resolution.

Fig. 3.15 shows the same ray coverage as Fig. 3.14, but projected on the CMB are traveltime anomalies dT, permitting to assess the spatial distribution of seismically fast and slow regions in the lowermost mantle. This rough "proto-tomography" exercise assumes that all arrival delays or advances originate from the core-grazing path segments. Each ray segment is coloured by the relative traveltime delay incurred w.r.t. the reference velocity model IASP91 and the Q values of PREM. Red paths are seismically slow, blue paths are fast. Anomalies are seen to be on the order of 1%.

Large-scale structures emerge that are well-known from global tomography models, such as generally slow regions beneath the southern hemisphere, corresponding to the African and Pacific Large Low Shear Velocity Provinces (LLSVPs). Seismically fast areas are confirmed under most of eastern Asia and under Central America, presumably the resting places of massive accumulations of subducted lithosphere. A striking east-west velocity gradient is evident across the USArray-sampled patch beneath South America and adjacent Pacific (compare to Fig. 3.14). Other strong velocity gradients appear to rim the Pacific LLSVP.

3.4 Discussion

For waveform measurements on Pdiff waves, the main challenge is their signal-to-noise ratio. Wave amplitudes that rapidly decline with epicentral distance and with frequency (Figs 3.2 and 3.11) meet with ambient noise levels that peak in the microseismic frequency band. Our approach mitigates by attempting measurements in 8 different passbands across the broad-band range of 30.0-2.7 s period, maximising the chance that at least one measurement will succeed, so that the wave path is basically covered. Fitting a passband waveform is easier than a broad-band measurement, since the latter depends on good SNR across all frequencies. This is particularly pertinent in selectively high-noise environments, as for Pdiff waves or on the ocean floor (where signal is not weak *per se*, but microseismic noise is elevated compared to land stations).

Over all eight bands and all distances, 14.3% (479,559) high-quality, multifrequency Pdiff measurements were achieved, compared to 47.0% (2,306,755) teleseismic P measurements. Diffracted P wave measurements are most likely

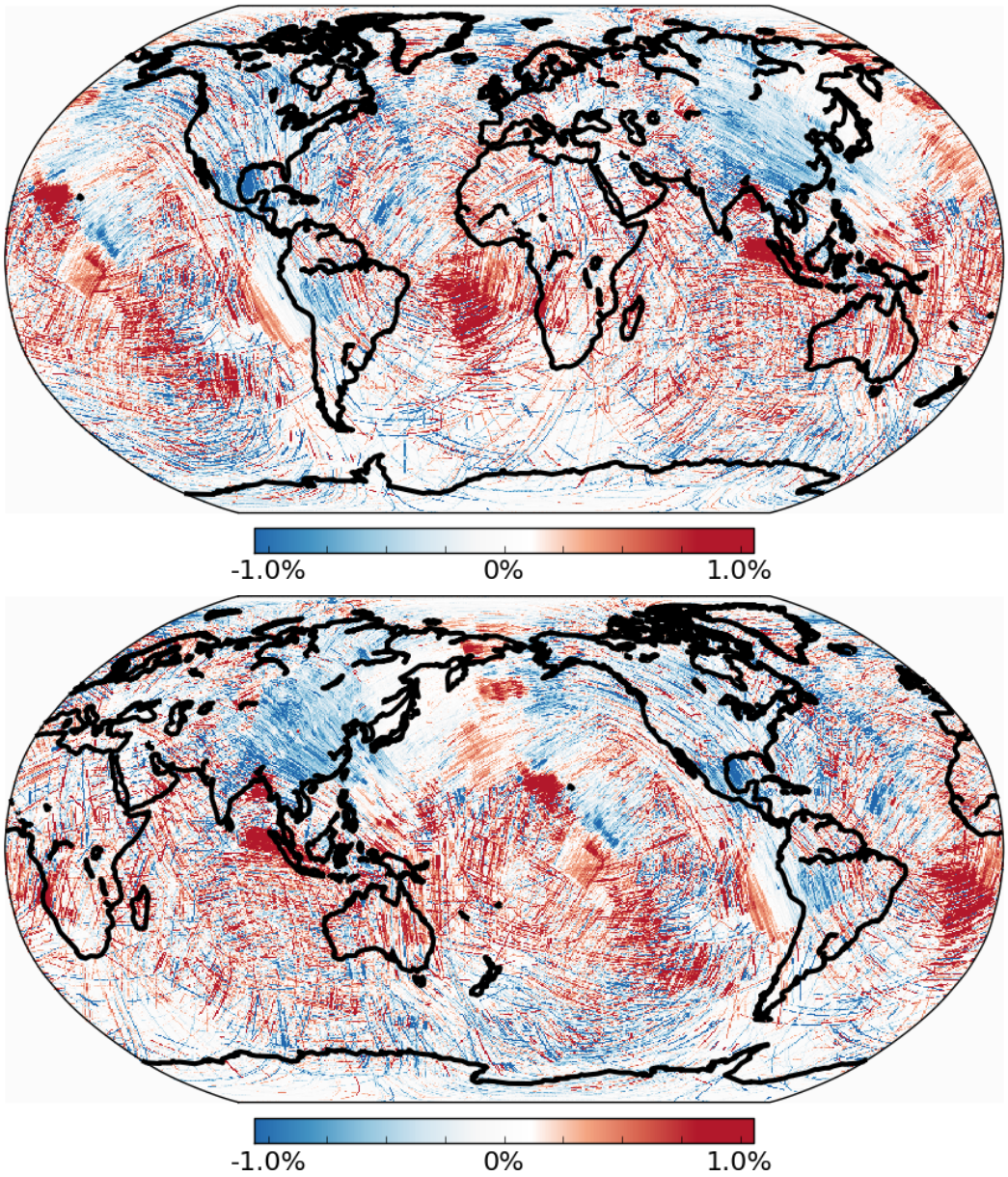

Figure 3.15: Traveltime anomalies of 479,559 Pdiff waves, projected onto their CMB-grazing segments. As Fig. 3.14, except that colour represents the traveltime anomaly dT in %. Red designates a measurement delayed relative to IASP91, blue means advanced. For a given delay dT, a longer core-grazing segment would result in a fainter shade of red, because dT is spread evenly along the segment. The raw dT measurements were corrected for earth's ellipticity, station topography and near-station crustal structure. Assuming that most Pdiff traveltime anomalies originate in the lowermost mantle, this plot represents a rough "proto-tomography", charting out seismically fast (blue) and slow (red) structural anomalies near the CMB.

to succeed in the lowest frequency band of 30.0 period (21.5% success rate) and least likely in the 7.5 s period band of the microseismic noise (9.0%). Successful teleseismic P measurements are most likely at 21.2 s (53.8%) and least likely in the highest band of 2.7 s (38.8%).

For a given wave path, the frequency dispersion between dT at the low and high ends of our frequency range can be 1-2 s, although more of this seems to be due to a mismatch of the spherically symmetric reference model rather than to 3-D heterogeneity (Fig. 3.6). Nevertheless, the signature of 3-D mantle heterogeneity is clearly present in Figs 3.6 and 3.7. A substantial part of this signal seems to originate from the lowermost mantle, since dT dispersion is significantly stronger for Pdiff than for P.

Computing Green's functions and sensitivity kernels up to the high frequencies used here is challenging and currently only feasible in a spherically symmetric reference model. This limitation may not be a serious one, given that mantle heterogeneity is expected to be of only a few percent, except perhaps in Ultra-Low Velocity Zones (ULVZs), which are however very limited spatially. Hence, a single-iteration matrix inversion, starting from a spherically symmetric reference model, should be capable of yielding a very good approximation to true earth structure. We hope and expect that our ability to exploit the highly resolving short wavelengths will far outweigh the limitation of not being able to iteratively update the solution.

The *Yspec* and *AxiSEM* software packages tools are both capable of delivering accurate Green's functions in spherically symmetric reference models, for the ambitious, broad-band frequency range in this study. Since *AxiSEM* was not complete at the time of creating our synthetic archive, *Yspec* was used to calculate all the traces in ≈ 2000 events of our data set which cost $\approx 10^6$ CPU hours in total.

Recently, we adapted the work flow to incorporate the *Instaseis* database approach of van Driel et al. (2015). Instaseis takes advantage of reciprocity of the Green's function; therefore, one database can be built for all possible sources with only two runs of AxiSEM: one for the vertical and one for the horizontal components. This expends a large upfront effort on computing and storing generic global Green's functions componentwise. Extraction from the database and linear combination into specific Green's functions then become quasi-instantaneous (on the order of milliseconds).

Fig. 3.16 compares the computational cost of different methods in computing synthetic seismograms down to 2 s period, assuming that each event was recorded at 1000 three-component stations. Ignoring the cost of computing the database (shaded green in Fig. 3.16), Instaseis is comparable in performance to WKBJ (red line). In contrast to WKBJ, where each crustal reverberation has to be defined separately, Instaseis synthetics automatically

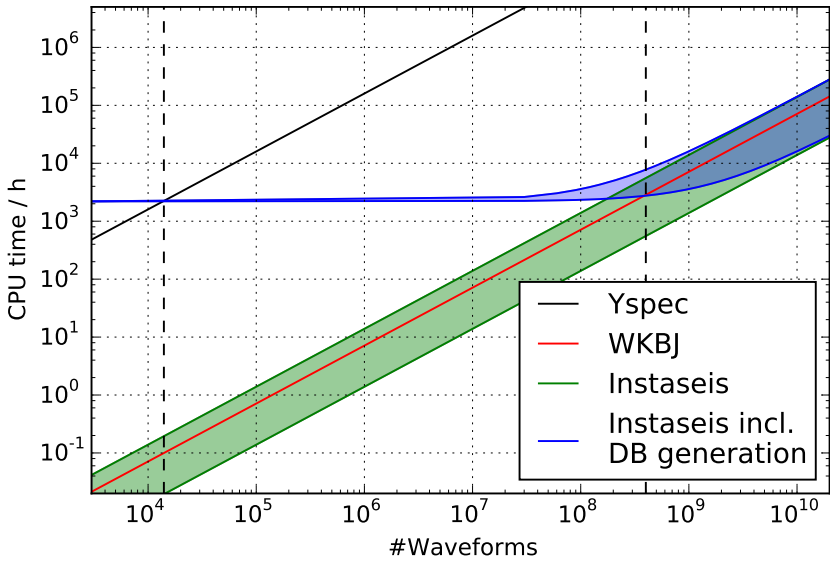

Figure 3.16: Computational cost of different methods in computing synthetic seismograms for finite-frequency tomography, up to 2 s period. For Yspec, we assume that each event is recorded by 1000 receivers with 3 components. The shaded regions for Instaseis indicate the dependence of the performance on the actual source receiver distribution (van Driel et al., 2015). Including the cost to generate the database with AxiSEM (shaded light blue), Instaseis breaks with Yspec for 14,000 waveforms, which is equivalent to about 5 sources in this configuration.

account for the full crustal response. Also, it accurately models all seismic phases, including diffracted waves (e.g., Pdiff) and triplicated phases from upper mantle discontinuities (Fig. 3.17). If we include the cost of generating the database (shaded light blue in Fig. 3.16), Instaseis breaks in computational cost with Yspec already at about 14,000 waveforms, that is, five events with 1000 three-component stations each. Moreover, generating seismograms with different source locations or moment-tensor radiation patterns, which is often necessary in tomography, does not require a new database.

Sensitivity kernels from full forward and backward wavefields will also be computed with *AxiSEM*, since *Yspec* is not an efficient tool for this purpose.

Deconvolution of source parameters is the bottleneck that requires the most user supervision, and no earthquake centre currently does this work. Stähler and Sigloch (2014) demonstrated a scheme of probabilistic inference that should largely automate this step. It also delivers full source uncertainty estimates and propagates them into the (correlated) uncertainties of

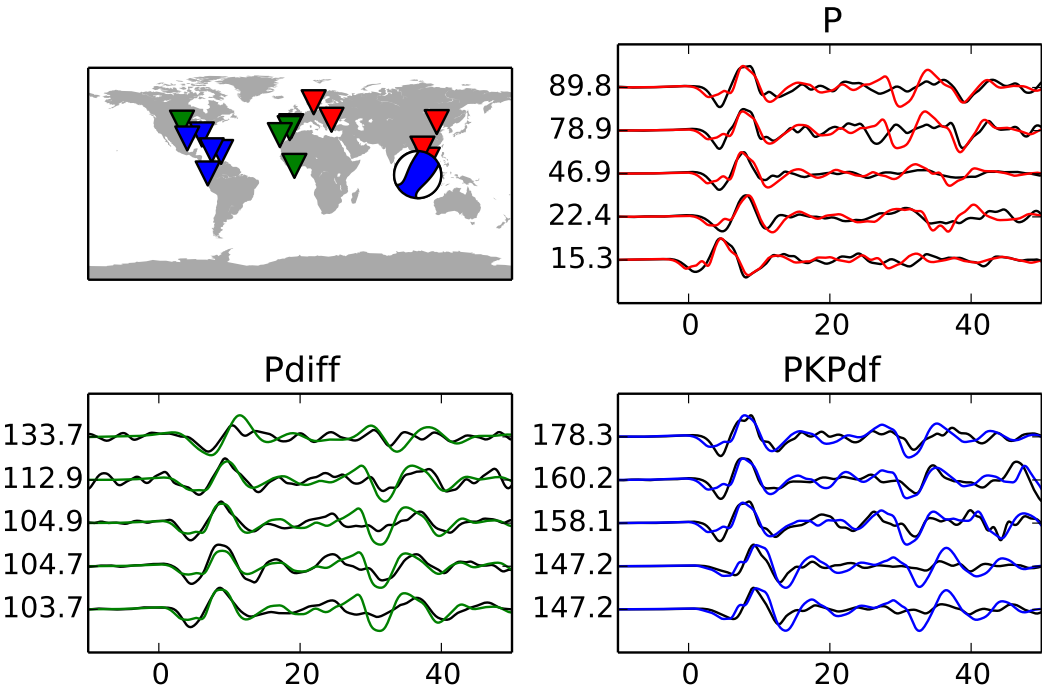

Figure 3.17: Comparison between observed seismograms (black) and Instaseis synthetics for the Sumatra event of Fig. 3.1. Vertical axis labels are epicentral distances, horizontal axis is time relative to the ray-theoretical arrivals. A Gabor filter with 3.7 s central period is applied to all traces, and the synthetics are convolved with the source time function estimate of Fig. 3.1d. The waveforms are aligned by computing relative time-shifts between data and synthetic seismograms using cross-correlation (similar to actual finite-frequency tomography).

dT measurements, as required to properly fill the measurement covariance matrix for tomography.

In terms of structural heterogeneity at long spatial wavelengths, the results of Fig. 3.15 are encouragingly consistent with prior studies that used different methods and data. This includes the aforementioned LLSVPs and the slab graveyards under Eastern Asia and Central America, which have become robust features in global tomographic models, especially S-wave models, such as S362ANI (Kustowski et al., 2008), S40RTS (Ritsema et al., 2011), SAW24B16 (Mégnin and Romanowicz, 2000), HMSL-S (Houser et al., 2008), or GyPSuM (Simmons et al., 2010). Because P wave models do not have the benefit of including normal modes, their resolution of lowermost mantle structure is generally considered less reliable and more attenuated. While too

early to assess the improvements possible through Pdiff in this regard, the large number of successful Pdiff measurements and their general agreement with known structure is promising.

Since the pioneering studies of Wysession (1996a) and Kàrason and Van der Hilst (2001), Pdiff waves have not been explicitly included in global P wave tomographies. Both studies used a data set of 543 PKPdf - Pdiff differential traveltimes. By comparison, we obtained 479,559 usable Pdiff waveform measurements, demonstrating the sea change in data availability that has taken place. While our structural findings bear more overall resemblance to recent global S-wave models, they are also broadly consistent with these two early, global Pdiff inversions, which recovered the two LLSVPs as well as high-velocity anomalies beneath south/central America and eastern Asia. Not present in our dT map is a high velocity structure under south and southeast of Africa that was apparently required by their Pdiff data in both the Wysession (1996a) and the Kàrason and Van der Hilst (2001) study.

From Pdiff measurements made by Ritsema and van Heijst (2002), Koelemeijer et al. (2013) constructed a traveltime map similar to our Fig. 3.15, by projecting the entire dT anomalies onto the CMB. With a coarse gridding of 5° caps, only large-scale structure was targeted. They recovered the two LLSVPs and high-velocity anomalies under central America and east Asia – another confirmation of these most robust features in the lowermost mantle.

A relatively small-scale but pronounced feature of Fig. 3.15 is an intensely slow patch just west of Hawaii. This structure was recently described as a newly recognised ULVZ by Cottaar and Romanowicz (2012), who modelled Sdiff waveforms. It appears to be highly visible to P waves as well.

3.5 Conclusion

We presented a method to routinely measure and model core-diffracted P waves across the broad-band frequency range. Green's functions are calculated by semi-analytical (i.e. theoretically exact) wave propagation through a spherically symmetric reference model, to 1 Hz dominant frequency, and broad-band source time functions are deconvolved from the waveform data. Largely automated processing of 1857 events yielded 2,306,755 teleseismic P- and 479,559 P-diffracted traveltime measurements by cross-correlation across eight frequency bands (dominant periods 30-2.7 s).

While significantly more challenging than teleseismic P-measurements, we obtain very decent success rates for dT measurements on Pdiff waveforms, of around 14% across all attempted wave paths and frequencies. The main challenge is signal-to-noise ratio, which drops precipitously with epicentral

distance and with frequency, as expected for diffracted waves. dT anomalies are larger for Pdiff than for P waves, and frequency dependence of dT due to 3-D heterogeneity is stronger for Pdiff as well. Projected on their core-grazing ray segments, the dT measurements recover major structural, lower-mantle heterogeneities known from existing global mantle models based on P- and S-waves. This methodically novel and very large data set of core-diffracted P waves is ready for global waveform tomography.

4

Global multiple-frequency inversion of teleseismic and core-diffracted P waves

Abstract

We present a new global seismic tomography model of isotropic P wave velocity anomalies at all mantle depths. This broad-band waveform inversion seamlessly incorporates a very large set of core-diffracted P-phase measurements (Pdiff) alongside conventional teleseismic P and PP waveforms. Pdiff waves extensively sample the lower third of the mantle and the Core-Mantle Boundary (CMB). Hence, their inclusion in a technically rigorous manner vastly improves the spatial resolution of the deepest mantle. Pdiff measurements combined with P and PP cover a wide range of mantle depths suitable for whole mantle tomography. In this study, all phases are measured and modelled from 30 s dominant period to the highest frequencies that produce satisfactory fits ($\approx 3\ s$). We use 1,550,587 multifrequency P, 577,106 PP and 391,320 Pdiff traveltime observations in the actual inversion. The measurements are linked to the model-parameters (3-D velocity structure) with Born scattering kernels which are capable of modelling dispersion in multifrequency traveltime observations. The model is parameterised adaptively by tetrahedra; edge-lengths are adjusted locally based on the expected resolution with a spa-

tial resolution of ≈ 60 km in highly sampled regions. The matrix inversion is done by an iterative conjugate gradient method, and both norm damping and smoothing are employed for regularisation. Here, we focus on the framework for joint inversion of multifrequency measurements and a set of short period traveltime anomalies, and we briefly discuss first-order features of our "preferred" global P wave tomography model. The mapped features confirm several previously imaged structures in the mantle. At the same time, sharper outlines for several subduction systems (e.g., Tethyan, Aegean and Farallon slabs) appear in our model. We trace some of these features throughout the mantle to investigate their morphological characteristics in a large (whole-mantle) context. Moreover, we report the structural findings revealed by our model, such as extensive fast-velocity provinces in the lowermost mantle representing (presumably) ancient subducted slab accumulations under East Asia and Central America, subdivisions of Large Low Shear Velocity Provinces at the root of the mantle, an Ultra-Low Velocity Zone west of Hawaii, and detailed lateral heterogeneities under Europe and North America.

4.1 Introduction

Since the advent of seismic tomography, the internal structure of Earth has been vastly sampled and imaged at different scales: from regional to global scales with a variety of spatial resolutions as a function of latitude, longitude or depth. Tomography models create one of the key inputs for geophysical interpretation from paleogeographic studies to geoid and mantle dynamics. Due to the growth of seismological waveform data holdings at data centres and development of novel inversion techniques, the resolution of the tomography models (in all scales) has been increasing. A support for this is the emerging consistency in the imaged structures with different data sets and techniques (especially) on large scales. Although, discrepancies still exist in various wavelength structures between models which emphasise the need for high-quality models to better understand the geological and geodynamical processes driving the earth.

Global tomography models of compressional wave velocity variations have been obtained from different types of data and modelling techniques. The classical method is based on arrival times of P as inputs modelled by ray (infinite frequency or zero wavelength) approximation due to its simplicity and computational efficiency (Dziewonski et al., 1977; Zhou, 1996; Grand

et al., 1997; van der Hilst et al., 1997; Obayashi and Fukao, 1997; Kennett et al., 1998; Bijwaard et al., 1998; Boschi and Dziewonski, 2000; Kàrason and Van der Hilst, 2001; Zhao, 2004; Lei and Zhao, 2006; Li et al., 2008; Koelemeijer et al., 2016).

A new class of tomography method was developed based on Born scattering kernels (Marquering et al., 1998; Dahlen et al., 2000; Hung et al., 2000; Montelli et al., 2004b) to model the frequency-dependent interaction of waves with structural heterogeneities (i.e. scattering of energy) which ray-based methods are unable to accommodate. The method is particularly advantageous for imaging mantle plumes, which are difficult to probe because of their narrow diameters (only on the order of the sampling wavelengths) and because they are located deep beneath ocean basins (far from sources and receivers). Both factors contribute to wavefront healing through the scattering of energy which removes an effect of the structure on traveltimes. Waveform-based methods of tomography are able to explicitly account for wavefront healing, and the required broad-band seismograms and processing techniques have become more and more abundant. Montelli et al. (2004b); Hung et al. (2004); Yang et al. (2006); French and Romanowicz (2015) are among the recent plume surveys.

For lack of dedicated measurements, early studies (Montelli et al., 2004b) had to retrospectively assign some finite-frequency content, at the low end of the body-wave spectrum ($\approx 20\ s$), to pre-existing traveltime data sets. However, Montelli et al. (2004b) demonstrated that the solution of full-fledged global tomography problems by considering physically realistic sensitivity kernels is computationally feasible.

Sigloch and Nolet (2006) developed a method to measure finite-frequency body-wave amplitudes and traveltimes in its entire frequency content, from 30.0 down to 2 sec (with lower measurement uncertainties). This method can generate the kind of data that finite-frequency modelling was envisioned for, consistent with the derivation of the kernels and their theoretical definition (Dahlen et al., 2000; Dahlen and Baig, 2002). It systematically exploits all frequency bands that the broad-band measurements can offer with the flexibility to identify and include only those of high signal quality. By applying this method to North America, a large multifrequency data set was created, and it was shown that finite-frequency tomography is clearly superior to ray theory in imaging the lower mantle. The tomography results showed highly resolved structures in that region (Sigloch et al., 2008; Sigloch and Mihalynuk, 2013) with a number of newly discovered fragments of the Farallon plate.

Hosseini and Sigloch (2015) applied the measurement technique of Sigloch and Nolet (2006) to a global data set and measured multifrequency travel-

times of P and Pdiff across their entire spectrum, up to the highest occurring frequencies. This was achieved by measuring the frequency-dependent traveltime observations using cross-correlation in eight overlapping frequency passbands with dominant periods between 30.0-2.7s. To account for the diffraction and non-ray-like behaviour of core-diffracted waves, Green's functions were calculated by semi-analytical (i.e. theoretically exact) wave propagation through a spherically symmetric reference model, to 1 Hz dominant frequency. The Green's functions were convolved with broad-band source time functions inverted from the waveform data to generate the synthetic waveforms comparable with the observed data. We find that in real data, P traveltime anomalies typically vary by 0.1-0.3 sec in different frequency bands (for a given source-receiver pair), and they are stronger for Pdiff. This Frequency dispersion in body-wave measurements constitutes the information that finite-frequency modelling is capable of exploiting above and beyond ray theory.

This study puts its emphasis on the methodology for joint inversion of the multifrequency cross-correlation measurements (Hosseini and Sigloch, 2015) and a set of short period traveltime anomalies to image the earth's mantle down to the CMB. We used finite-frequency modelling in which the matrix A of the (linearized) problem $d = Am$, as in traditional ray-theoretical inversions, is computed explicitly. The data vector d contains multifrequency measurements obtained by cross-correlating the observed data with synthetic waveforms in eight overlapping frequency bands, from $\approx$ 2000 processed earthquake sources in our data set. The Green's function for each source-receiver pair was computed by simulating wave propagation in a broad-band spectrum from 0.2mHz to 1Hz in the spherically symmetric earth model IASP91 (Kennett and Engdahl, 1991) extended with density and attenuation from PREM (Dziewonski and Anderson, 1981). A subset of short period P and PP data from ISC was included to d to enhance the coverage. The traveltime anomalies (d vector) put constraints on 3-D elastic structure V_p; which are modelled by traveltime kernels K. We used three-dimensional frequency-dependent sensitivity kernels K for each source-receiver pair and each dominant period. Vector m contains the parameters to estimate, i.e. 3-D anomalies in elastic V_p as discretised on the three-dimensional adaptive (and irregular) global grid. These are the three components (d, A and m) that will be discussed in details here.

After a brief overview on multifrequency traveltime observations (d vector) in Section 4.3, the methods to generate the inversion grid and to calculate the sensitivity kernels are discussed (Section 4.4). In Section 4.5, we show models (three-dimensional P wave speed variations) resulting from inverting the global traveltime data set. This requires a selection of regularisation

parameters that will be discussed in Section 4.5.1. Finally, we present a "preferred" model and discuss only first-order features deferring the detailed analysis to a later paper.

4.2 Linear inversion

We assume that the traveltime observations $d_i (i = 1, ..., D)$ are linearly linked to the earth model $m(r)$ by the traveltime kernels K in the following explicit linear form:

$$d_i = \int_V K_i^T(r) m(r) d^3r \tag{4.1}$$

where $K_i^T(r)$ is the sensitivity kernel of ith data (Section 4.4.1), and the integral is over the whole earth's volume V. In practice, the volume is limited to the region where the amplitude of the sensitivity kernel $K_i^T(r)$ is significant. This equation is in continuous form (∞-unknowns) and first it should be discretised into a finite number of unknowns through model parameterisation or generation of the inversion grid (Section 4.4.2). Inversion grid linearly interpolates the continuous kernels onto the discrete nodes of the mesh; therefore, the unknown function $m(r)$ can be written as a linear combination of M known "basis functions" (h_j):

$$m(r) = \sum_{j=1}^{M} m_j h_j(r) \tag{4.2}$$

where $m_j (j = 1, ..., M)$ are the finite-number of unknowns in the inversion. By substituting eq. 4.2 into 4.1:

$$d_i = \sum_{j=1}^{M} A_{ij} m_j, \tag{4.3}$$

in which:

$$A_{ij} = \int_V K_i^T(r) h_j(r) d^3r \tag{4.4}$$

Each row of $A_{ij} (i, j = 1, ..., M)$ links one measurement d_i to all the model parameters m_j according to the projected sensitivity kernel K_i onto the inversion grid. A_{ij} is calculated and assembled for all the measurements before the inversion (Section 4.4.1) by using the Fréchet kernel expressions derived by Dahlen et al. (2000).

The above equation can be rewritten in matrix form for all the measurements as:

$$d = Am \tag{4.5}$$

This equation does not have a unique solution ($m = A^{-1}d$) due to uneven distribution of source-receiver pairs, data inconsistency and rank deficiency in A. One method to deal with rank-deficiency and ill-conditioning is by applying regularisation to the linearized eq. 4.5 which results in *regularised least-squares* formula. Two usual regularisation techniques are damping and smoothing. In the former, the model parameters are pushed toward zero, i.e. the preferred model should be close to a reasonable a priori background model; this decreases the effect of noise during the inversion. On the other hand, in smoothing, the roughness (second derivative) of the neighbouring model parameters are minimised. Both damping and smoothing are a priori information, i.e. they have not been inferred from the experiment or seismic measurements.
In practice, using smoothing alone can result in non-trivial null-spaces; therefore, we use a combination of smoothing and damping operators to regularise the problem. This can be written in a matrix form as:

$$\begin{pmatrix} C_d^{-1/2}d \\ 0 \\ 0 \end{pmatrix} = \begin{pmatrix} C_d^{-1/2}A \\ \epsilon_n I \\ \epsilon c_m^{-1/2} \end{pmatrix} m \tag{4.6}$$

in which C_d is the data co-variance matrix (Section 4.3), ϵ_n is (global) damping parameter, $c_m^{-1/2}$ acts as smoothing operator and ϵ is a scaling factor that can be used to tweak the intensity of smoothing operator.

ϵ_n in eq. 4.6 scales uniformly the intensity of norm damping on all the model parameters. To generalise this, a parameter scaling matrix L is inserted:

$$\begin{pmatrix} C_d^{-1/2}d \\ 0 \\ 0 \end{pmatrix} = \begin{pmatrix} C_d^{-1/2}A \\ \epsilon_n LI \\ \epsilon c_m^{-1/2} \end{pmatrix} m \tag{4.7}$$

L is a diagonal matrix whose elements vary as a function of data coverage at each model parameter: highly sampled model parameters take values around 1 and poorly sampled parameters have > 1 factors. In other words, a priori information (damping) with higher amplitude is assumed for regions with lower data coverage.

In the following sections, each component (d, A and m) in our global inversion will be discussed.

4.3 Data Space (d vector)

The d vector in eq. 4.7 contains the traveltime measurements scaled by their assigned uncertainties C_d. The data co-variance matrix (C_d) is used to make the data univariant and it is assumed to be diagonal with σ_i^2 (standard errors) as entries.

Two kinds of traveltime observations were included in the d vector: multifrequency cross-correlation traveltimes and short-period "picked" arrival times. Fig. 4.1 shows the distribution of sources and receivers from both data sets that were used in the actual inversion (after removing all the outliers). The two data sets will be discussed separately in the following sections.

Multifrequency cross-correlation traveltimes

A global data set of 1857 earthquake sources of magnitude $m_b \geqslant 5.8$ that occurred between 1999 and 2010—plus many earlier or smaller events if they occurred in less common locations were used for multifrequency measurements. The source parameters (moment tensor and depth) as well as broadband source time functions were deconvolved from the data for all the events. Out of this data set, P, PP and Pdiff were measured since the combination of these seismic phases covers a wide range of epicentral distances and mantle depths suitable for whole mantle tomography (Fig. 4.2). P and PP traveltime observations were our main data source for the upper and mid mantle. On the other hand, Pdiff waves graze the core and, therefore, sample the deepest part of the mantle extensively, making it possible to image the velocity structures down to the CMB.

We follow the measurement technique described in Sigloch and Nolet (2006) and Hosseini and Sigloch (2015). Multifrequency traveltimes of P (32-85 degrees), PP (64-155 degrees) and Pdiff in all available epicentral distances (typically 98-160) were measured by cross-correlating the waveform data with synthetic seismograms in frequency passbands ranging from 30.0 to 2.7 s dominant period. Each synthetic seismogram is the convolution of the source time function estimate with the Green's function calculated by semi-analytical wave propagation through a spherically symmetric reference model, to 1 Hz dominant frequency (refer to Hosseini and Sigloch (2015) for more details). Only those measurements were considered for the inversion that passed the acceptance threshold: Cross-Correlation (CC) factor more than 0.8 for P and Pdiff, and $CC \geqslant 0.85$ for PP, regardless of the frequency band. Standard errors were assigned to each measurement according to its CC ranging from $\approx 0.2\ s$ for high-quality measurements to $\approx 1\ s$ for low CC.

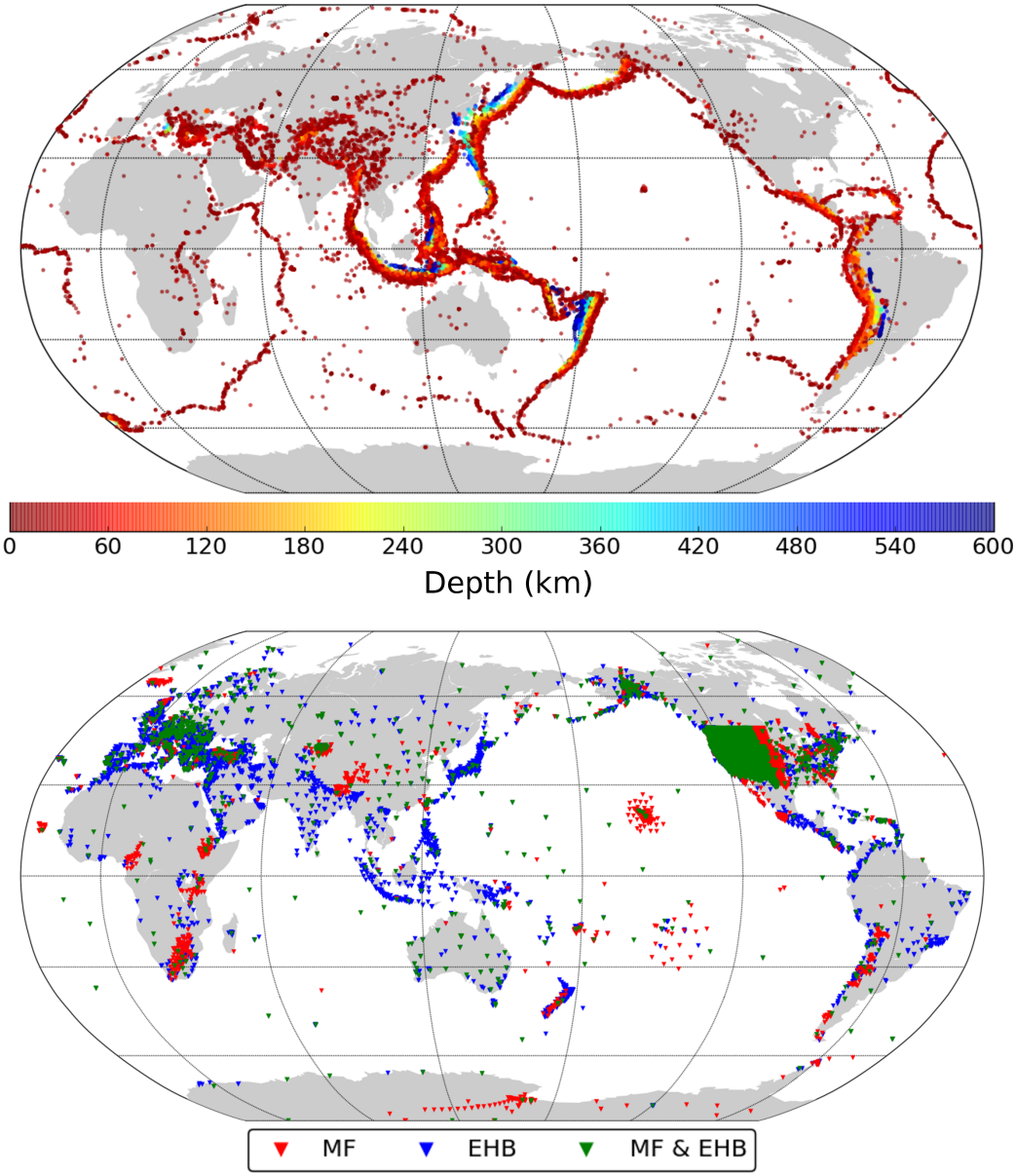

Figure 4.1: Global distribution of earthquake sources and receivers used in the tomography. Abbreviations: MF: Multifrequency; EHB: EHB catalogue. Each source and receiver contributed to at least one successful measurement in either one frequency band (multifrequency measurement) or one short period picked arrival time (EHB bulletin). Source and receiver coverage in this map reflects our 'No data left behind' philosophy (Hosseini-zad et al., 2012), in that the aim is to extract a maximum of information from all available data. Top: seismicity map of 31,187 sources. The colour bar shows the depths of the events (the deepest events are in the foreground). Bottom: the traveltime observations of 10,638 station locations used in the actual inversion. Red triangles show the stations that had, at least, one good multifrequency measurement. Blue triangles are for EHB stations, and greens are the stations that had, at least, one good multifrequency measurement and one short period picked arrival time from EHB bulletin.

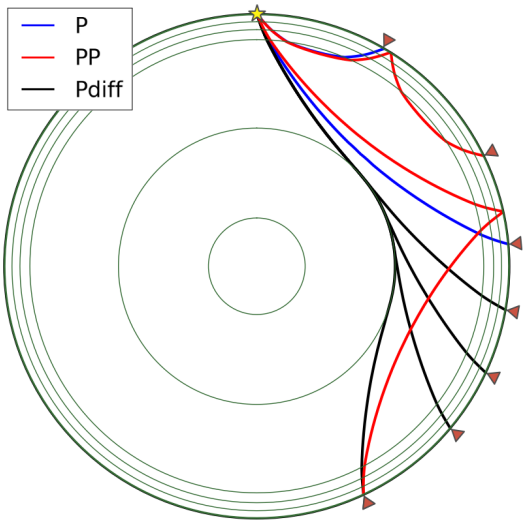

Figure 4.2: Combination of P, PP and Pdiff covers a wide range of epicentral distances and mantle depths suitable for whole mantle tomography. In this study, we use P (32-85 degrees), PP (64-155 degrees) and Pdiff in all available epicentral distances (typically 98-160). Blue: teleseismic P wave; red: PP; black: Pdiff.

The measurement errors were used to fill in the data covariance matrix C_d in eq. 4.7.

Table 4.1 lists the number of records, epicentral distance range and the frequency content of the multi-frequency traveltime measurements of P, PP and Pdiff.

Short period picked arrival times

In addition to the multifrequency measurements, a subset of short period arrival times from EHB (Engdahl et al., 1998), a catalogue of routinely picked and processed arrival times, was selected and included in the d vector. EHB data is obtained from reprocessing of picked arrival times reported to ISC (International Seismological Centre) and NEIC (National Earthquake Information Center) using the Engdahl et al. (1998) algorithm, including iterative relocating of earthquake sources and dynamic phase re-identification. The inclusion of picked arrival times from the EHB catalogue can greatly enhance the coverage in locations where the information content of the multifrequency measurements was poor. However, the EHB bulletin contains data for $\approx$ 150,000 events with millions of measurements for different seismic phases. To reduce this, we only select those source-receiver pairs that match:

Phase	Number of records	Epicentral Distance	Frequency
P	1,550,587	32-85	0.03-0.37 Hz
PP	577,106	64-155	0.03-0.37 Hz
Pdiff	391,320	98-160	0.03-0.37 Hz
Total	2,519,013		

Table 4.1: List of seismic phases measured with the multifrequency cross-correlation technique of Sigloch and Nolet (2006) and Hosseini and Sigloch (2015). P (32-85 degrees), PP (64-155 degrees) and Pdiff (typically 98-160) were measured in frequency passbands ranging from 30.0 to 2.7 s dominant period. The total number of multifrequency measurements that were used in the actual inversion (after removing the outliers) is specified for each seismic phase.

1. Event magnitude $\geqslant 5.0$.

2. P and PP with epicentral distance 32-85 and 64-170, respectively.

3. Arrival time reading precision < 0.1 s.

4. Quasi-homogeneous directional coverage at source/receiver locations.

The quasi-homogeneous directional coverage was achieved by employing the following steps: first, the earth surface was divided into blocks of 5 °. For each block that enclosed, at least, one source or one receiver, the number of rays and their directions were stored. When the number of rays from one direction (0-90, 90-180, 180-270 and 270-360 degrees bins) reached to a threshold, no more rays would be accepted for that direction and that block. However, a good azimuthal coverage for each event is desirable as source location is one of our inversion parameters; therefore, for each event, stations from different azimuths were selected and included in the d vector. The final product is shown in Fig. 4.3.

Table 4.2 lists the number of records and epicentral distance range of the seismic phases that were selected from EHB catalogue.

4.3.1 Common Corrections

Synthetic seismograms are calculated on the spherically symmetric earth model of IASP91 in which neither effects of the crust nor ellipticity and topography are incorporated (only a layer with constant thickness and velocity

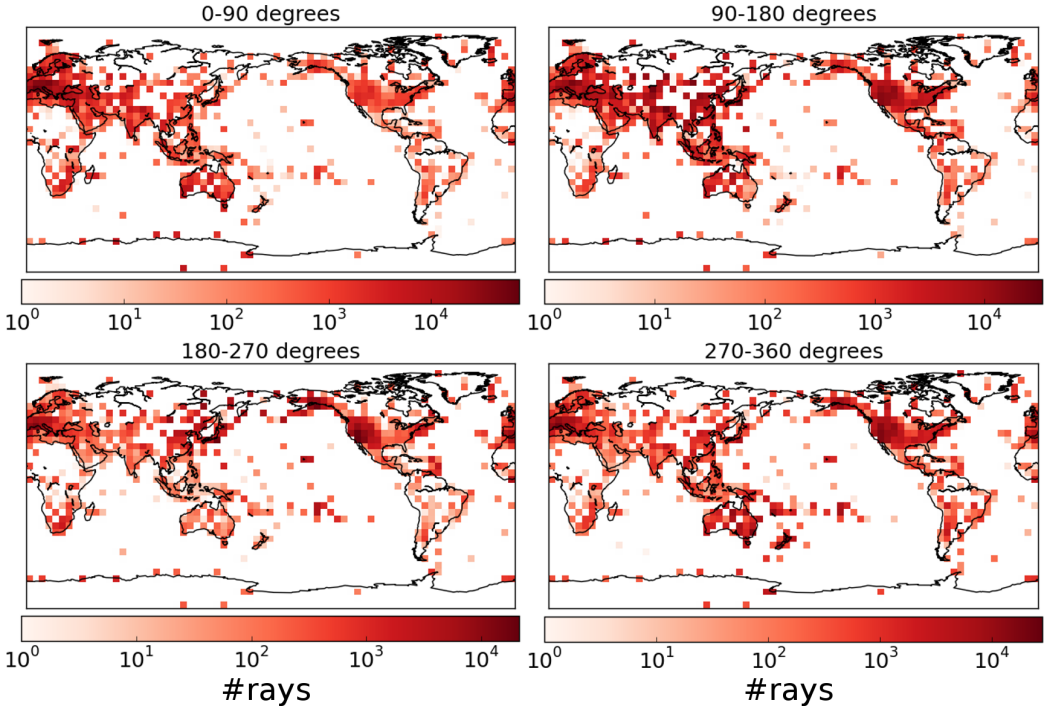

Figure 4.3: Quasi-homogeneous directional coverage at source/receiver locations. Short period arrival times were selected from EHB catalogue and added to the d vector of eq. 4.7 to enhance the coverage in locations where the source-receiver coverage of our multifrequency measurements was poor. One of the criteria for selecting the high-frequency arrival times was quasi-homogeneous directional coverage at source/receiver locations. To achieve this, the earth surface was divided into blocks of 5 °, and the number of rays and their directions (0-90, 90-180, 180-270, 270-360 degrees bins) at each block that enclosed, at least, one source or one receiver were stored. Once the number of rays in one direction bin reached to a threshold, no more rays would be accepted from that direction in that block. This figure shows the density of each block (source/receiver locations) for different directional bins.

Phase	Number of records	Epicentral Distance	Frequency
P	3,285,227	32-85	1 Hz
PP	78,937	64-170	1 Hz
Total	3,364,164	1 Hz	

Table 4.2: High frequency picked arrival times of P and PP were selected from EHB catalogue and added to d vector to enhance the coverage of multifrequency measurements. The total number of picked arrival times for P (32-85 degrees) and PP (64-170 degrees) that were used in the actual inversion (after removing the outliers) is listed here. Due to the large number of available picks in EHB catalogue, only a subset of arrival times was selected and added to the d vector. See text for further discussion on selection criteria.

is considered as a crust). To account for the known deviations from spherically symmetric earth model and to bring the predicted time closer to that of a 3-D Earth, corrections should be applied to the computed traveltimes:

$$dt = (T_{\text{obs}} - T_{\text{pred}}) - dt_{\text{cor}} \tag{4.8}$$

where $(T_{\text{obs}} - T_{\text{pred}})$ is the measured traveltime anomaly (Section 4.3) and dt_{cor} is the correction term. In case of crustal correction:

$$\delta T_{\text{cru}} = -t_{\text{BG}} + t_{\text{3D}} \tag{4.9}$$

t_{BG} is calculated according to the incident angle and the length of the ray in the crustal layer of IASP91, and t_{3D} is computed on $2^\circ \times 2^\circ$ crustal model CRUST2.0 (Bassin et al., 2000). Crustal correction is crucial in global tomography as it weakens the crustal smearing (and imaging artefacts) into the upper mantle. Fig. 4.4 shows the crustal correction for Pdiff as an example.

To consolidate the ellipticity effects, the earth is approximated by an ellipsoid. In case of Pdiff, ellipticity correction is calculated based on the parts of the ray that goes downward and upward to/from CMB (Kennett and Gudmundsson, 1996; Nolet, 2008).

These corrections were applied to the traveltime observations (multifrequency cross-correlation measurements and short period picked arrival times) using the method described in Tian et al. (2007a) and the corrected measurements were added to the d vector of eq. 4.7.

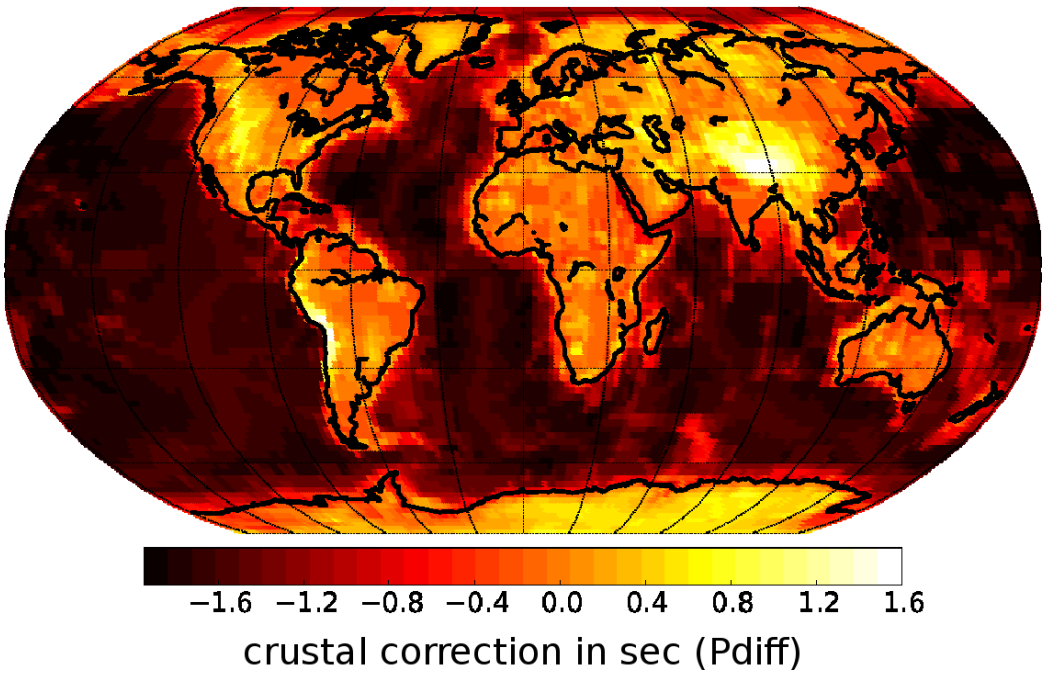

Figure 4.4: Map of crustal correction for Pdiff waves based on CRUST2.0. Pdiff has a constant incident angle at the background model surface; thus, it is possible to plot the corrections for all the locations on one map. In case of P and PP, the crustal corrections depend on the incident angle.

4.4 Data kernel (A matrix)

A matrix in eq. 4.7 links the accepted traveltime observations (d vector) to the discretised model parameters (m vector). Each row in the A matrix contains the projected 3-D sensitivity kernel values of one measurement on the inversion grid. As we have two sets of traveltime observations (Section 4.3), two groups of sensitivity kernels are also calculated: frequency-dependent and ray-based kernels. In the following two sections, the computation of kernels and the generation of the inversion grid are briefly explained.

4.4.1 Computation of kernels

Traveltime observations (δT) are linked to velocity anomalies ($\delta ln(V_p)$) by the sensitivity kernels (K^T):

$$\delta T = \int K^T(r)\delta ln(V_p)d^3r \tag{4.10}$$

The kernels of multifrequency cross-correlation traveltimes of our data set were computed with the approach of Dahlen et al. (2000) in which a method based on paraxial approximation is introduced for efficient calculation of 3-D sensitivity kernels (Hung et al., 2000; Montelli et al., 2004a; Tian et al., 2007b). These frequency-dependent kernels were computed for the bandpass filters (Gabor filters in eight overlapping frequency bands) used for traveltime measurements. Fig. 4.5 shows the sensitivity kernels of P, PP and Pdiff. Pdiff kernels are approximated, as Dahlen's method (Dahlen et al., 2000) cannot account for diffraction.

The elastodynamic wave equation can be approximated for high-frequencies with ray theory (hypothetically infinite frequency). The short-period picked arrival times selected from EHB bulletin fall in this group with the centre frequency of $\approx$ 1 Hz. The sensitivity kernels for these traveltime observations are the projected geometrical ray path on the inversion grid as they are shown in Fig. 4.6 for two examples.

4.4.2 Parameterisation

Spatial distribution of interpolation supports in the discretised model directly controls the maximum resolution retrievable in different regions of the earth. There is also a compromise between the desire to render fine features and computational cost in designing the inversion mesh. Irregular tetrahedral meshes have the advantage of being able to accommodate different sizes of tetrahedra in a straightforward manner. The mesh can thus be rendered

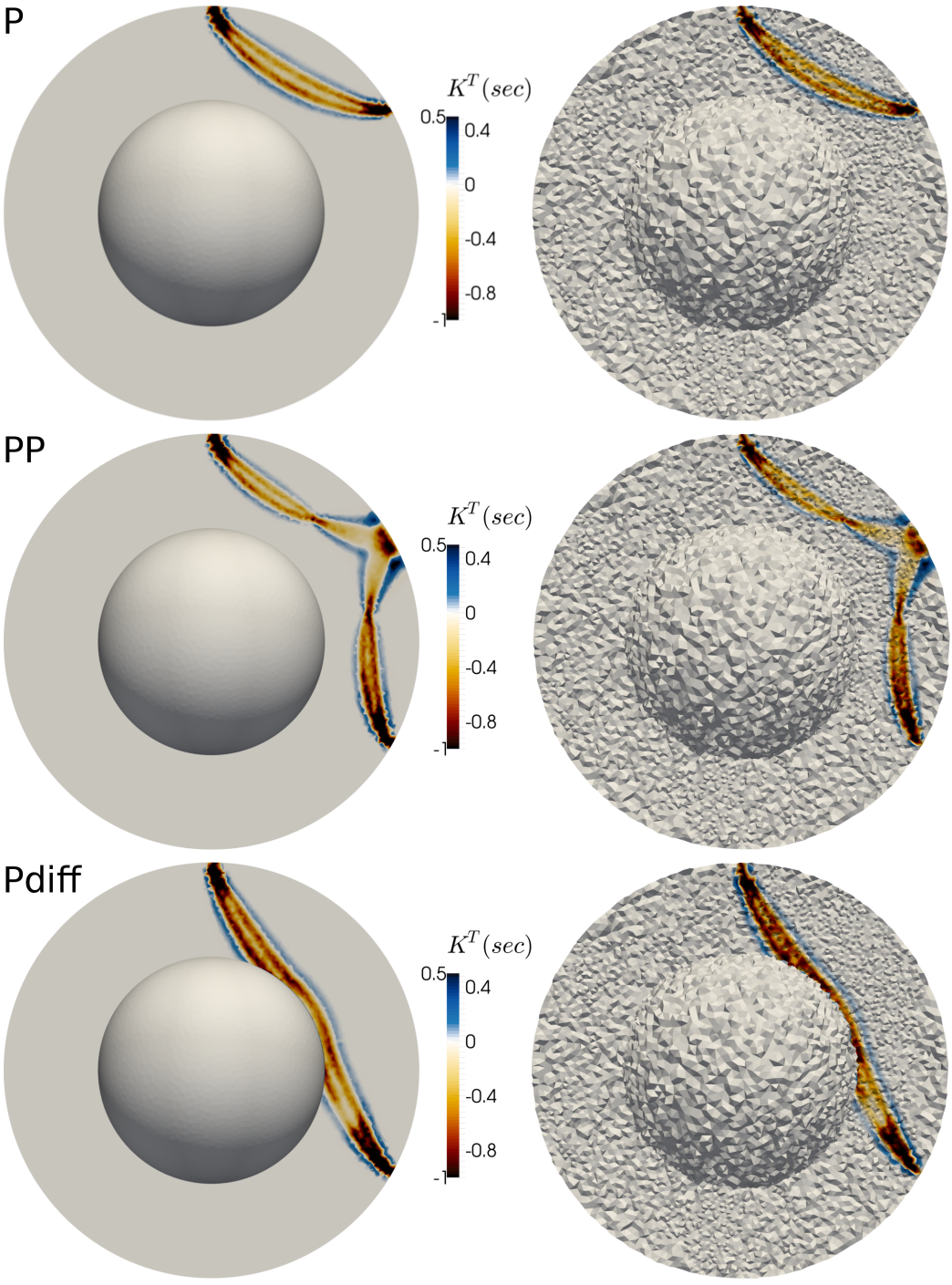

Figure 4.5: 3-D sensitivity kernels of P, PP and Pdiff seismic phases calculated with the method of Dahlen et al. (2000). These kernels are frequency-dependent; here, only kernels for a Gabor filter with 21.2 sec central period are plotted. As diffracted waves cannot be calculated with this method, we approximated the kernels for Pdiff measurements. Moreover, the paraxial approximation is not valid near antipodal epicentral distances (Tian et al., 2007b); therefore, PP kernels with epicentral distance ≤ 155 were calculated.

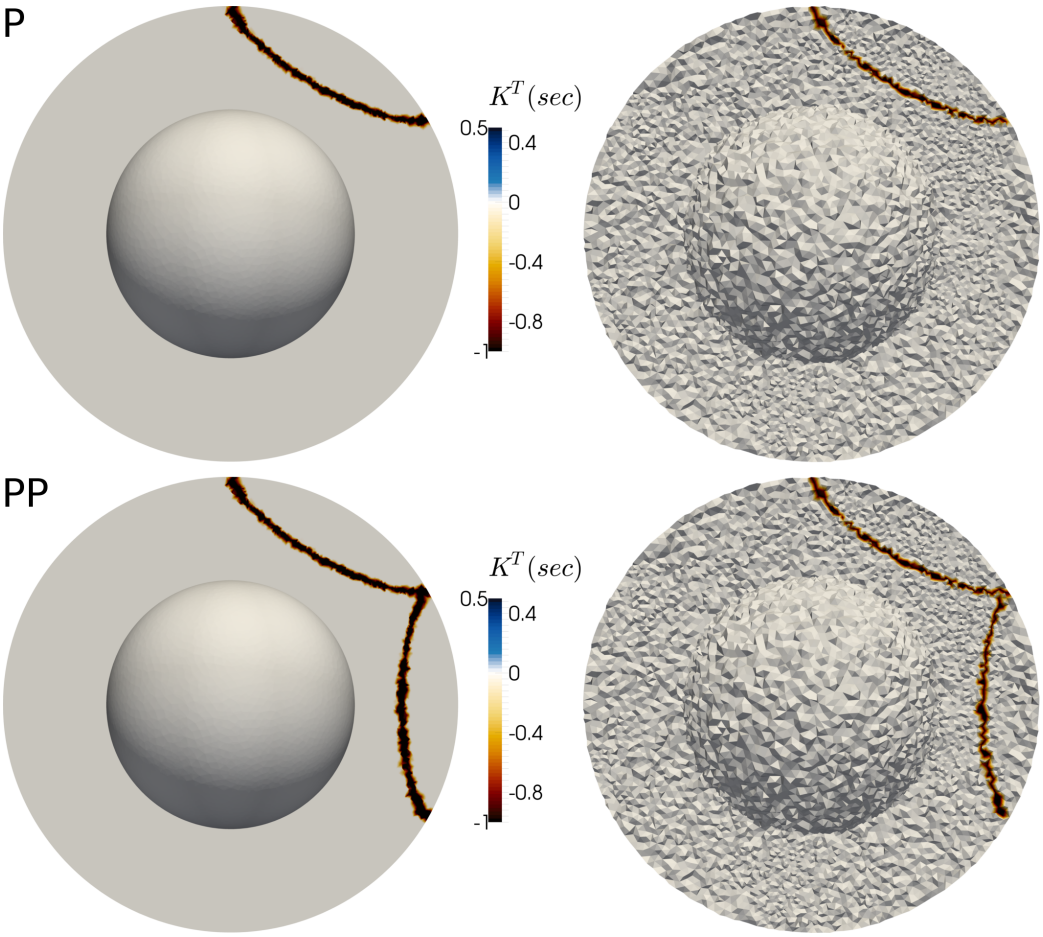

Figure 4.6: Sensitivity kernels of P and PP picked arrival times from EHB catalogue. The modelling of the high-frequency arrival times is based on ray-theory (infinite frequency) which results in the projection of geometrical ray paths on the inversion grid.

denser selectively in places where the data offers increased resolving power (e.g., dense data coverage). Here, we use tetrahedra to discretise the earth model with linear interpolation between the four vertices using barycentric coordinates. This should be sufficient since tomography equations are in integral form, and they are insensitive to small detail in the function describing the model (Nolet and Montelli, 2005).

Generation of non-overlapping tetrahedra was done using the *DistMesh* tool (Persson and Strang, 2004) and based on Delaunay criteria using the *QHULL* tool (Barber et al., 1996). *DistMesh* generates tetrahedral meshes of high quality as measured by the regularity of the tetrahedra: a large ratio of volume to facet length cubed is desired. To ensure that the tetrahedra that contain the hull nodes always enclose the Earth's surface, the radius of the convex hull is set to 6371+50 km. Due to the local interpolation scheme selected for discretisation, it is possible to locally change the interpolation node density. To this end, a method was developed to generate spherical tetrahedral meshes with adaptive cell sizing based on the kernel coverage:

As the first step, a homogeneous inversion grid with 200 km edge-length tetrahedra was generated, and the sensitivity kernels of a relatively large subset of the data were calculated. The absolute values of the kernels were then projected and summed at each node. This is similar to a column sum plot of the A matrix. In the next step, a new inversion grid was generated in which the number of interpolation supports was increased for the regions with large sensitivity kernel values (up to 66 km edge-length), and the number of nodes was decreased around the model parameters with low data coverage, by assigning the desired edge-length to each node of the grid according to its sensitivity kernel value. After some iterations, all measurements were used, and the final inversion grid with 396,501 nodes was generated.

Fig. 4.7 compares the results of the first and final steps. In the former, the inversion grid is homogeneous, but the sensitivity kernel values are highly inhomogeneous. As an example, the sensitivity kernel values are very high beneath North America and low in East Pacific. Moreover, the values take a striped pattern as a function of depth in this case (Fig. 4.8). This is due to the homogeneity of the inversion grid in which there are more interpolation supports at specific depths. By adapting the inversion grid, the distribution of the sensitivity kernel values become more homogeneous, for example, the values beneath North America decreases, and the kernel values of poorly sampled regions (e.g., East Pacific) increase. Additionally, the striped pattern of the Fig. 4.8 in homogeneous inversion grid vanishes since the nodes are distributed throughout the globe.

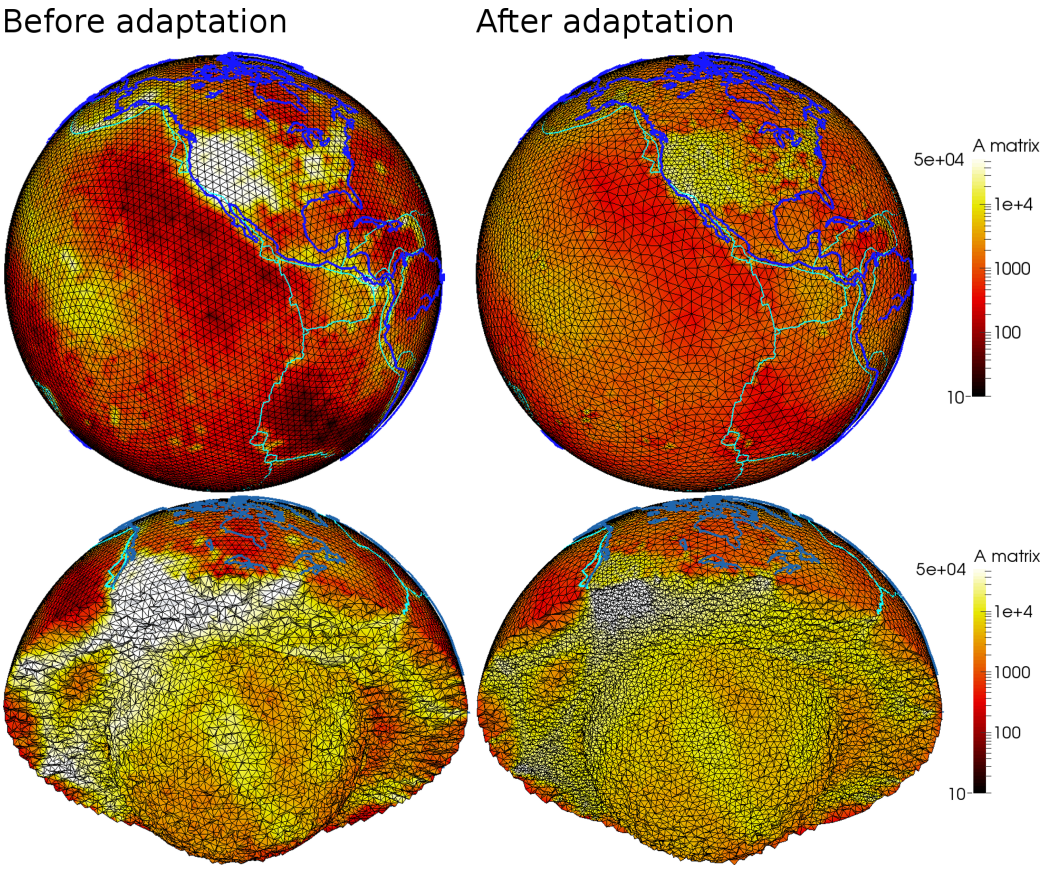

Figure 4.7: Adaptive parameterisation of the domain according to the sensitivity kernel values at each node. This method optimises the spatial distribution of the interpolation supports based on the sensitivity kernel coverage of the data set, that is, generates more interpolation supports around the locations with higher absolute sensitivity kernel values. As the first step, a homogeneous grid was generated, and the sensitivity kernels of a large subset of data were calculated and projected on the grid (left panels). In this case, the amplitudes of sensitivity kernels differ greatly in different regions. By having the absolute kernel values at nodes of the grid and assigning the desired edge-length to each, a new inversion grid with adapted edge-lengths was generated (right panels). In this case, the kernel amplitudes become more homogeneous. These two figures are not directly comparable in terms of the absolute kernel values since more measurements were considered in the final inversion grid compared to the initial grid. However, the increased homogeneity of the amplitudes is apparent in the adapted inversion grid. Note that the colour bar is logarithmic.

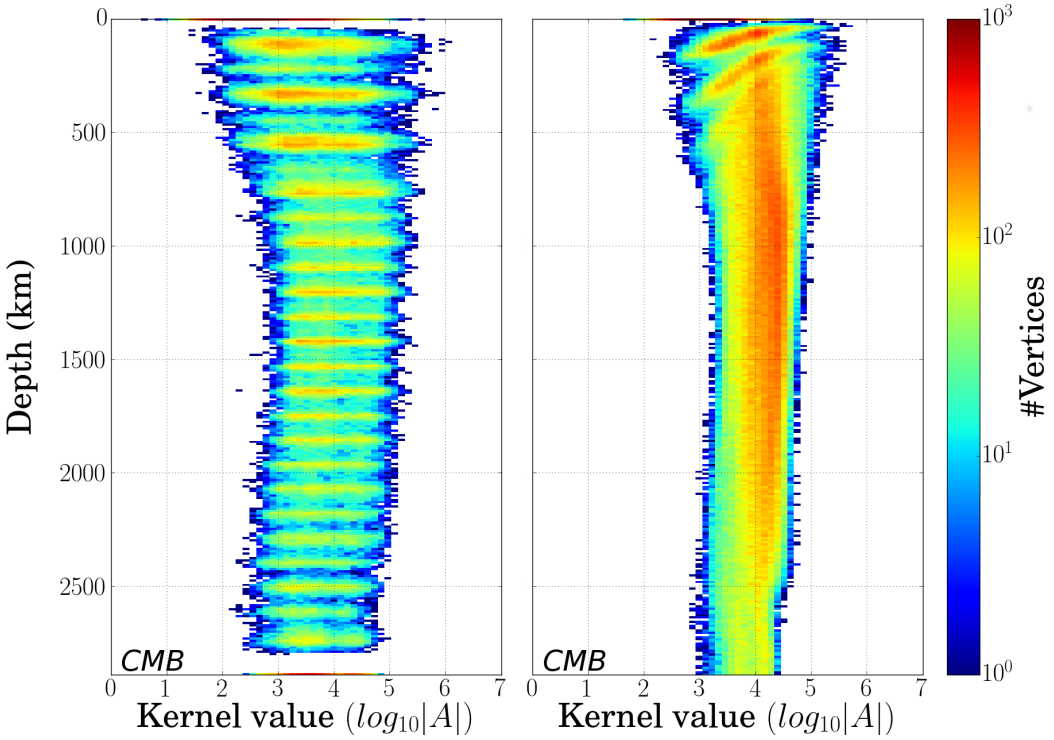

Figure 4.8: Sensitivity kernel values at each node of the inversion grid as a function of depth. In the initial grid (left panel), kernel values have a banded pattern which mirrors the homogeneity in the spatial distribution of the interpolation supports. By adapting the grid based on the kernel values, the striped pattern was replaced by a relatively uniform pattern in all depths. The colour bar shows the node density at each depth and absolute kernel value.

4.4.3 Global kernel coverage

A traveltime measurement constrains the average structure between a source and receiver. The geometry of the resolved average structure depends on the wave path (selected seismic phase) and the frequency content of the propagating wave, for example, sensitivity kernels of different seismic phases of this study in Figs 4.5 and 4.6. By increasing the number of measurements, the ability to resolve finer structures increases. Although the geometry of the source and receiver pairs is an important factor (i.e. crossing rays), the amplitude of absolute sensitivity kernel values at each model parameter can be to some extent representative of our ability in resolving the structural features. Figs 4.9 and 4.10 show this at several depth slices and for two sets of measurements: all the measurements used in the inversion (left panels) and all without core-diffracted (Pdiff) measurements (right panels). In both cases, high absolute kernel values appear beneath source and receiver locations at shallow depths (150 and 600 km). Moreover, the northern hemisphere generally has a better coverage. In the mid mantle (1050 and 1500 km), the coverage becomes more homogeneous in both cases with the lowest values under the southern Pacific, southwest of Indian ocean and south of Atlantic.

The global kernel coverage of two data sets starts to diverge for the lower third of the mantle (2000-2800 km). This is due to the inclusion of core-diffracted measurements (Fig. 4.10, left panels). Core-diffracted waves are abundantly observed but have hardly been used in seismic tomography. To our knowledge, the only global P wave tomographies that explicitly model and include Pdiff traveltime data were by Wysession (1996a); Kàrason and Van der Hilst (2001) both using a set of 543 differential Pdiff-PKP measurements. As a result, tomography resolution of the lower third of the mantle is expected to be much poorer than for the middle (teleseismic) third. In this study, 391,320 frequency-dependent Pdiff traveltime measurements were used to enhance the resolution in this region.

4.5 Model Space (m vector)

In Sections 4.3 and 4.4, d vector (traveltime measurements) and A matrix (sensitivity kernels) for adaptively discretised model parameters were constructed. Here, solution(s) to the inverse problem (vector m) formulated in eq. 4.7 will be discussed.

Entries of m are the three-dimensional solutions for isotropic compressional P wave with additional unknowns to account for source effects (hypocen-

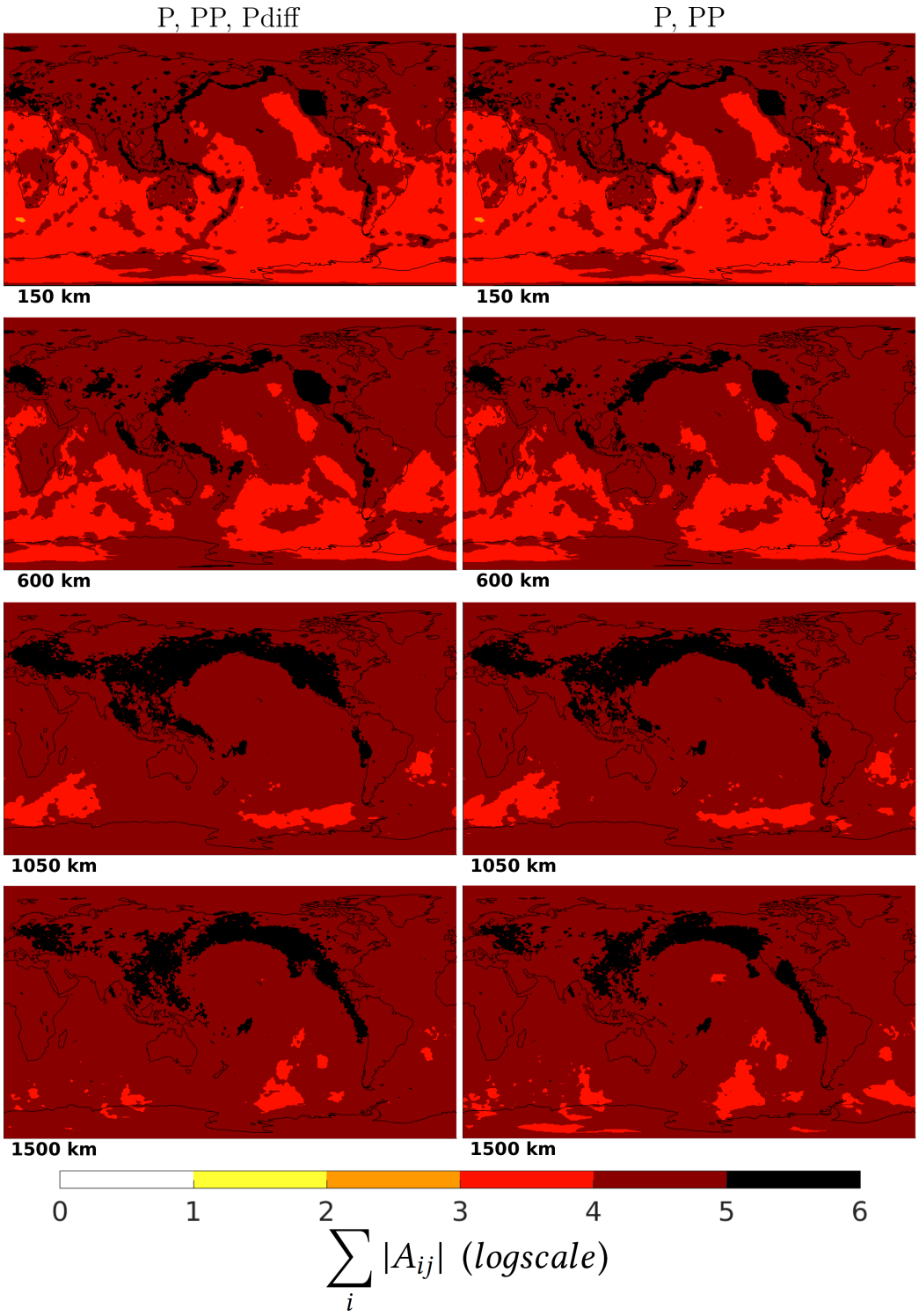

Figure 4.9: Absolute sensitivity kernel values (column sum of A matrix in eq. 4.7: $\sum_i |A_{ij}|$) for sections at four different depths (150, 600, 1050 and 1500 km). Left panels are for all measurements (P, PP and Pdiff) and right panels for P and PP (excluding Pdiff). At shallower depths, high kernel values appear mainly beneath the source and receiver locations. The distribution becomes more homogeneous in the middle third of the mantle (1050 and 1500 km). Note that the colour scale is logarithmic.

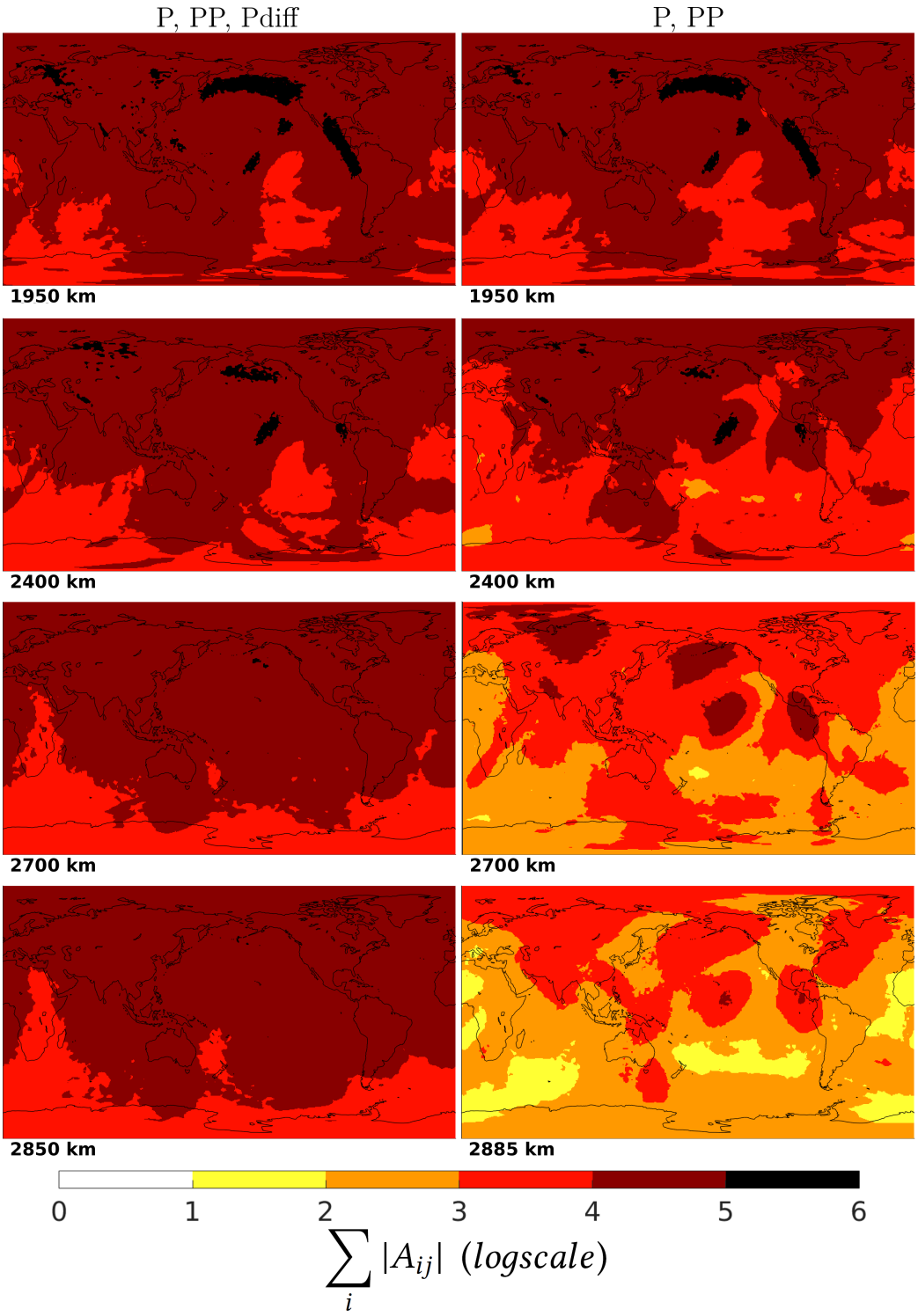

Figure 4.10: Same as Fig. 4.9 but for sections at 1950, 2400, 2700 and 2850 km depths. The difference between left panels (P, PP and Pdiff) and right panels (P and PP) becomes more apparent in the lower third of the mantle. This is due to the inclusion of core-diffracted P measurements which were the main data source for illuminating the lower third of the mantle in our inversion. Note that the colour scale is logarithmic.

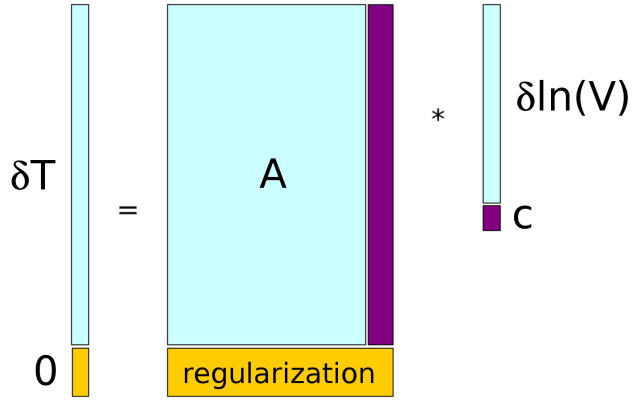

Figure 4.11: Schematic of the linear system of equations ($d_r = Gm$) whose L_2 norm needs to be minimised: $min||Gm - d_r||_2^2$. Data vector d_r consists of traveltime anomalies (δT) with 5,883,177 elements and appended rows for regularisation, thus subscript r for added rows to d. Model vector m consists of P wave velocity anomalies ($\delta ln(V)$) with 396,501 entries and appended event correction rows c (hypocenter and source origin time corrections). Matrix G links data and model parameters through traveltime kernels (A) and regularisation rows (refer to Section 4.5.1 for more details). Note that compare to eq. 4.7, event correction columns and rows are appended to A and m, respectively.

ter and origin time corrections). For every component (solution and correction) in the m vector, a prior uncertainty was assigned as follow: 2% for P wave velocity, 20 km for hypocenter corrections and 2.5 sec for event origin time corrections. Fig. 4.11 schematically shows the components of the system of equations to solve: $d_r = Gm$ in which d_r and G are d and A with appended rows for regularisation, respectively.

The G matrix contains $\approx$ 7M rows and $\approx$ 600K columns with $\approx$ 25,500M non-zero elements. Among different types of solvers to compute the inverse of a matrix, iterative solvers are the most suitable and efficient tools for an inverse problem with this size. Here, the inversion was done by minimising the L_2 norm with iterative conjugate gradient solver LSQR (Paige and Saunders, 1982; Nolet, 1985).

4.5.1 Selection of the preferred model

The linear inverse problem of eq. 4.7 is ill-posed and non-unique. One way of solving this system of equations is by inserting the regularisation param-

eters: damping and smoothing. We apply norm damping (minimising the amplitude of the model parameters) and Laplacian smoothing (minimising the roughness between adjacent parameters) to the system of equations. By changing the intensity of regularisation parameters, the trade-off between the residual data misfit in terms of reduced chi-squared (absolute chi-squared divided by the number of data N):

$$\chi^2 = \frac{1}{N} \sum_{i=1}^{N} \frac{(d_i^{obs} - d_i^{pred})^2}{\sigma_i^2} \tag{4.11}$$

and the model norm $|m|^2$ (squared Euclidean norm) can be analysed. Fig. 4.12 shows an example of this trade-off (L-curve); two cross sections at 1200 and 2885 km depth through the tomography models obtained by constant ratio $\frac{damping}{smoothing} = 0.1$ but with different amplitudes of damping and smoothing parameters are plotted. By increasing the intensity of regularisation, models show lower norms $|m|^2$ and higher χ^2. In these over-regularised models, many small-scale features are damped out; however, the amplitudes of robust structures decrease only gently.

Changes in the amplitude due to regularisation can affect the interpretation of tomography models. As an example, conversion of velocity structure to temperature field, one of the inputs for geodynamical modellings, are directly influenced by the amplitudes of anomalies. To better characterise these effects, Fig. 4.13 compares the mean of absolute amplitudes in 3 selected tomography models of Fig. 4.12. The amplitudes of the least regularised solution ($\chi^2 = 1.096$) are higher than the other models in all depths, and by increasing the intensity of regularisation, the amplitudes can be changed up to a factor of two at some depths (Fig. 4.13, right panel). Although these values cannot be generalised to all tomography models, they show the magnitudes to which the models are affected by the regularisation in a realistic example.

Selection of smoothing and damping parameters is normally done by assuming that the models close to the bending of the L-curve are the best compromise between minimising both the residual data misfit χ^2 and the model norm $|m|^2$. Models far from the bending are either dominated by noise ("vertical" part of the curve with high $|m|^2$ values) or the data is poorly exploited in them ("horizontal" part with high χ^2 and low $|m|^2$ values). However, there is a subjectivity inherent to the choice of models close to the bending of the L-curve due to the poor knowledge of data uncertainties.

Zaroli et al. (2013) proposed an objective rational for the choice of damping. We follow the first part of that procedure in which one segment of the L-curve can be ruled out by generating l_∞-norm as a function of χ^2. Fig. 4.14

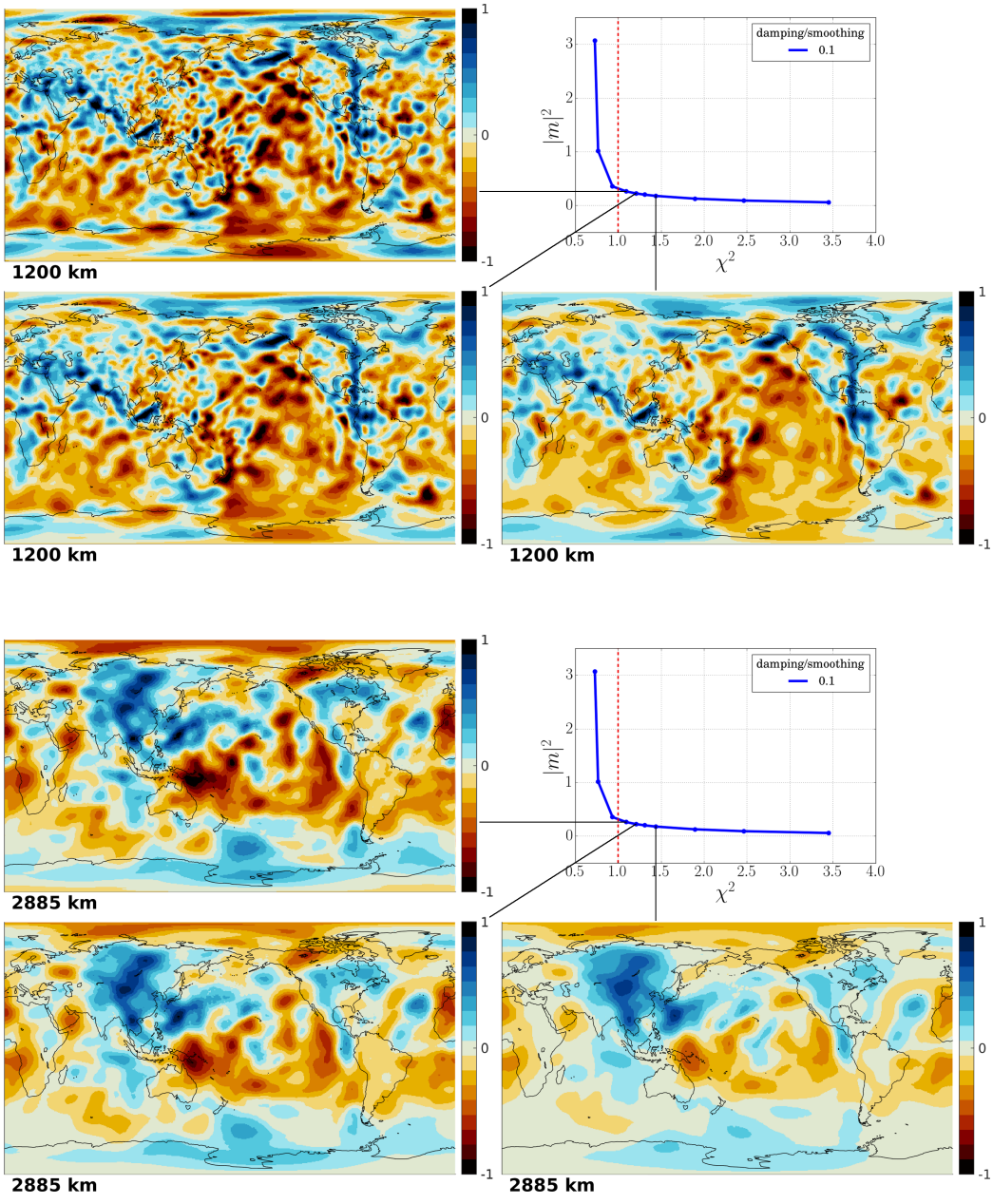

Figure 4.12: Trade-off between the model norm and the residual data misfit by changing the damping and smoothing parameters. Effects of regularisation at two depths 1200 (top) and 2885 km (bottom) are compared visually. In all cases, the ratio $\frac{damping}{smoothing} = 0.1$ is constant, but the intensity of regularisation parameters were changed.

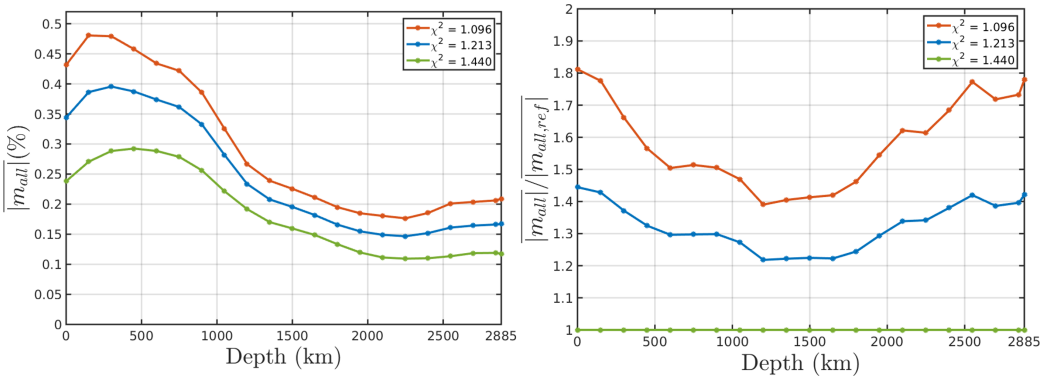

Figure 4.13: Changes in the mean of absolute velocity anomalies in three tomography models of Fig. 4.12 due to regularisation. The ratios between the means of models with $\chi^2 = 1.096, 1.213$ with respect to $\chi^2 = 1.440$ (reference) show that amplitudes are affected differently in depths, and they can be changed up to a factor of two (right panel).

shows this for three examples with $\frac{damping}{smoothing} = 0.5, 0.3, 0.1$. Starting from an over-regularised model in one of the three cases and decreasing the intensity of regularisation, (tracing one of the curves from right to left in Fig. 4.14, right panel), the maximum amplitude of the model parameters increases smoothly with a sudden change around $\chi^2 = 1$. This sudden increase in the amplitude of at least one model parameter is considered to be the beginning of the noise-dominated tail of the L-curve ("vertical" part) from which no model was accepted.

In the examples of Figs 4.13 and 4.14, one set of damping and smoothing parameters was applied to all the unknowns (model parameters). Alternatively, regularisation with a constant smoothing operator but with locally adjusted damping parameters was also tested. The local adjustment was done by grouping the model parameters with similar kernel values and assigning a scaling factor for damping to each group as it is shown in Fig. 4.15.

Solutions obtained from locally adjusted regularisation showed velocity anomalies with lower amplitudes in poorly sampled regions while the amplitudes of other model parameters were unaffected. This method helps to go beyond the limitations of globally constant regularisation in which the highly resolved regions will be over-regularised to account for the lack of data in other regions, or unknowns with poor data coverage will be under-regularised to keep the resolution of highly-sampled parameters. However, a downside to this approach is the selection of scaling factors which is rather

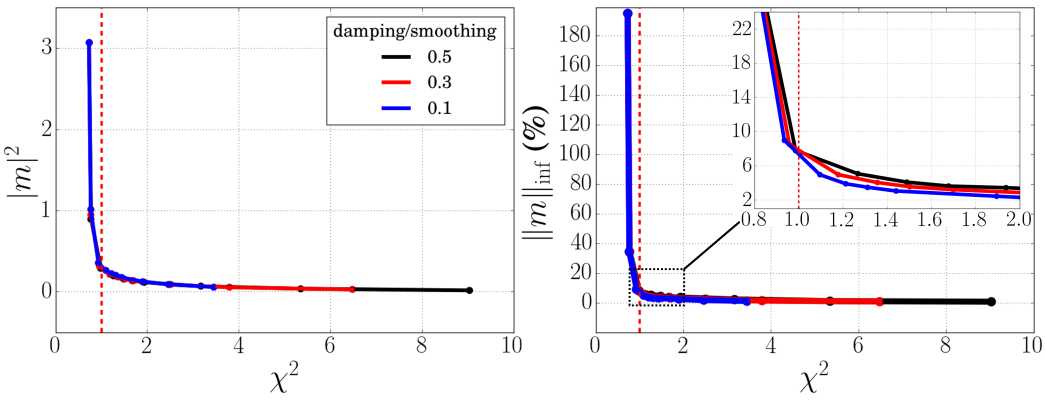

Figure 4.14: Selection of damping and smoothing parameters using $|m|^2$ and l_∞-norm. L-curve (left panel) shows the trade-off between the model norm $|m|^2$ and the residual data misfit χ^2 for three examples with $\frac{damping}{smoothing} = 0.5, 0.3, 0.1$ (legend). Normally, the models around the bending of this curve are considered as the possible solutions to the inverse problem as they compromise between models with poorly-exploited data (over-regularised) and noise-dominated ones. To systematically rule out some of these models, we follow the method of Zaroli et al. (2013) in which l_∞-norm as a function of χ^2 is generated (right panel). Models with $\chi^2 < 1$ show much higher amplitudes compared to the slightly more regularised models. These models were considered to be on the noise-dominated tail, and they were excluded from the possible solutions.

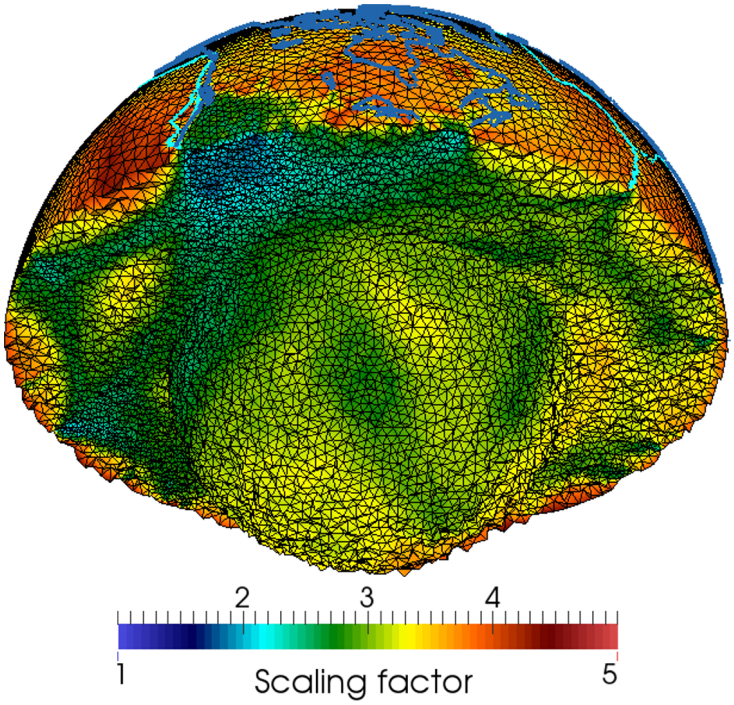

Figure 4.15: Norm damping parameters were adjusted locally according to the sensitivity kernel values at each node. Here, the scaling factor at each model parameter is shown which is used to fill in L matrix in eq. 4.7. For regions with poor data coverage (e.g., East Pacific), damping parameters are scaled up more strongly compared to well-illuminated regions (e.g., beneath North America).

arbitrary. Here, the cumulative column density of A matrix, $\log_{10}(\sum_i A_{ij})$, was used to assign the scaling factors for damping to model parameters.

Different parameter settings (e.g., changing the $\frac{damping}{smoothing}$ ratio) were experimented using the whole or only a subset of data vector, and a set of models close to the critical points of $l_\infty - \chi^2$ curves were chosen as possible solutions to the inverse problem. In the next step and to narrow down the selected model solutions, various resolution tests were performed in which synthetic data vectors d^{syn} were constructed based on the input model vectors m^{inp}:

$$d^{syn} = Am^{inp} \tag{4.12}$$

Solutions were then obtained through the same inversion procedure, and the outputs were compared with the input synthetic models. This checks

two aspects of the inversion: data coverage and the choice of regularisation parameters (in other words, deviations of the retrieved structures from the input models indicate either poor data coverage or strong/weak regularisation).

An example of the resolution test is shown in Fig. 4.16. In the mid and lower mantle where our data coverage is at its best, the recovered (output) patterns by the inversion (using realistic regularisation and noise) are well resolved (right columns). In the upper mantle, the resolution is controlled by the uneven distribution of stations and sources. As a result, well-resolved patterns are mainly beneath the continents and source locations as well as the bouncing points of PP measurements. In the lowermost mantle, the patterns are retrieved very well in the northern hemisphere, but less well in the southern hemisphere.

4.5.2 Mantle heterogeneity inferred from a global tomography model

A global multiple-frequency tomography model was selected based on the method described in Section 4.5.1. In the following, first-order structural features of this model will be briefly discussed, and the results will be compared with two global P wave models: PRI-P05 (Montelli et al., 2006) and MIT-P08 (Li et al., 2008).

Similar to PRI-P05, our model was derived by using both cross-correlation traveltime measurements and picked arrival times. In PRI-P05, $\approx 90K$ finite-frequency measurements with 20 s dominant period were combined with $\approx 1.5M$ short-period traveltimes from bulletins (Montelli et al., 2004b). We used $2.5M$ multifrequency measurements with dominant periods from 30.0 to 2.7 s combined with $\approx 3.4M$ picked arrival times from EHB catalogue. The models were parameterised by tetrahedra in both cases with 19,279 nodes in PRI-P05 and 396,501 nodes in our model. On the other hand, the main data source in MIT-P08 was picked arrival times ($\approx 15.2M$ records with $4.1M$ composite rays) combined with cross-correlation measurements ($\approx 21K$), and rectangular cells were used to discretise the model. All three models employed data-driven parameterisation techniques in which more nodes are considered in regions with better data coverage.

We start with the structural features in the lowermost mantle. In most global P wave tomographies, data in the far teleseismic range, which effectively starts to sense the core (generally neglecting by the sensitivity modelling), is included to illuminate the lower mantle, but they stop short of including "real" Pdiff data. Sparser sampling and poorer modelling result

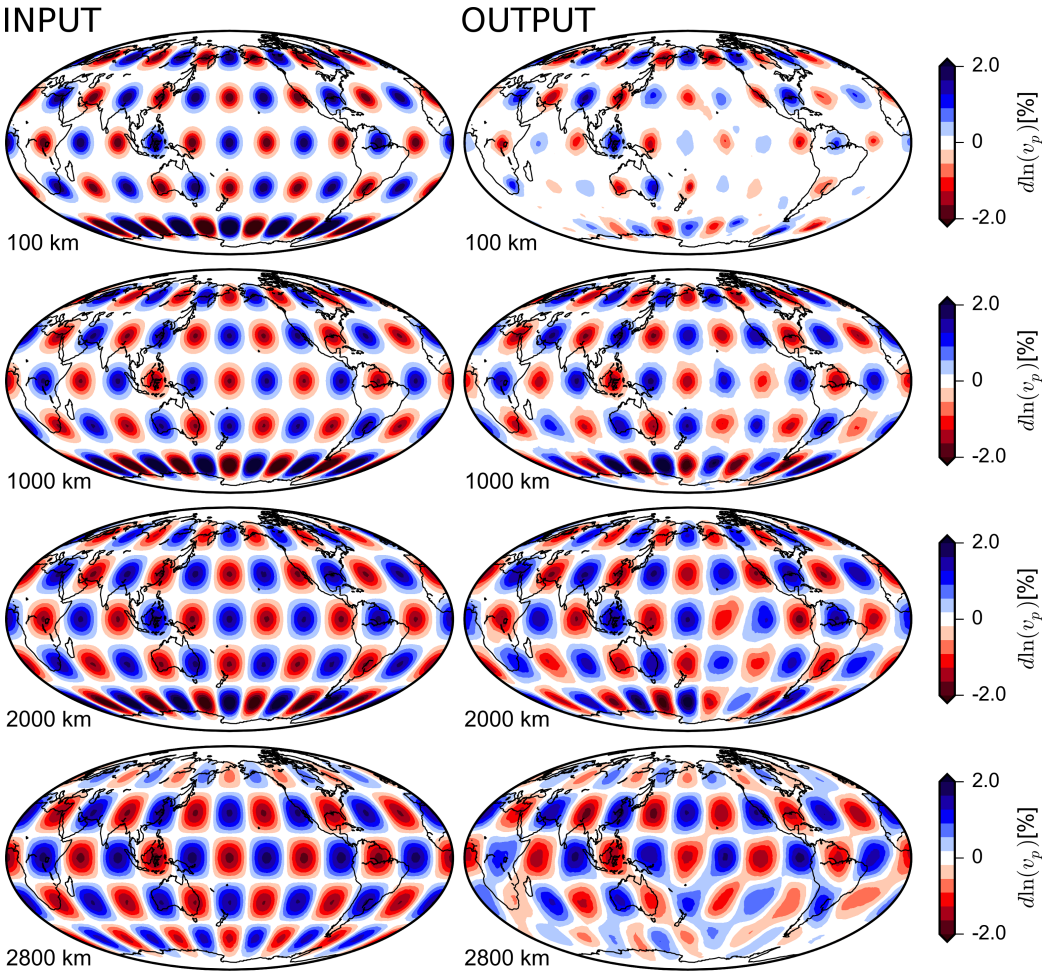

Figure 4.16: Resolution test. 2-D sections at 100, 1000, 2000, and 2800 km depth through input (left column) and output (right column) patterns. In each block of the input pattern, the centre has the highest velocity perturbation of $\delta ln(V) = \pm 3\%$, and velocity profiles are extended laterally with a three-dimensional Gaussian function. The recovered (output) patterns were retrieved by the inversion using realistic regularisation and noise.

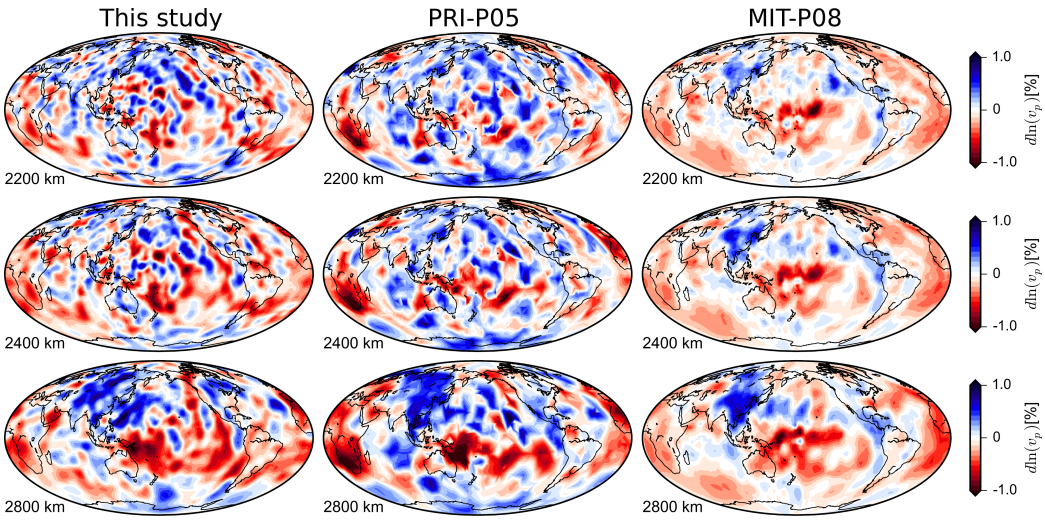

Figure 4.17: Visual comparison of our preferred model with two other global P models: PRI-P05 (Montelli et al., 2006) and MIT-P08 (Li et al., 2008). Sections through the lower mantle (2200, 2400 and 2800 km) are projected to the earth's surface. Colours indicate the compressional velocity perturbations, $dln(V_p)$, with respect to IASP91 background model.

in coarser image resolution and significant discrepancies across tomographic models, even for large-scale features. Fig. 4.17 shows this by comparing our model with PRI-P05 and MIT-P08 at selected depth sections in the lower third of the mantle (2200, 2400 and 2800 km).

Several common structures at 2800 km depth can be detected visually in the three models of Fig. 4.17: two Large Low Shear Velocity Provinces (LLSVPs) beneath Africa and Pacific and seismically fast areas under most of the eastern Asia and under Central America. The models also agree on some less well-resolved structures, such as high-velocity anomalies under the Central Atlantic and east of Indian ocean.

LLSVPs have been previously detected in global (P and S) tomography models (e.g. Woodhouse and Dziewonski, 1989; Masters et al., 2000; Mégnin and Romanowicz, 2000; Grand, 2002; Ritsema and van Heijst, 2002; Montelli et al., 2006); however, discrepancies still exist in the geometries and distribution of low-velocity anomalies, their relation to presumed hotspot locations and the subdivisions of LLSVPs at lowermost mantle. As an example, all the models in Fig. 4.17 show a low-velocity anomaly beneath west of Pacific while the retrieved structures vary between them in the Central and eastern

Pacific. This lack of consistency, especially in the southern hemisphere, may be due to the sparse sampling and poor data coverage in these regions.

A relatively small-scale but pronounced feature in our model at 2800 km depth is a slow patch just west of Hawaii. This structure was described by Cottaar and Romanowicz (2012) as a newly recognised Ultra-Low Velocity Zones (ULVZs). Both PRI-P05 and MIT-P08 imaged a high-velocity structure in this region.

Another common structure across the models of Fig. 4.17 is a seismically fast area under eastern Asia that extends to Central Pacific. This high-velocity anomaly (associated with subducted slab accumulations) is also detectable in 2200 and 2400 km depths. In MIT-P08 model, the high-velocity structure imaged in Pacific stays almost constant across 2400 to 2800 km depth and tends to fade around 2200 km. In PRI-P05 and our model (2400 km cross section), two distinct long linear features are imaged. One starts from the north of Pacific which extends to eastern Pacific, and the other extends from west to Central Pacific.

Compare to the lower mantle, the correlation between the models in the mid mantle varies spatially. Fig. 4.18 shows this for the models averaged over 960-1510 km depth. All three models show an excellent correlation in linear high-velocity features beneath America and the southern Eurasia. Detailed tectonic or paleogeographic interpretations of these long, but relatively narrow (with only several hundred kilometres apparent width) features have been proposed by many regional and global tomographies at upper and mid mantle depths (e.g. for Tethyan slabs beneath the southern Eurasia: Van der Voo et al. (1999b); Hafkenscheid et al. (2006); for North America: Grand (2002); Ren et al. (2007); Pavlis et al. (2012); Sigloch and Mihalynuk (2013); globally: Li et al. (2008); van der Meer et al. (2010)). These seismically fast regions were associated with the sites of ancient subduction still visible in the mantle due to their spatial correlation with the subduction-related seismic zones. Moreover, based on the depths to which they extend, it was suggested that slabs in some arc systems may descend well into the mid and even lower mantle. Despite the consistency between the models in these provinces, there is a large discrepancy between them in regions with poor data coverage, for example, below the Pacific.

Teleseismic measurements were the main data source in our tomography model and PRI-P05. Consequently, the resolution at the shallow depths is controlled by the uneven distribution of sources and receivers. Fi. 4.19 shows the extent to which PRI-P05 and our model agree beneath Europe and its surrounding area at 100 and 500 km depth. The two models correlate strongly in long and intermediate wavelength structures: mid-Atlantic ridge as a seismically slow region, high-velocity structure in the eastern Europe,

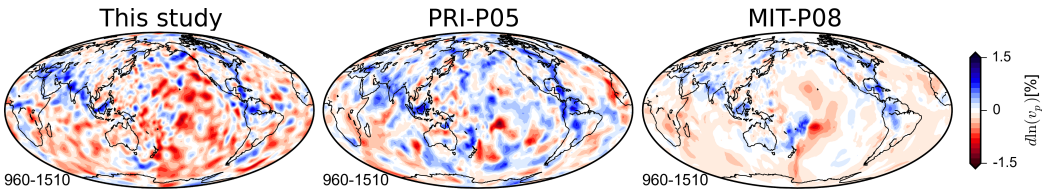

Figure 4.18: Visual comparison of our preferred model with PRI-P05 and MIT-P08 in the mid mantle. The models are averaged over 960-1510 km depth and they are projected to the earth's surface. Colours indicate the compressional velocity perturbation with respect to IASP91 background model.

velocity anomalies beneath Africa, and (to some extent) on the structures under Greenland and middle-East. Moreover, many of the small-scale features in the European upper mantle retrieved by our model, such as slabs and upwellings, are consistent with existing tomography models of this region. One example for this (at 100 km depth) is the sharp boundary between the westerly low velocities under Central Europe and the seismically fast area beneath the eastern Europe. This feature under the Tornquist-Teisseyre Zone was inferred as a boundary between Precambrian East European Platform and younger (Phanerozoic central and eastern) parts of Europe (e.g. Zielhuis and Nolet, 1994; Zhu et al., 2012). At 500 km depth, a high-velocity structure beneath the southern Europe is detectable consistent with regional studies (e.g. Wortel and Spakman, 2000; Zhu et al., 2012).

Another example of the mantle structure beneath Europe imaged by our model is shown in Fig. 4.20. Vertical (great-circle) cross-sections through PRI-P05 and our tomography model are compared in the southeast of Europe. Both models show a seismically fast anomaly from the surface down to the lower mantle. This structure was previously detected and associated with continuous northward subduction and accretion of the Aegean mountain belt (van Hinsbergen et al., 2005; van der Meer et al., 2010).

Mantle structure beneath North America is, perhaps, one of the best seismically imaged regions due to the dense seismic networks, hundreds of stations, in the United States and surrounding area. Fig. 4.21 depicts mantle lateral heterogeneities beneath America imaged by our model and PRI-P05. At 1300 km depth, the long-wavelength ancient Farallon slab appears mainly beneath eastern North-America in both models. Our model also features a clear detached slab fragment beneath Central North-America.

Fragments of the Farallon slab throughout the mantle have been previously discussed in details based on high-resolution, regional-scale seismic tomography studies (Sigloch et al., 2008; Tian et al., 2009; Sigloch and Mi-

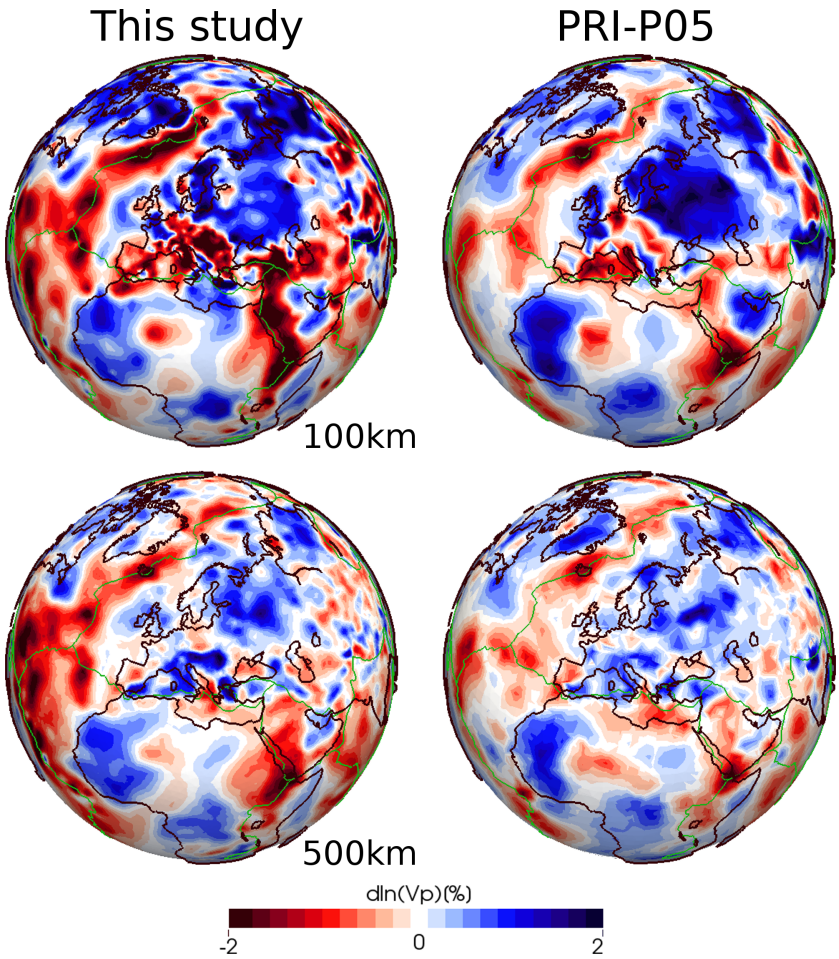

Figure 4.19: Comparison between PRI-P05 (Montelli et al., 2006) and our model at shallow depths. Sections through 100 and 500 km depth are projected to the earth's surface. Colours indicate the compressional velocity perturbations with respect to IASP91 background model. Black lines: continents; green lines: tectonic plates.

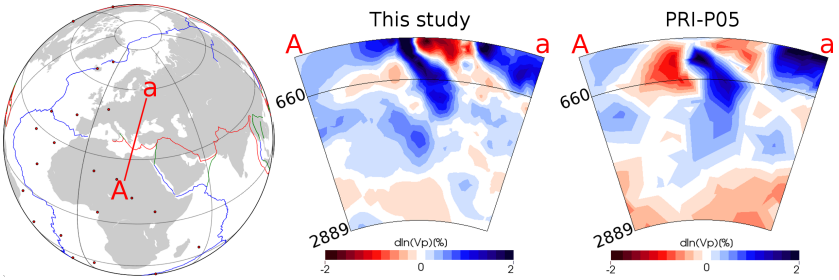

Figure 4.20: Vertical cross-section through PRI-P05 and our model in the mantle structure below the southeast of Europe. The high-velocity structure imaged by both models extends from the surface down to the lower mantle. Colours indicate the compressional velocity perturbations with respect to IASP91 background model.

halynuk, 2013). In our model, sharp outlines of fast anomalies emerge in all mantle depths beneath North America. Fig. 4.22 shows this complex subduction system and compares it with PRI-P05 in a vertical whole-mantle depth cross-section.

Although the three models show high correlation for many large-scale structures throughout the mantle, the geometries of the imaged features, especially for the structures with short and intermediate wavelength, differ significantly between them. PRI-P05 and our model also tend to show slightly larger amplitudes than MIT-P08 in almost all the mantle depths. These differences can be due to the theoretical framework (finite-frequency effects, sensitivity kernels and forward modelling), data coverage (the sampling of the mantle by seismic waves), and inversion techniques (e.g., regularisation) used to derive the tomography models.

4.6 Conclusion

We presented a global multiple-frequency tomography model of V_p variations in the mantle. The model was derived by incorporating a very large set of core-diffracted P-phase measurements (Pdiff) alongside conventional teleseismic P and PP. All phases were measured and modelled from 30 s dominant period to the highest frequencies that produce satisfactory fits (≈ 3 s) which resulted in 1,550,587 multifrequency P, 577,106 PP and 391,320 Pdiff traveltime observations. The measurements were linked to the model-parameters (3-D velocity structure) with Born scattering kernels to correctly model the dispersion in the multifrequency traveltime observations. By using the am-

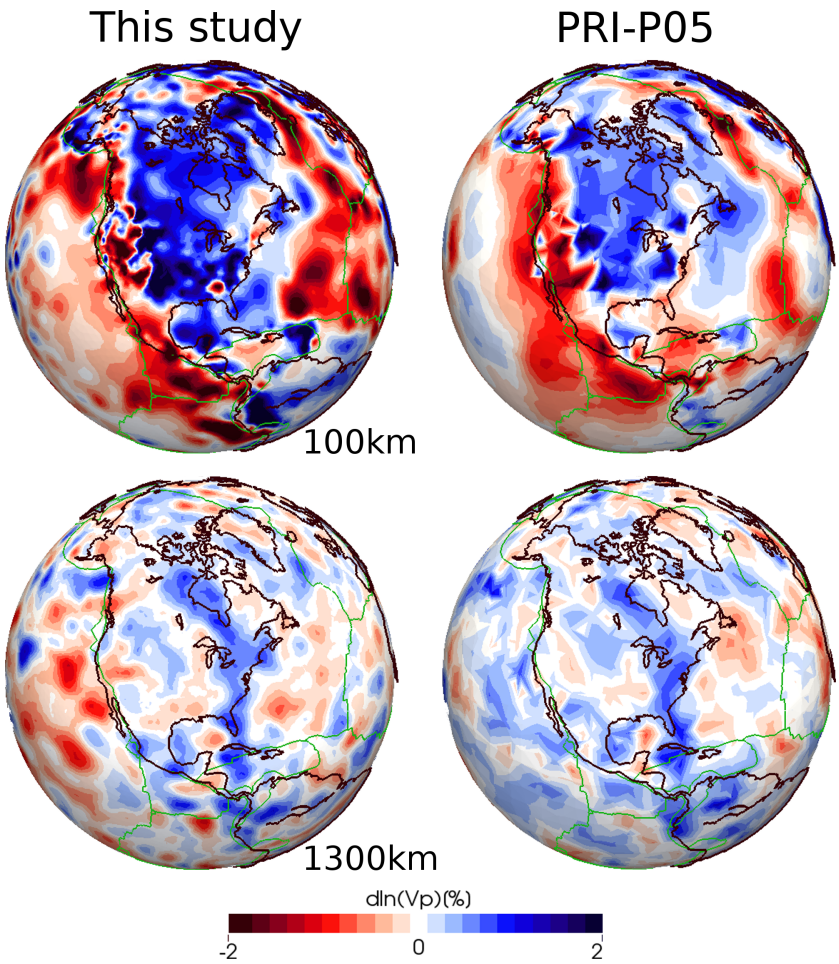

Figure 4.21: Comparison between our model and PRI-P05 (Montelli et al., 2006) in lateral heterogeneities imaged under North America. Sections through 100 and 1300 km depth are projected to the earth's surface. Colours indicate the compressional velocity perturbations with respect to IASP91 background model. Black lines: continents; green lines: tectonic plates.

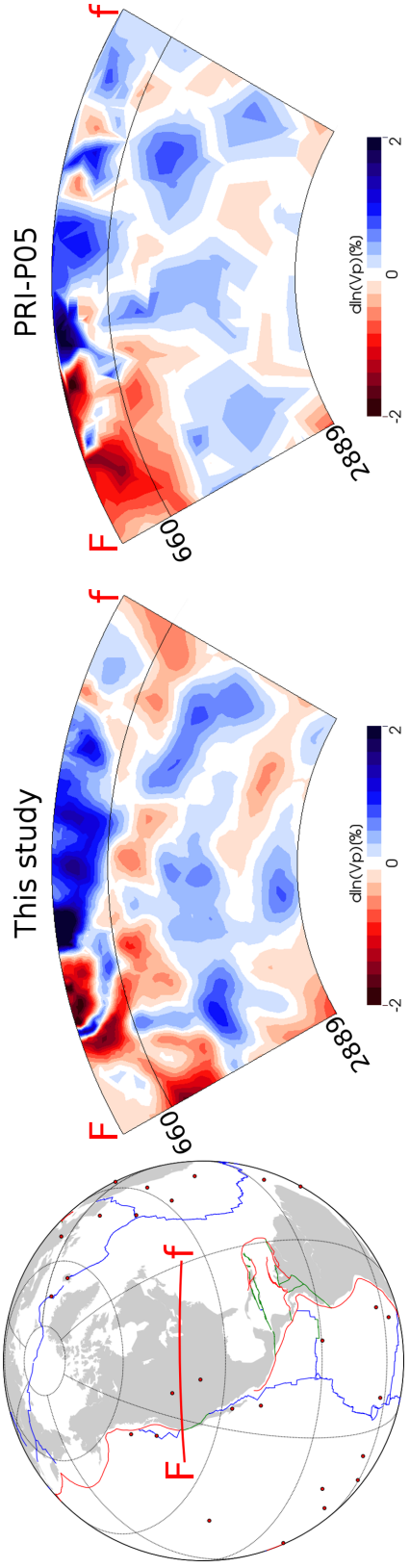

Figure 4.22: Vertical cross-section through our model and PRI-P05 in the North American mantle from the surface down to the CMB (2850 km). Colours indicate the compressional velocity perturbations with respect to IASP91 background model.

plitudes of sensitivity kernels, the model was parameterised adaptively by tetrahedra; edge-lengths were adjusted locally based on the expected resolution. The matrix inversion was done by an iterative conjugate gradient method, and both norm damping and smoothing were used for regularisation. A two-step approach in selecting the model(s) was employed in which the preferred solution(s) was obtained by using $|m|^2$ and l_∞-norm of the model parameters. Moreover, the choice of the regularisation in the selected models was checked by resolution tests through the same inversion procedure on known synthetic inputs.

Our preferred multiple-frequency tomography model was shown at selected depths through the mantle. Its major structural features were briefly discussed, and it was compared visually with two other global P-velocity models. The results showed high correlation for many large-scale structures throughout the mantle. However, large discrepancies still exist in the geometries of the imaged features which emphasises the need for high-quality models to better understand the geological and geodynamical processes driving the earth.

5

Global lower mantle structure from multiple-frequency seismic tomography

Abstract

We present multi-scale lower mantle structure derived from a global multiple-frequency seismic tomography. This broad-band waveform inversion seamlessly incorporates multifrequency Pdiff observations alongside a very large data set of conventional teleseismic P and PP measurements. An inversion framework with adaptive parameterisation and locally-adjusted regularisation is developed to accurately map the information of these measurements onto the desired model parameters (dV_p/V_p). The P wave velocity images show the geometries of seismically fast anomalies representing subducted slabs still visible in the mantle, low-velocity anomalies and their relation to presumed hotspot locations and the subdivisions of Large Low Shear Velocity Provinces at the base of the mantle. Our model confirms the presence of several previously imaged mantle plumes. At the same time, it provides tomographic evidence to support the existence of deep-mantle plumes beneath Iceland and Tristan da Cunha. We trace some of these structural findings throughout the mantle to investigate their morphological characteristics in a large (whole-mantle) context. Moreover, considerable structural complexities

in the lower mantle beneath north America and eastern Asia, dominated by seismically fast anomalies, are discussed and visualised by using a three-dimensional rendering technique. Our results reveal extensive high-velocity anomalies from the northwestern Pacific to eastern Eurasia at the root of the mantle. In western Pacific, two distinct linearly elongated high-velocity features are imaged by our model. Moreover, a seismically fast structure that covers north America and extends to the northwestern Colombia is apparent in the P wave velocity images.

5.1 Introduction

The Core-Mantle Boundary (CMB) is a thermal and chemical boundary layer at the base of the mantle ($\approx$ 2900 km depth) which separates the liquid outer core from the solid lower mantle (Lay, 1989; Loper and Lay, 1995). Seismological observations have provided, perhaps, most of the direct information about the lower third of the mantle from localised scattering studies (e.g. Weber and Davis, 1990; Thomas et al., 2004; Hutko et al., 2006; van der Hilst et al., 2007; Kito et al., 2007) to global tomography models (e.g. Woodhouse and Dziewonski, 1989; Masters et al., 2000; Mégnin and Romanowicz, 2000; Grand, 2002; Ritsema and van Heijst, 2002; Montelli et al., 2006; Li et al., 2008). In these studies, strong variations in seismic velocity and anisotropy were observed that suggest a high level of complexity in the deep mantle structure. However, discrepancies still exist across these models mainly due to differences in data coverage and modelling technique. In most global tomography models, the lowermost mantle is only marginally sampled by data in the far teleseismic range, which effectively starts to sense the core, but they stop short of including "real" core-sensitive data. Sparser sampling and poorer modelling result in much less confidently imaged anomalies in the lower third of the mantle (Wysession, 1996a). However, there is a significant effort underway in seismic tomography and localised studies to improve the spatial resolution and coverage of the lower mantle in order to provide a detailed picture of this region.

In this study, we present the results of a whole-mantle multiple-frequency tomography model based on teleseismic and core-diffracted P waves. This broad-band waveform inversion has two main features to effectively increase the illumination of the lower mantle compared to previous global P models:

1. A multifrequency measurement technique (Sigloch and Nolet, 2006; Hosseini and Sigloch, 2015) is employed that systematically exploits

the seismic phases from 30 s to the highest frequencies that produce satisfactory fits between observed signals and numerically simulated waveforms (≈3 sec).

2. A very large set of core-diffracted P-phase measurements (Pdiff) is included to a global teleseismic P and PP inversion. Pdiff waves dive deep enough to sense the Earth's core and diffract around the CMB. This makes them the most highly-resolving wave type that extensively sample the deep mantle.

This way, 1,550,587 multifrequency P, 577,106 PP and 391,320 Pdiff traveltime observations were obtained and used in the actual inversion. These measurements were linked to the model parameters (3-D velocity anomalies) using Born scattering kernels (Marquering et al., 1998; Dahlen et al., 2000; Hung et al., 2000), which are capable of modelling the dispersion in the multifrequency traveltime observations. We do not simultaneously invert for the CMB topography since the sensitivity of Pdiff waveforms to the topography should be negligible (Colombi et al., 2012, 2014).

Our tomography model confirms several structures at 2800 km depth which were revealed previously in regional and global studies (Fig. 5.1): two Large Low Shear Velocity Provinces (LLSVPs) at the root of the mantle beneath Africa and Pacific and seismically fast areas under most of the eastern Asia and under Central America. The model also shows high-velocity anomalies under the Central Atlantic, the eastern Indian Ocean, and Antarctica. The relation of these provinces at the CMB to the lower mantle and to the shallower depths will be discussed in Sections 5.2 and 5.3 for low- and high-velocity features, respectively.

5.2 Large Low Shear Velocity Provinces (LLSVPs)

Whole-mantle (S and P) tomography studies have hinted at two large low-velocity provinces that dominate the seismically slow structure of the few hundred kilometres above the CMB (e.g. Dziewonski et al., 1977; Woodhouse and Dziewonski, 1989; Masters et al., 2000; Mégnin and Romanowicz, 2000; Grand, 2002; Ritsema and van Heijst, 2002; Montelli et al., 2006; Simmons et al., 2010; Auer et al., 2014; Koelemeijer et al., 2016). Although these structures are particularly prominent in global S-wave tomography models, a relatively weaker expression of them has also been detected in P wave velocity images. In our model, these two LLSVPs are apparent beneath Africa and the Pacific at 2800 km depth (Fig. 5.1). The mapped structures are consistent with previous global P models (Montelli et al., 2006; Li et al., 2008),

Figure 5.1: Maps of the P wave velocity variations imaged by our model at the lower mantle (2200, 2400 and 2800 km) projected to the Earth's surface. On large scales, the velocity anomalies at the CMB (2800 km) show several previously imaged structures in global tomography models, such as LLSVPs beneath Africa and Pacific and seismically fast areas under eastern Asia and Central America. See text for further discussion. Colours indicate the compressional velocity perturbations, $dln(V_p)$, with respect to IASP91 background model.

especially in the low-velocity heterogeneities beneath the southwestern Pacific (Fig. 5.2a). In the northern border of this LLSVP (southwest of Hawaii), a relatively small-scale but pronounced feature is also imaged in our model. This structure was described as a newly recognised Ultra-Low Velocity Zone (ULVZ) with the diameter of $\approx$ 910 km by Cottaar and Romanowicz (2012).

The other LLSVP covers the lower mantle under Africa and the south Atlantic (Fig. 5.2c). Although the Pacific LLSVP appears as several plumes as opposed to the broad low-velocity structure of the African LLSVP, it is beyond our detection capabilities to interpret this difference as morphological characteristics. Moreover, compared to the Pacific LLSVP, the seismically slow anomalies imaged under Africa and the Atlantic have generally lower amplitudes. This difference cannot be directly related to the amplitudes of the "actual" structural features since data coverage, regularisation and parameterisation can produce similar effects (decreasing the amplitudes). Tkalčić et al. (2015) employed a trans-dimensional and hierarchical Bayesian imaging to overcome these limitations. Their model shows even higher amplitudes under Africa compared to the low-velocity structure beneath the western Pacific. This poor correlation emphasises the uncertainties that exist in the mapped structural features across different tomography models which make the detailed interpretation of the amplitudes challenging, if possible at all.

Complex structures at the CMB are expected to interact with the rest of the mantle through heat and mass transfer. One example of this interaction observed at the surface is global volcanism. Although the theory of plate tectonics provides the framework to account for much of these activities, it cannot explain hotspot volcanoes, which are often remote from the plate boundaries. One possible origin of hotspot volcanoes was first proposed by Morgan (1971) as mantle plumes upwelling from the Earth's lowermost mantle. Several studies have discussed this relation based on whole-mantle tomography models, especially for the LLSVPs and presumed hotspot locations (Montelli et al., 2004b; French and Romanowicz, 2015). However, the debate over the viability of this concept – do mantle plumes exist? how deep are their roots? – continues to this day accompanied by alternative proposed origins for the hotspots, such as shallow convective processes and tensional cracking of the lithosphere beneath volcanic islands (Anderson, 2005).

We employ a three-dimensional rendering technique to assess this relation in the lower mantle: the imaged low-velocity anomalies, associated with the Pacific and African LLSVPs, are shown from the base of the mantle up to 500 km above the CMB in Fig. 5.2(b) and (d), respectively. The structures extend almost vertically in some locations (e.g., south and southwest of Hawaii) while they stay close to the CMB or rise with a gentle slope in

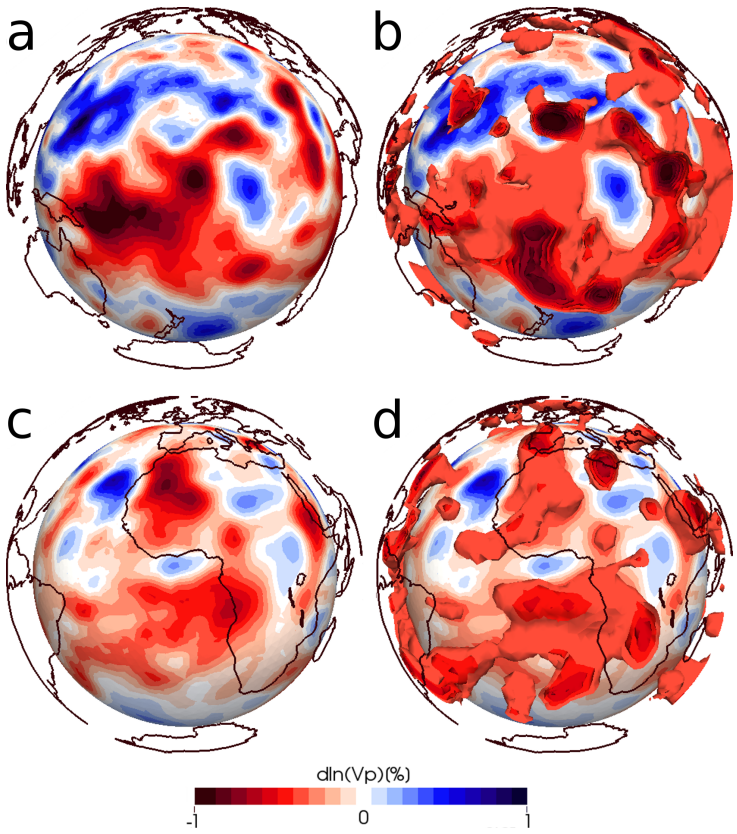

Figure 5.2: Low velocity structures imaged by our model at the base of the mantle. Panels a and c show the structures at 2800 km depth beneath the southwestern Pacific and Africa, respectively. Panels b and d render the three-dimensional seismically slow anomalies 500 km above the CMB beneath the southwestern Pacific and Africa. The isosurface threshold is $-1.0\% \leq dln(V_p) \leq -0.4\%$ in increments of 0.1%. Colours indicate the compressional velocity perturbations, $dln(V_p)$, with respect to IASP91 background model. Note that the continental outlines are at 500 km above the CMB.

other regions. Some of these anomalies, in both LLSVPs, reach to the upper mantle. To trace these low velocities through the whole mantle, we limit our analysis to two exemplary cases: Iceland as a (relatively) well-instrumented region and Tristan da Cunha as a poorly sampled one. (See Figs A.1-A.3 in Extended Data for the imaged structure beneath Afar hotspot).

Iceland lies along the northern sector of Mid-Atlantic Ridge. In addition to spreading ridge (divergent boundary) activity, a plume origin for this hotspot has been suggested based on seismological, observational, laboratory and numerical investigations (Bijwaard and Spakman, 1999). Almost all tomography models agree on the existence of an upper-mantle plume beneath Iceland (Bijwaard and Spakman, 1999; Ritsema et al., 1999; Hung et al., 2004; Montelli et al., 2006; Rickers et al., 2013); however, there are still discrepancies between the models at depth. This can be better seen in the vertical cross-sections through our model under Iceland (Fig. 5.3) compared to the global finite-frequency tomography model of Montelli et al. (2006), PRI-P05. The two models agree on the general structure of the low-velocity heterogeneities in the mid and upper mantle; however, a noticeable difference exists between them at the base of the mantle. Our model shows a continuous low-velocity conduit from the CMB to the upper mantle while this cannot be confirmed from PRI-P05.

To test the robustness of the low-velocity column under Iceland, two resolution tests were performed (Figs 5.4 and 5.5). The input model in both tests was a 3-D cylinder with 400 km radius and with a Gaussian distribution of lateral amplitudes. In one case (Fig. 5.4), the column spans the whole mantle (from the surface down to the CMB) while in the other case (Fig. 5.5) the synthesised plume only reaches to the mid mantle ($\approx$ 1500 km). The recovered structures in both tests are well-resolved throughout the mantle. The retrieved model also shows no vertical leakage (Fig. 5.5). The results suggest that we have adequate resolution to image the mantle provinces beneath Iceland, and that the deep-rooted low-velocity conduit was required by our traveltime observations.

The earth's mantle beneath the south Atlantic is a region where we can expect mantle circulation to be driven in large part from below. The absence of subduction since the breakup of Gondwana suggests that any upwelling structures in the vast African anomaly – a superplume, plume clusters, or individual plumes – should have had space and time to evolve into rather "pure", undisturbed realisations of their kind. Here, we turn to the structural information imaged by our model beneath Tristan da Cunha as the southern member of the Atlantic plume cluster.

Tristan da Cunha is categorised as a "primary" (deep-rooted) plume mainly based on its clear hotspot tracks along the Walvis Ridge and Rio

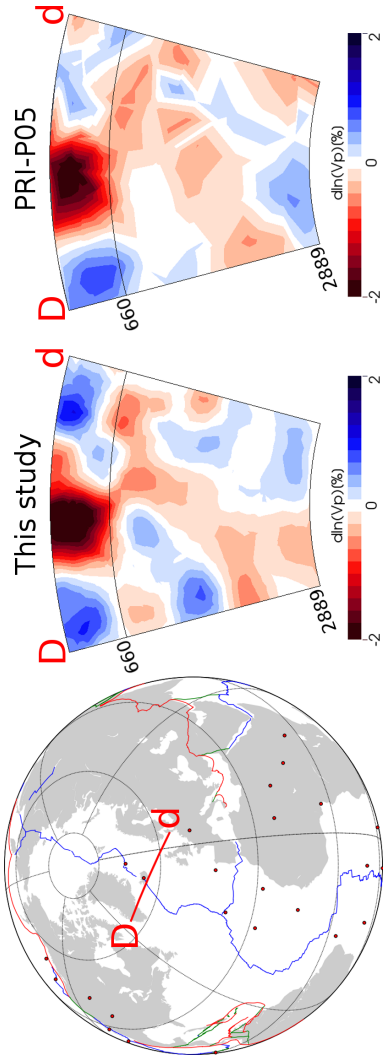

Figure 5.3: Vertical cross-sections through our model and PRI-P05 in the mantle structure below Iceland. The section is shown in the map (left). Both models agree well in the low-velocity anomalies in the upper and mid mantle, which is encouraging given that the two maps are made with independent data. However, there are some disagreements between them mainly in the lowermost mantle in which our model features a seismically slow anomaly and a continuous conduit from the CMB to the upper mantle. Colours indicate the compressional velocity perturbations, $dln(V_p)$, with respect to IASP91 background model. Red dots represent the global hotspot distribution according to Steinberger (2000).

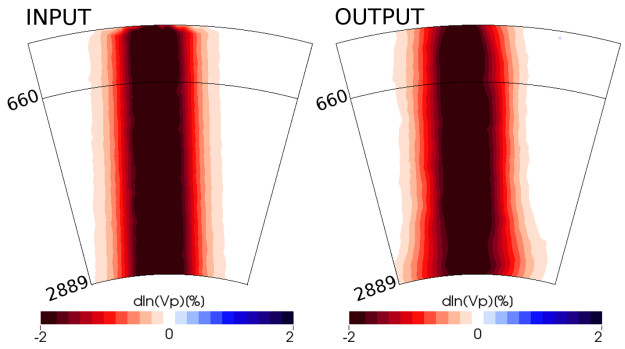

Figure 5.4: Resolution test. The input pattern is a 3-D cylinder with a Gaussian lateral velocity profile $dV_p/V_p = (dV_p/V_p)_{centre} exp(-r^2/w^2)$ with radius $w = 400$ km; centred at Iceland. The highest velocity perturbation $(dV_p/V_p)_{centre}$ in the centre of the cylinder is -3%. Left panel shows the input pattern, and right panel shows the output pattern retrieved by the inversion (using realistic regularisation and noise). The column is recovered very well almost in all depths; however, the output anomalies at the base of the mantle are slightly smeared which should be irrelevant for the interpretation of structural features in this study.

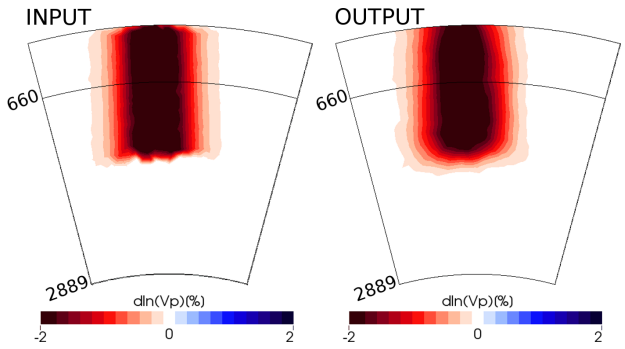

Figure 5.5: Resolution test. Like Fig. 5.4, except that the input column extends from the surface to the mid mantle (1500 km). This tests the effects of regularisation and data coverage on the vertical leakage. The recovered column preserves the depth of the input model well. This suggests that the observed extension of the model to the CMB was required by our traveltime measurements.

Grande Rise, the existence of the Parianá and Etendeka continental flood basalts at the origin of these tracks and its large buoyancy flux (Courtillot et al., 2003). Morgan (1972) was the first to interpret the Walvis Ridge and Rio Grande Rise as the result of plates moving away from a fixed hot-spot located on the crest of a spreading mid-ocean rise.

However, due to the sparse source and receiver distribution, the mantle beneath the south Atlantic is one of the most poorly illuminated regions, especially for body wave tomography. Therefore, there are only limited seismic studies that support the presence of a deep mantle plume beneath Tristan da Cunha with no conclusive interpretation. As an example, Ritsema and Allen (2003) has probed for a deep mantle plume beneath Tristan. They did not observe a classical conduit into the lower mantle, but they also noted resolution concerns.

In this study, a large set of P, PP and Pdiff seismic phases were measured using a multifrequency measurement technique to further improve the resolution beneath the south Atlantic. The overall coverage was enhanced, but several regions in the upper and mid mantle are still poorly constrained. Hence, the geometries of the imaged structures are not as detailed as the Iceland example.

A vertical cross-section through our model beneath Tristan da Cunha is shown in Fig. 5.6, and is compared with the global tomography model of Montelli et al. (2006). Our model shows a continuous low-velocity structure from the CMB to the surface. In the mid mantle, this plume appears to be strongly deflected towards the southwest. PRI-P05 images a seismically slow anomaly in the upper mantle and to some extent in the mid mantle, but its continuous extent to the lower mantle can not be confirmed from this model.

Note that in both cases (Iceland in Fig. 5.3 and Tristan da Cunha in Fig. 5.6), the low-velocity columns start spreading laterally at around 1000 km depth. This horizontally elongated branches extend from the plume stems suggest that the flow may have encountered resistance to direct continuation into the upper mantle.

Resolution tests with similar setup as Iceland were performed for Tristan da Cunha (Figs 5.7 and 5.8). In both tests, the recovered anomalies tend to smear laterally in the mid mantle which may be caused by the lack of data in this depth range. In the lower mantle, the retrieved structures show higher resolution in terms of shape and amplitude. This is due to the inclusion of Pdiff measurements. These waves travel long distances and possibly illuminate the lower third of the mantle better than the mid mantle in this region. In the upper mantle, the recovered velocity anomaly tends to get localised around the island as our only data source at shallow depths are the seismic channels in the *TRIS* station on Tristan da Cunha island and PP bouncing

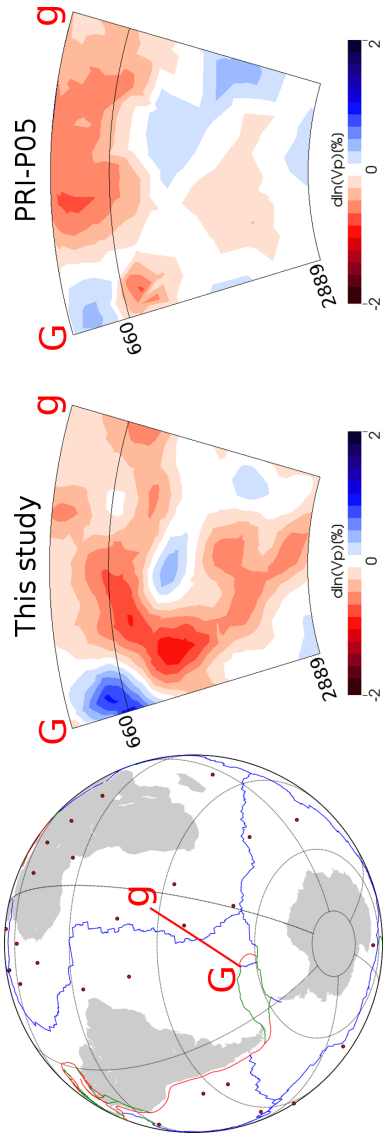

Figure 5.6: Whole mantle depth cross-sections of compressional velocity variations through our model and PRI-P05, in the vicinity of the Tristan da Cunha hotspot. The section is shown in the map (left). Although PRI-P05 shows low velocities in the upper and to some extent in the mid mantle, our model features a continuous low-velocity structure from the CMB (connected to the border of the African LLSVP) up to the surface. Colours indicate the compressional velocity perturbations, $dln(V_p)$, with respect to IASP91 background model. Red dots represent the global hotspot distribution according to Steinberger (2000).

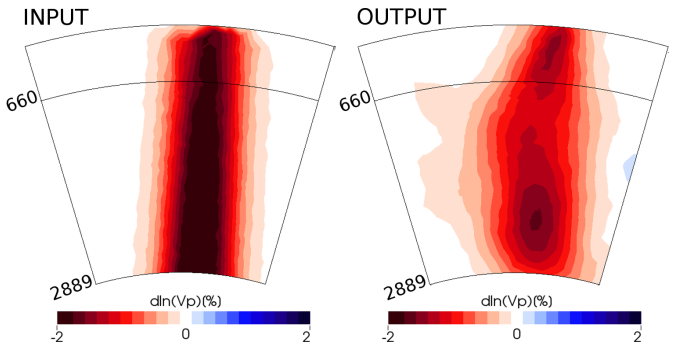

Figure 5.7: Resolution test. The input pattern is a 3-D cylinder with a Gaussian lateral velocity profile $dV_p/V_p = (dV_p/V_p)_{centre} exp(-r^2/w^2)$ with radius $w = 400$ km; centred at Tristan da Cunha island. The highest velocity perturbation $(dV_p/V_p)_{centre}$ in the centre of the cylinder is -3%. Left panel shows the input pattern, and right panel shows the output pattern retrieved by the inversion (using realistic regularisation and noise). A lateral smearing in the mid mantle is detectable which is due to the poor data coverage at this depth range. However, the smearing decreases in the lowermost and in the upper mantle. These results indicate that our inversion can resolve the long-wavelength features beneath Tristan da Cunha. However, imaging its structural complexities requires improvement in seismic observations, for example, considering other seismic phases, updating our data set with new events and more importantly including waveforms from new instrumentation (ocean-bottom seismographic experiments) in this region.

points. This mirrors one of the difficulties in imaging the mantle plumes: most presumed hotspots are located in the oceans with poor data coverage. New instrumentation, such as OBS (Ocean Bottom Seismometers, e.g., Laske et al. (2009); Barruol and Sigloch (2013)) and submarine MERMAIDS (Mobile Earthquake Recording in Marine Areas by Independent Divers, Simons et al. (2006)) will help to sharpen the mapped structures beneath volcanic islands and potentially any associated plumes.

5.3 Ancient subducted slabs

Various seismically fast structures have been detected throughout the mantle in global (P and S) seismic tomography models with an increasing consistency in their shapes and locations. The correlation between the imaged anomalies and the locations of paleo-subduction zones has suggested the subducted

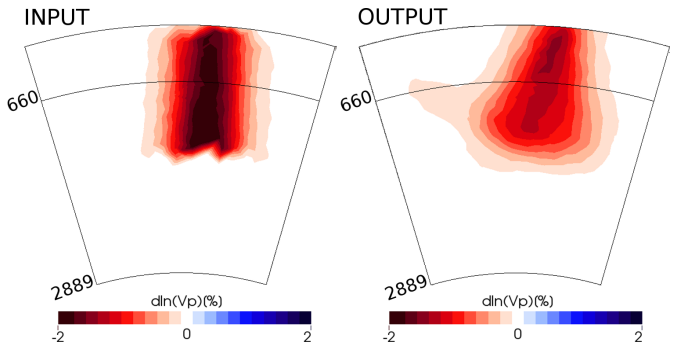

Figure 5.8: Resolution test. Like Fig. 5.7, except that the input column extends from the surface to the mid mantle (1500 km). This tests the effects of regularisation and data coverage on the vertical leakage. The recovered structure preserves the depth of the synthetic input model well. However, the anomalies in the mid mantle show lateral smearing due to the poor data coverage at these depths. This also causes amplitude decrease on the output anomalies. Note that at the shallow depths, the mapped structure is limited mainly to the vicinity of the island on which we have seismic stations. However, the multifrequency measurements have helped to constrain a wider region.

oceanic lithosphere as a possible origin for these high-velocity provinces (van der Hilst et al., 1997; Grand et al., 1997; Grand, 2002). Moreover, high-resolution (regional and global) seismic tomography studies have provided detailed maps of some of these anomalies from the surface to the lower mantle (Wortel and Spakman, 2000; Amaru, 2007; Li et al., 2008; Sigloch, 2008; Sigloch et al., 2008; Fukao et al., 2009; Sigloch, 2011; Obayashi et al., 2013). In these models, the slabs start to enter the mantle first as a thin structure with a thickness comparable with the oceanic lithosphere. They become several times thicker as they reach the transition zone. "Folding" of the slabs against the forces applied by higher-viscosity deeper mantle has been suggested as an explanation for the thickening of oceanic lithosphere (Griffiths and Turner, 1988). This hypothesis has been supported by several numerical (Gibert et al., 2012; Čížková and Bina, 2013) and laboratory experiments (Ribe et al., 2007). Consequently, wall-like "super-slabs" (Sigloch and Mihalynuk, 2013) created at the transition zone may sink vertically into the lower mantle since the only primary acting force is the gravity at these depths. Based on these observations, outlines of massive high-velocity piles near the CMB, (mapped out by global models), may relate to the ancient subducted slabs which probably reaches back $>$ 200 Ma. However, they have hardly

been explored because tomographic image resolution in the lower mantle is still limited.

A major effort in developing our global P wave model has focused on maximising the illumination of the lower third of the mantle to sharpen the previously imaged structures at this depth range. The results (Fig. 5.1) bear a striking resemblance to S wave models (e.g. Ritsema et al., 2011). At the same time, slabs at the base of the mantle and few hundred kilometres above the CMB appear as narrower, more linear belts. One example of this is the high-velocity anomaly beneath north and central America (Fig. 5.9, panels a and b).

Hung et al. (2005) imaged the lower mantle shear velocity structure beneath the Caribbean and surrounding areas by using a regional finite frequency technique. On long wavelength scales, their model showed a high-velocity anomaly that covers central America and reaches to the northwest of Colombia. Other seismological and tomographic studies have also detected the slab located below the Cocos plate and Central America (e.g. Thomas et al., 2004; Hutko et al., 2006; Kito et al., 2007; Amaru, 2007). Our model confirms these findings as shown in Fig. 5.9(a) and (b). Moreover, it agrees well with the model of Hung et al. (2005) on the seismically slow features under the northern part of south America. These have been interpreted as a localised region of low-velocity in D'' (Wysession et al., 2001; Fisher et al., 2003) or as a part of a cluster of low-velocity patches in the vicinity (Hung et al., 2005).

To assess the robustness of the imaged features, a resolution test was performed with the input model shown in Fig. 5.10(a) and Fig. 5.11(a). The retrieved structures using realistic regularisation and noise are shown at the CMB beneath America and western Pacific in Fig. 5.10(b) and Fig. 5.11(b), respectively. The input patterns are very well recovered in all relevant regions. Three-dimensional renderings of the output models, 400 km above the CMB, also show no significant lateral smearing (Fig. 5.10d and Fig. 5.11d).

Almost all global tomography models agree on a deep high-velocity anomaly beneath eastern Asia. This structure may be associated with the remnants of subducted slabs – Paleozoic/Mesozoic fossil slabs – accumulated in the deepest lower mantle (Sengör et al., 1993; Fukao et al., 1992; Van der Voo et al., 1999b). Our model features this huge pile under eastern Asia and the western Pacific that extends to the northern Pacific (Fig. 5.9c). To better illustrate these anomalies, only seismically fast structures from 2350-2850 km depth (500 km above the CMB) are rendered in Fig. 5.9(d). Visual inspection of the model a few hundred kilometres above the CMB indicates the presence of two distinct high-velocity structures: one starts from the northwest Pacific and reaches to the mid-eastern Pacific. The other extends from western to

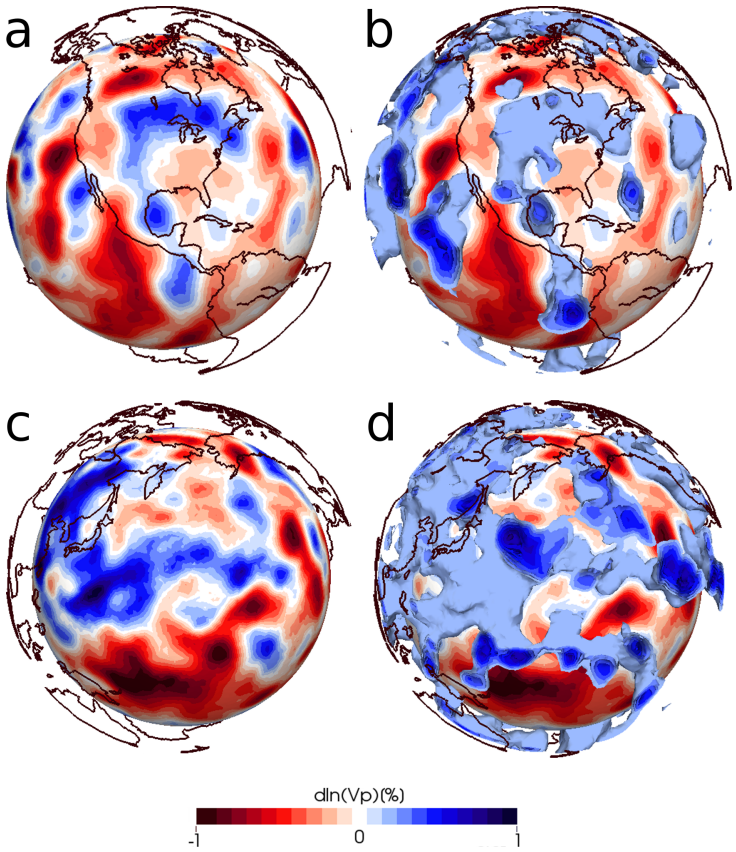

Figure 5.9: High velocity structures imaged by our model at the base of the mantle. Panels a and c show the structures at 2800 km depth beneath America and the northwestern Pacific, respectively. Panels b and d render the three-dimensional seismically fast anomalies 500 km above the CMB beneath America and the northwestern Pacific. The isosurface threshold is $0.2\% \leq dln(V_p) \leq 1.0\%$ in increments of 0.1%. Colours indicate the compressional velocity perturbations, $dln(V_p)$, with respect to IASP91 background model. Note that the continental outlines are at 500 km above the CMB.

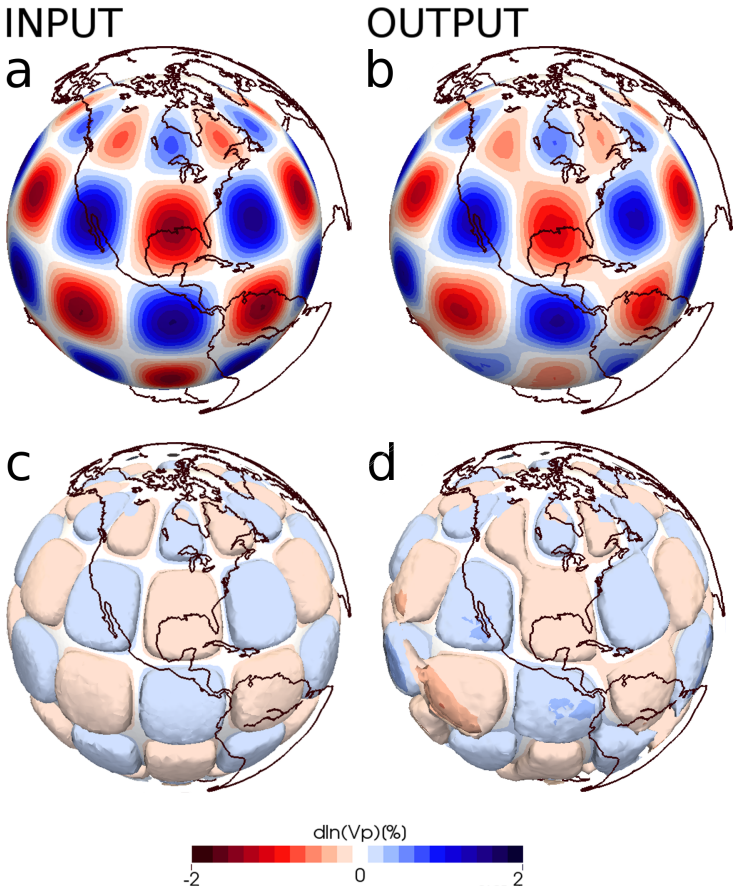

Figure 5.10: Resolution test. The input pattern is shown in panels a and c. In each block, the centre has the highest velocity perturbation of ±3%, and velocity profiles are extended laterally with a Gaussian function. Retrieved anomalies (using realistic regularisation and noise) are shown at the base of the mantle (panel b). A three-dimensional rendering of the output 400 km above the CMB is also presented to test the smearing of the recovered anomalies at these depths (panel d). The isosurface threshold in 3-D renderings is $-3.0\% \leq dln(V_p) \leq -0.2\%$ and $0.2\% \leq dln(V_p) \leq 3.0\%$ in increments of 0.1%. Colours indicate the compressional velocity perturbations, $dln(V_p)$, with respect to IASP91 background model. Note that the continental outlines are at 500 km above the CMB.

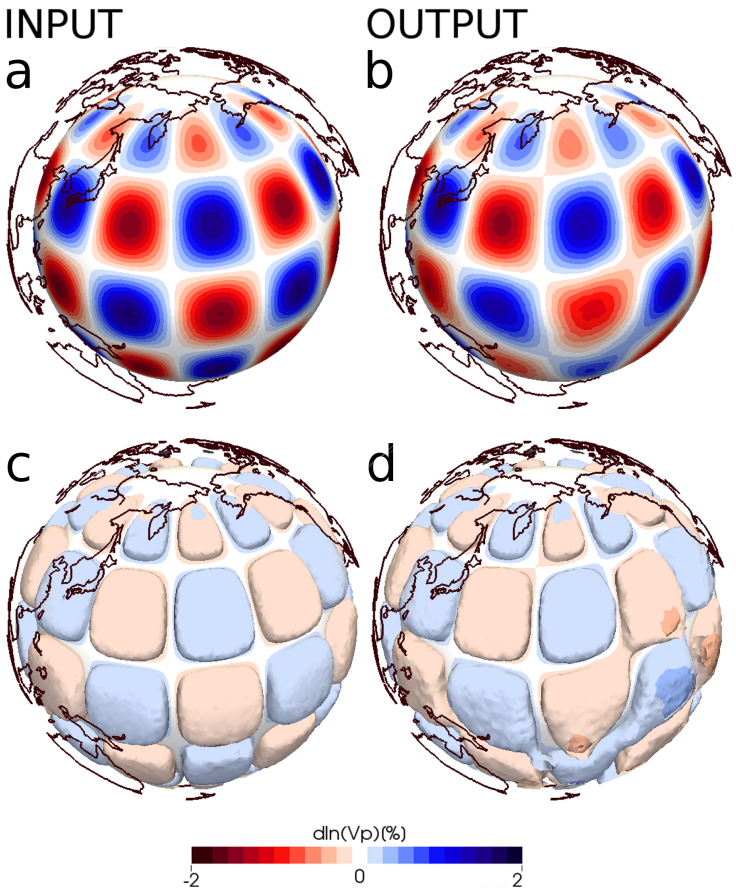

Figure 5.11: Resolution test. Like Fig. 5.10, except that the location is the western Pacific. The output patterns are very well resolved with an exception beneath southern Pacific due to the poor illumination in this region. Colours indicate the compressional velocity perturbations, $dln(V_p)$, with respect to IASP91 background model. Note that the continental outlines are at 500 km above the CMB.

Central Pacific. Our model also reveals extensive fast anomalies from the northwestern Pacific to eastern Eurasia. This structure is the largest body of high-velocity anomalies in almost all the existing global P models (Fukao et al., 2009), and they have been interpreted as the graveyard of ancient slabs in the northwestern Pacific.

There is a striking similarity between the locations of linearly elongated fast seismic velocities in D'' (e.g., America and eastern Asia) and the locations of paleo-subduction zones (Paleozoic Paleotrenches). This reinforces the idea that CMB may be the ultimate resting place of deep-diving subducted lithosphere (Wysession, 1996b) through a strong coupling between surface plate tectonics and the lower mantle. Based on these observations, images of ancient subducted slabs may help to better constrain the reconstruction of tectonic plate configurations. This "absolute plate motion reference frame" has already been used successfully in both regional (Van der Voo et al., 1999a,b; Hafkenscheid et al., 2006; Ren et al., 2007; Sigloch et al., 2008; Van der Meer et al., 2012; Sigloch and Mihalynuk, 2013) and global paleogeographic reconstructions (van der Meer et al., 2010). The results of modern tomography models will help to place tighter constraints on the current under-constrained tectonic models by incorporating this deep structural information, especially for the periods not recorded by the current seafloor.

5.4 Conclusion

A global multiple-frequency tomography model was used to infer the lower mantle structure and its relation to the shallower depths. The underlying P velocity model was obtained by a waveform-based tomography technique which systematically measures and models the frequency dependence of teleseismic body waves. The inclusion of core-sensitive Pdiff waves alongside teleseismic (P and PP) measurements greatly enhanced the illumination, particularly in the lower third of the mantle.

Mapped anomalies recovered major structural, lower-mantle heterogeneities known from existing global (P and S) mantle models: the African and Pacific LLSVPs and the large high-velocity provinces under eastern Asia and America. On intermediate wavelength scales, subdivisions of two LLSVPs were imaged. One example is a relatively small-scale but pronounced feature in the northern border of the Pacific LLSVP (southwest of Hawaii) consistent with local studies in this region. By tracing the low-velocity anomalies under Iceland and Tristan da Cunha, quasi-vertical continuous features from the CMB to the upper mantle were revealed. These provide tomographic evidence for the presence of deep-rooted mantle plumes beneath these islands.

Outlines of massive slabs under Asia and America at the CMB appeared as narrower, more linear belts compared to previous global models. The results show two distinct linearly elongated high-velocity provinces beneath the western Pacific. These may relate to the remnants of Paleozoic/Mesozoic subducted slabs still visible in the mantle. Our results also showed a huge pile of fast anomalies from the northwestern Pacific to eastern Eurasia, consistent with previous global tomographic models. The mantle provinces under America showed a seismically fast structure that covers north America and extends to the northwest of Colombia.

A Extended data

A.1 Afar

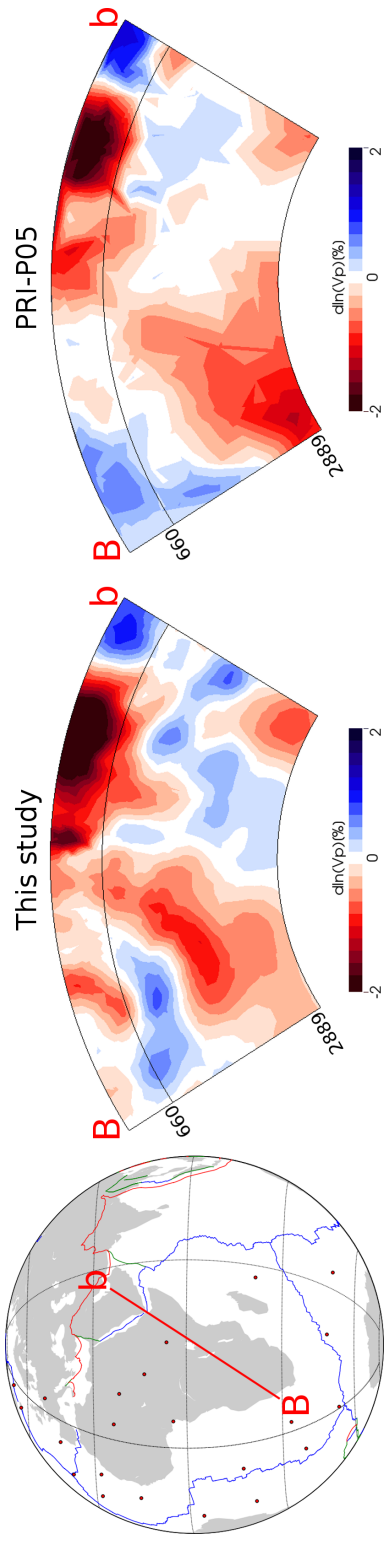

Figure A.1: Vertical cross-sections through our model and PRI-P05 (Montelli et al., 2006) in the mantle structure beneath the Afar hotspot. The section is shown in the map (left). Both models feature a continuous low-velocity structure from the CMB (connected to the African LLSVP) up to the surface. Colours indicate the compressional velocity perturbations, $dln(V_p)$, with respect to IASP91 background model. Red dots represent the global hotspot distribution according to Steinberger (2000).

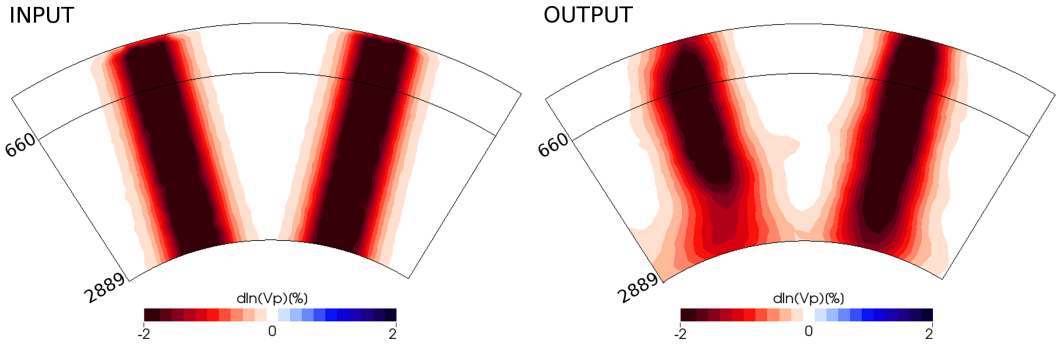

Figure A.2: Resolution test. Two 3-D cylinders with Gaussian lateral velocity profiles $dV_p/V_p = (dV_p/V_p)_{centre} exp(-r^2/w^2)$ and with radii $w = 400$ km are considered in the vicinity of the Afar hotspot. The highest velocity perturbation $(dV_p/V_p)_{centre}$ in the centre of each cylinder is -3%. Left panel shows the input pattern, and right panel shows the output pattern retrieved by the inversion (using realistic regularisation and noise). In both recovered columns, a lateral smearing in the lower mantle is detectable mirroring the poor Pdiff coverage under south Africa.

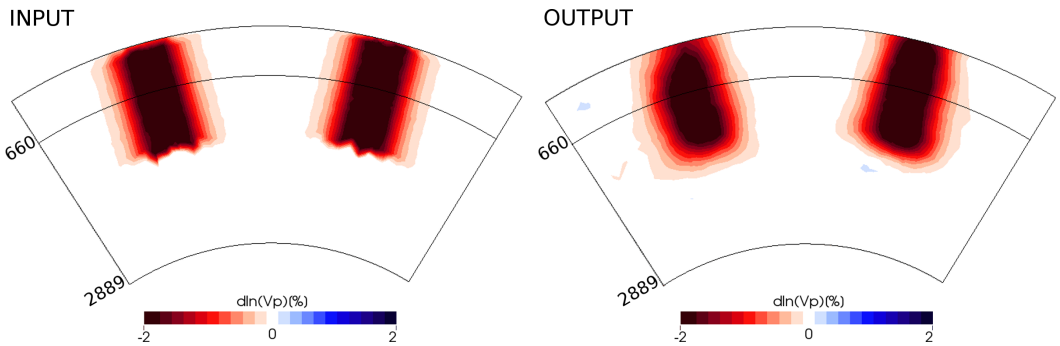

Figure A.3: Resolution test. Like Fig. A.2, except that the input cylinders extend from the surface to the mid mantle (1500 km). The output column preserves the depth of the input model well with no significant vertical leakage. This suggests that the observed extension of the model to the CMB was required by our traveltime observations (rather than caused by inversion artefacts).

6

Conclusions & Outlook

The scope of this thesis was to combine large seismological data sets with broad-band waveform modelling and multiple-frequency inversion technique to map mantle structure in all depths. To this end, we designed and implemented an efficient processing strategy called as "No Data Left Behind". A major effort in technical developments of this study was focused on delivering codes and solutions, each serves as one processing block, to this framework. This includes a fully automatic software toolbox for query, retrieval, processing and management of seismological data sets. This development led to a free, open-source community software *obspyDMT* that is now being used by several working groups (e.g., Poli and Prieto, 2014; Hillers et al., 2014).

A measurement technique was developed to extract multifrequency observables (amplitude and traveltime) from arbitrary seismic phases, including complex core-diffracted waves. In this methodology, synthetic seismograms are computed by semi-analytical wave propagation through a spherically symmetric earth model, to 1 Hz dominant frequency. We scaled and automated this technique to process the voluminous waveform data of $\approx$ 2000 earthquakes in our archive. This resulted in one of the largest core-diffracted P wave traveltime collections so far with a total of 479,559 traveltimes in frequency passbands ranging from 30.0 to 2.7 s dominant period. We showed that the strong observed dispersion in multifrequency Pdiff measurements is partly due to diffraction around the core and partly caused by finite-frequency effects in a heterogeneous earth. These significant imprints of the

3-D lowermost mantle heterogeneities were then used for a global waveform inversion.

An inversion framework with data-adaptive parameterisation and locally-adjusted regularisation was developed to accurately map the information of this data set onto the desired model parameters. We showed that Pdiff measurements can be embedded seamlessly into a global teleseismic P and PP wave inversion by using finite-frequency sensitivity kernels. This way, a single-iteration matrix inversion, starting from a spherically symmetric reference model, yielded highly-resolved, multi-scale tomographic images of the whole-mantle. Sharp outlines of several subduction systems (e.g., Tethyan, Aegean and Farallon slabs) and uprising mantle plumes (e.g., Iceland, Afar and Tristan da Cunha) were showed and discussed. Moreover, we reported the structural findings revealed by our model, from geometries of slab complexes and subdivisions of Large Low Shear Velocity Provinces at the root of the mantle to tomographic evidence to support the existence of deep-mantle plumes beneath Iceland and Tristan da Cunha.

The multi-scale mantle structures imaged by modern, high-resolution models of this kind will help to re-evaluate the discrimination between thermal and chemical anomalies and to assess more precisely the fate of slabs and morphological characteristics of mantle plumes. For geological and paleogeographic interpretation, outlines of the imaged ancient subducted slabs may place tighter constraints on the current tectonic models by incorporating deep structural information, that is, tectonic plate reconstruction with the slab constraints. By providing high-resolution global models, modern tomographic techniques can push geodynamical modellings towards more "realistic" convection patterns in the mantle and consequently, improve our understanding of geological and geodynamical processes driving our planet.

Theoretical and technical aspects of the present work can be extended in various ways. In the following, we will give an outlook on two possible future developments: extending the data archive with recent earthquakes and novel seismic phases, and calculation of "true" sensitivity kernels.

Future Developments

Massive data sets for waveform tomography

Source and receiver coverage used in this study reflects our "No Data Left Behind" philosophy, in that we considered every event of magnitude $m_b \geq 5.8$ that occurred between 1999 and 2010 – plus many earlier or smaller events if they occurred in unusual locations. One way of extending the current

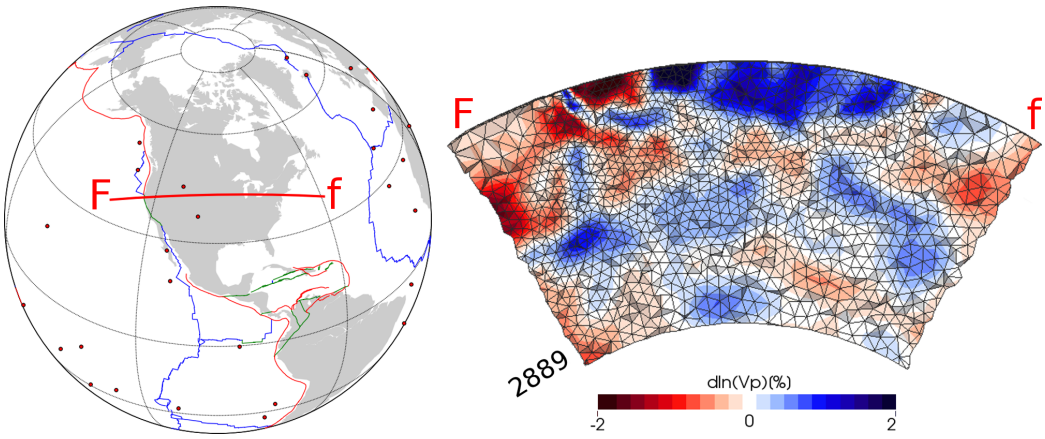

Figure 6.1: Vertical cross-section through our model in the North American mantle from the surface down to the CMB (see Fig. 4.22 in Chapter 4). The data-adaptive parameterisation technique developed in this study has correctly accounted for the varying density of the data coverage in this region. The tetrahedra facet length differs significantly beneath North America and adjacent Pacific. Inclusion of new data sets, both in terms of quantity and type, should help to improve the global tomographic resolution.

study is to update this data set with recent earthquakes recorded by land stations, ocean bottom seismometers (OBS) and submarine MERMAIDS (Simons et al., 2006).

Fig. 6.1 shows a whole-mantle-depth cross section through our model beneath North America (similar to Fig. 4.22 in Chapter 4). Triangles in this figure are one of the triangular faces of the tetrahedrons used for parameterisation. Our data-adaptive parameterisation technique has correctly accounted for the uneven data coverage in this region. Sizes of tetrahedrons are decreased beneath the densely sampled North America. On the other hand, larger tetrahedrons are considered in the adjacent Pacific with poor data coverage. Tomographic resolution in regions with sub-optimal illumination remains limited by the long wavelengths. Inclusion of new source-receiver pairs to our data archive can help to enhance the coverage and consequently, to increase the resolution. Examples for data sets that can considerably improve our current global coverage are: onshore/offshore seismic deployments by Cascadia initiative (Toomey et al., 2014; Sumy et al., 2015) along the Cascadia subduction zone, RHUM-RUM land and OBS stations which cover an area of 2000 $\times$ 2000 km^2 around the La Réunion island (Barruol and Sigloch, 2013; Stähler et al., 2016), and TRISTAN land and OBS stations

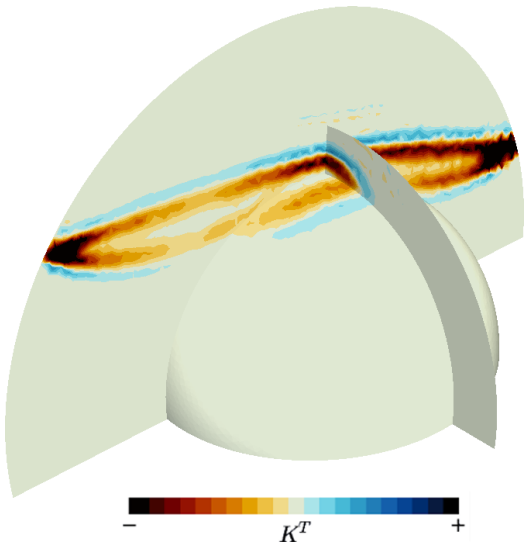

Figure 6.2: Sensitivity kernel of a Pdiff wave recorded at an epicentral distance of 120 °. The kernel is calculated in a 21 s log-Gabor filter and projected onto a global tetrahedron inversion mesh. This "true", finite-frequency sensitivity kernel resembles a spatially extended banana in the mantle, but flattens elliptically on top of the CMB due to diffraction.

surrounding the Tristan da Cunha island in an area of $500 \times 500\ km^2$ (Jegen et al., 2015), to name a few.

There should be significant room for improvement in tomographic resolutions by using not only more data but also novel data. In this work, we jointly inverted multifrequency measurements of teleseismic (P, PP) and core-diffracted P waves. Our tool-set for finite-frequency (amplitude and traveltime) measurements can be seamlessly applied to other seismic phases as well. For inversion of such data in a linearized optimisation problem, corresponding sensitivity kernels should be calculated. This will be discussed in the following section.

Broad-band sensitivity kernels

The method of choice to calculate 3-D sensitivity kernels throughout this study was the efficient but approximative algorithm of Dahlen et al. (2000). A natural extension of this work would be to use the spatiotemporal evolution of 3-D wavefields to calculate "true" sensitivities of any part of a seismogram (Fig. 6.2). This can considerably reduce modelling mismatches inherent in using approximate sensitivities.

Facilitated by AxiSEM, calculation of accurate 3-D Born-Fréchet sensitivity kernels across the entire usable frequencies is now feasible. MC Kernel, implementation of this method, uses full forward and backward wavefields to calculate the kernels which are able to account for seismic sensitivities of arbitrary resolutions and observables (Stähler et al., 2016). This software works in an inversion-grid-centred fashion: kernels are computed on irregular, adapted inversion grids. A Monte-Carlo integration method is employed to project kernel values onto each basis function. This way, the desired precision of the kernel estimation can be controlled with no prior assumption on the kernel shape (Stähler et al., 2016). Fig. 6.2 shows the sensitivity kernel of a Pdiff wave computed with this method.

Such (in particular differential) time-space sensitivity kernels can also form a basis to quantitatively optimise data selection, that is, identifying those parts of a seismogram that are most sensitive to the structures of interest. We hope and expect that this strategy combined with the novel data sets suggested in the previous section lead to a sea change in the resolution of tomography models in the near future.

Bibliography

Afanasiev, M., Peter, D., Sager, K., Simutė, S., Ermert, L., Krischer, L., and Fichtner, A., *Foundations for a multiscale collaborative Earth model*, Geophysical Journal International, 204(1):39–58, 2016. (cited on page 7)

Aki, K. and Richards, P. G., *Quantitative Seismology*, Geology (University Science Books).: Seismology. University Science Books, 2002, ISBN 9780935702965. (cited on page 45, 46)

Al-Attar, D. and Woodhouse, J. H., *Calculation of seismic displacement fields in self-gravitating earth models–applications of minors vectors and symplectic structure*, Geophys. J. Int., 175(3):1176–1208, 2008, doi: 10.1111/j.1365-246X.2008.03961.x. (cited on page 42, 43, 44, 48, 49, 59)

Amaru, M., *Global travel time tomography with 3-D reference models*, Geologica Ultraiectina, 274, 2007. (cited on page 4, 123, 124)

Anderson, D. L., *Scoring hotspots: The plume and plate paradigms*, Geological Society of America Special Papers, 388:31–54, 2005. (cited on page 115)

Auer, L., Boschi, L., Becker, T., Nissen-Meyer, T., and Giardini, D., *Savani: A variable resolution whole-mantle model of anisotropic shear velocity variations based on multiple data sets*, Journal of Geophysical Research: Solid Earth, 119(4):3006–3034, 2014. (cited on page 4, 7, 8, 113)

Backus, G. and Gilbert, F., *The resolving power of gross earth data*, Geophysical Journal International, 16(2):169–205, 1968. (cited on page 3)

Backus, G. and Gilbert, F., *Uniqueness in the inversion of inaccurate gross earth data*, Phil. Trans. R. Soc. A: Mathematical, Physical and Engineering Sciences, 266(1173):123–192, 1970. (cited on page 3)

Backus, G. E. and Gilbert, J., *Numerical applications of a formalism for geophysical inverse problems*, Geophysical Journal International, 13(1-3): 247–276, 1967. (cited on page 3)

Barber, C. B., Dobkin, D. P., and Huhdanpaa, H., *The quickhull algorithm for convex hulls*, ACM Transactions on Mathematical Software, 22(4): 469–483, 1996. (cited on page 89)

Barruol, G. and Sigloch, K., *Investigating La Réunion hot spot from crust to core*, Eos, Transactions American Geophysical Union, 94(23):205–207, 2013. (cited on page 25, 122, 135)

Bassin, C., Laske, G., and Masters, G., *The Current Limits of Resolution for Surface Wave Tomography in North America*, Eos, 81, 2000. (cited on page 57, 63, 84)

Beyreuther, M., Barsch, R., Krischer, L., Megies, T., Behr, Y., and Wassermann, J., *ObsPy: A Python Toolbox for Seismology*, SRL, 81(3):530–533, may 2010. (cited on page 21)

Bijwaard, H. and Spakman, W., *Tomographic evidence for a narrow whole mantle plume below Iceland*, Earth and Planetary Science Letters, 166(3): 121–126, 1999. (cited on page 3, 117)

Bijwaard, H., Spakman, W., and Engdahl, E. R., *Closing the gap between regional and global travel time tomography*, Journal of Geophysical Research: Solid Earth (1978–2012), 103(B12):30055–30078, 1998. (cited on page 3, 4, 75)

Boschi, L. and Dziewonski, A. M., *Whole Earth tomography from delay times of P, PcP, and PKP phases: Lateral heterogeneities in the outer core or radial anisotropy in the mantle?*, Journal of Geophysical Research: Solid Earth (1978–2012), 105(B6):13675–13696, 2000. (cited on page 3, 4, 75)

Bozdag, E., Lefebvre, M., Lei, W., Peter, D., Smith, J., Komatitsch, D., and Tromp, J., Global Adjoint Tomography, In *EGU General Assembly Conference Abstracts*, volume 17, page 7640, 2015. (cited on page 8)

Chapman, C., *A new method for computing synthetic seismograms*, Geophys. J. Roy. Astr. Soc., 54:481–518, 1978. (cited on page 48)

Čížková, H. and Bina, C. R., *Effects of mantle and subduction-interface rheologies on slab stagnation and trench rollback*, Earth and Planetary Science Letters, 379:95–103, 2013. (cited on page 123)

Colombi, A., Nissen-Meyer, T., Boschi, L., and Giardini, D., *Seismic waveform sensitivity to global boundary topography*, Geophysical Journal International, 191(2):832–848, 2012, doi: 10.1111/j.1365-246X.2012.05660.x. (cited on page 113)

Colombi, A., Nissen-Meyer, T., Boschi, L., and Giardini, D., *Seismic waveform inversion for core-mantle boundary topography*, Geophysical Journal International, page 10.1093/gji/ggu112, 2014. (cited on page 113)

Cottaar, S. and Romanowicz, B., *An unsually large ULVZ at the base of the mantle near Hawaii*, Earth and Planetary Science Letters, 355:213–222, 2012. (cited on page 71, 104, 115)

Courtillot, V., Davaille, A., Besse, J., and Stock, J., *Three distinct types of hotspots in the Earth's mantle*, Earth and Planetary Science Letters, 205 (3):295–308, 2003. (cited on page 120)

Dahlen, F. A. and Baig, A., *Fréchet kernels for body wave amplitudes*, Geophys. J. Int., 150:440–466, 2002. (cited on page 9, 75)

Dahlen, F. A., Hung, S.-H., and Nolet, G., *Fréchet kernels for finite-frequency traveltimes-I. Theory*, Geophysical Journal International, 141(1):157–174, 2000. (cited on page 5, 9, 51, 75, 77, 86, 87, 113, 136)

Dziewonski, A. M., *Mapping the lower mantle: determination of lateral heterogeneity in P velocity up to degree and order 6*, Journal of Geophysical Research: Solid Earth, 89(B7):5929–5952, 1984. (cited on page 3)

Dziewonski, A. and Anderson, D., *Preliminary reference Earth model*, Phys. Earth Planet. Inter., 25:297–356, 1981. (cited on page 2, 47, 76)

Dziewonski, A., Hager, B., and O'Connell, R., *Large-scale heterogeneities in the lower mantle*, J. Geophys. Res., 82:239–255, 1977. (cited on page 3, 4, 8, 74, 113)

Engdahl, E. R., van der Hilst, R., and Buland, R., *Global teleseismic earthquake relocation with improved travel times and procedures for depth determination*, Bulletin of the Seismological Society of America, 88(3):722–743, 1998. (cited on page 81)

FDSN, FDSN StationXML Schema, 2015, [Online; accessed 27-March-2015]. (cited on page 29)

Fichtner, A. and Igel, H., *Efficient numerical surface wave propagation through the optimization of discrete crustal models - a technique based on non-linear dispersion curve matching (DCM)*, Geophys. J. Int., 173(2): 519–533, may 2008. (cited on page 6)

Fichtner, A. and Villaseñor, A., *Crust and upper mantle of the western Mediterranean–Constraints from full-waveform inversion*, Earth and Planetary Science Letters, 428:52–62, 2015. (cited on page 8)

Fichtner, A., Kennett, B. L. N., Igel, H., and Bunge, H.-P., *Theoretical background for continental and global scale full-waveform inversion in the time-frequency domain*, Geophys. J. Int., 175(2):665–685, nov 2008. (cited on page 5)

Fichtner, A., Igel, H., Bunge, H.-P., and Kennett, B. L. N., *Simulation and inversion of seismic wave propagation on continental scales based on a spectral-element method*, Journal of Numerical Analysis, Industrial and Applied Mathematics, 4(1-2):11–22, 2009a. (cited on page 48)

Fichtner, A., Kennett, B. L. N., Igel, H., and Bunge, H.-P., *Full waveform tomography for upper-mantle structure in the Australasian region using adjoint methods*, Geophys. J. Int., 179(3):1703–1725, 2009b. (cited on page 5, 8)

Fisher, J. L., Wysession, M. E., and Fischer, K. M., *Small-scale lateral variations in D attenuation and velocity structure*, Geophysical research letters, 30(8), 2003. (cited on page 124)

French, S. W. and Romanowicz, B., *Broad plumes rooted at the base of the Earth's mantle beneath major hotspots*, Nature, 525(7567):95–99, 2015. (cited on page 3, 75, 115)

French, S. and Romanowicz, B., *Whole-mantle radially anisotropic shear velocity structure from spectral-element waveform tomography*, Geophysical Journal International, 199(3):1303–1327, 2014. (cited on page 7, 8)

Friederich, W. and Dalkolmo, J., *Complete synthetic seismograms for a spherically symmetric Earth by a numerical computation of the Green's function in the frequency domain*, Geophys. J. Int., 122:537–550, 1995. (cited on page 48)

Fuchs, K. and Müller, G., *Computation of synthetic seismograms with the reflectivity method and comparison with observations*, Geophys. J. Roy. Astr. Soc., 23:417–433, 1971. (cited on page 49)

Fukao, Y., Obayashi, M., Inoue, H., and Nenbai, M., *Subducting slabs stagnant in the mantle transition zone*, Journal of Geophysical Research: Solid Earth, 97(B4):4809–4822, 1992. (cited on page 124)

Fukao, Y., Obayashi, M., and Nakakuki, T., *Stagnant slab: a review*, Annual Review of Earth and Planetary Sciences, 37:19–46, 2009. (cited on page 123, 128)

George Helffrich, J. W. and Bastow, I., *The Seismic Analysis Code*, Cambridge University Press, 2013. (cited on page 23)

Gibert, G., Gerbault, M., Hassani, R., and Tric, E., *Dependency of slab geometry on absolute velocities and conditions for cyclicity: insights from numerical modelling*, Geophysical Journal International, 189(2):747–760, 2012. (cited on page 123)

Grand, S., van der Hilst, R., and Widiyantoro, S., *Global seismic tomography: A snapshot of mantle convection in the Earth*, GSA Today, 7:1–7, 1997. (cited on page 3, 4, 74, 123)

Grand, S. P., *Mantle shear–wave tomography and the fate of subducted slabs*, Phil. Trans. R. Soc. A: Mathematical, Physical and Engineering Sciences, 360(1800):2475–2491, 2002. (cited on page 41, 42, 53, 103, 104, 112, 113, 123)

Griffiths, R. and Turner, J., *Folding of viscous plumes impinging on a density or viscosity interface*, Geophysical Journal International, 95(2):397–419, 1988. (cited on page 123)

Groos, J., *Broadband seismic noise: classification and Green's function estimation*, PhD thesis, Karlsruher Instituts für Technologie, 2010. (cited on page 29, 30, 31)

Gutenberg, B., *Über die Konstitution des Erdinnern, erschlossen aus Erdbebenbeobachtungen*, Phys. Zeitschrift, 14:1217–1218, 1913. (cited on page 2)

Hafkenscheid, E., Wortel, M. J. R., and Spakman, W., *Subduction history of the Tethyan region derived from seismic tomography and tectonic reconstructions*, Journal of Geophysical Research: Solid Earth (1978–2012), 111 (B8), 2006. (cited on page 41, 104, 128)

Hillers, G., Campillo, M., Ben-Zion, Y., and Roux, P., *Seismic fault zone trapped noise*, Journal of Geophysical Research: Solid Earth, 119(7):5786–5799, 2014. (cited on page 133)

Hosseini, K., Sigloch, K., and Stähler, S., *Finite Frequency Measurements of Conventional and Core-diffracted P-waves (P and Pdiff)*, AGU Fall Meeting Abstracts, 1:4450, 2014. (cited on page 18)

Hosseini, K. and Sigloch, K., *Multifrequency measurements of core-diffracted P waves (Pdiff) for global waveform tomography*, Geophysical Journal International, 203(1):506–521, 2015, doi: 10.1093/gji/ggv298. (cited on page 9, 12, 18, 33, 75, 76, 79, 82, 112)

Hosseini-zad, K., Stähler, S. C., Sigloch, K., and Scheingraber, C., *"No Data Left Behind": Efficient processing of large datasets for waveform tomography and Bayesian source inversion*, in EGU General Assembly 2012, held 2012 April 22–27 in Vienna, Austria., p. 4157, 2012. (cited on page 10, 42, 80)

Houser, C., Masters, G., Shearer, P., and Laske, G., *Shear and compressional velocity models of the mantle from cluster analysis of long-period waveforms*, Geophys. J. Int., 174:195–212, 2008. (cited on page 70)

Hung, S.-H., Dahlen, F. A., , and Nolet, G., *Fréchet kernels for finite-frequency traveltimes—II. Examples*, Geophys. J. Int., 141:175–203, 2000. (cited on page 5, 9, 75, 86, 113)

Hung, S.-H., Shen, Y., and Chiao, L.-Y., *Imaging seismic velocity structure beneath the Iceland hot spot: A finite frequency approach*, Journal of Geophysical Research: Solid Earth (1978–2012), 109(B8), 2004. (cited on page 75, 117)

Hung, S.-H., Garnero, E. J., Chiao, L.-Y., Kuo, B.-Y., and Lay, T., *Finite frequency tomography of D shear velocity heterogeneity beneath the Caribbean*, Journal of Geophysical Research: Solid Earth, 110(B7), 2005. (cited on page 124)

Hunter, J. D., *Matplotlib: A 2D graphics environment*, Computing In Science & Engineering, 9(3):90–95, 2007. (cited on page 21)

Hutko, A., Lay, T., Garnero, E., and Revenaugh, J., *Seismic detection of folded, subducted lithosphere at the core-mantle boundary*, Nature, 441: 333–336, 2006. (cited on page 112, 124)

Jackson, D. D., *Interpretation of inaccurate, insufficient and inconsistent data*, Geophysical Journal International, 28(2):97–109, 1972. (cited on page 3)

Jeffreys, H. and Bullen, K. E., *Seismological Tables*, British Association for the Advancement of Science, London, 1940. (cited on page 2)

Jeffreys, H., *The Rigidity of the Earth's Central Core*, Geophysical Supplements to the Monthly Notices of the Royal Astronomical Society, 1(7): 371–383, 1926. (cited on page 2)

Jegen, M., Geissler, W., Maia, M., Baba, K., and Kirk, H., *TRISTAN: Electromagnetic, gravimetric and seismic measurements to investigate the Tristan da Cunha hot spot and its role in the opening of the South-Atlantic-Cruise No. MSM20/2, January 17-February 15, 2012, Walvis Bay (Namibia)–Recife (Brazil)*, 2015. (cited on page 136)

Kàrason, H. and Van der Hilst, R., *Tomographic imaging of the lowermost mantle with differential times of refracted and diffracted core phases (PKP, Pdiff)*, J. Geophys. Res., 106:6569–6587, 2001. (cited on page 3, 4, 41, 71, 75, 92)

Käufl, P., Fichtner, A., and Igel, H., *Probabilistic full waveform inversion based on tectonic regionalization-development and application to the Australian upper mantle*, Geophysical Journal International, page ggs131, 2013. (cited on page 6)

Kennett, B. L. N. and Gudmundsson, O., *Ellipticity corrections for seismic phases*, Geophysical Journal International, 127(1):40–48, 1996, ISSN 1365-246X, doi: 10.1111/j.1365-246X.1996.tb01533.x. (cited on page 58, 84)

Kennett, B. and Engdahl, E., *Traveltimes for global earthquake location and phase identification*, Geophys. J. Int., 105:429–465, 1991. (cited on page 2, 47, 76)

Kennett, B., Engdahl, E., and Buland, R., *Constraints on seismic velocities in the Earth from traveltimes*, Geophys. J. Int., 122:108–124, 1995. (cited on page 2)

Kennett, B., Widiyantoro, S., and Van Der Hilst, R., *Joint seismic tomography for bulk-sound and shear wavespeed*, J. geophys. Res, 103(12):469–12, 1998. (cited on page 3, 4, 75)

Kito, T., Rost, S., Thomas, C., and Garnero, E. J., *New insights into the P-and S-wave velocity structure of the D" discontinuity beneath the Cocos plate*, Geophysical Journal International, 169(2):631–645, 2007. (cited on page 112, 124)

Knopoff, L. and Gilbert, F., *Diffraction of elastic waves by the core of the earth*, Bulletin of the Seismological Society of America, 51(1):35–49, 1961. (cited on page 43)

Koelemeijer, P., Ritsema, J., Deuss, A., and van Heijst, H.-J., *SP12RTS: a degree-12 model of shear- and compressional-wave velocity for Earth's mantle*, Geophysical Journal International, 204(2):1024–1039, 2016, doi: 10.1093/gji/ggv481. (cited on page 4, 75, 113)

Koelemeijer, P., Deuss, A., and Ritsema, J., *Observations of core-mantle boundary Stoneley modes*, Geophys. Res. Lett., 40:2557–2561, 2013. (cited on page 71)

Komatitsch, D. and Tromp, J., *Spectral-element simulations of global seismic wave propagation—I. Validation*, Geophys. J. Int., 149:390–412, 2002a. (cited on page 42, 48)

Krischer, L., Megies, T., Barsch, R., Beyreuther, M., Lecocq, T., Caudron, C., and Wassermann, J., *ObsPy: A Bridge for Seismology into the Scientific Python Ecosystem*, Computational Science & Discovery, 8(1):014003, 2015, doi: 10.1088/1749-4699/8/1/014003. (cited on page 21)

Kustowski, B., Ekström, G., and Dziewonski, A. M., *Anisotropic shear-wave velocity structure of the Earth's mantle: a global model*, Journal of Geophysical Research: Solid Earth, 113(B6):2156–2202, 2008, doi: 10.1029/2007JB005169. (cited on page 70)

Laske, G., Collins, J. A., Wolfe, C. J., Solomon, S. C., Detrick, R. S., Orcutt, J. A., Bercovici, D., and Hauri, E. H., *Probing the Hawaiian hot spot with new broadband ocean bottom instruments*, Eos, Transactions American Geophysical Union, 90(41):362–363, 2009. (cited on page 122)

Lay, T., *Structure of the core-mantle transition zone*, Eos, Transactions American Geophysical Union, 70(4):49–59, 1989. (cited on page 112)

Lehmann, I., *P', Publ*, Bur. Centr. Seism. Internat. Serie A, 14:87–115, 1936. (cited on page 2)

Lei, J. and Zhao, D., *Global P-wave tomography: On the effect of various mantle and core phases*, Physics of the Earth and Planetary Interiors, 154 (1):44–69, 2006. (cited on page 4, 75)

Lekić, V. and Romanowicz, B., *Inferring upper-mantle structure by full waveform tomography with the spectral element method*, Geophysical Journal International, 185(2):799–831, 2011. (cited on page 8)

Li, C., van der Hilst, R. D., Engdahl, E. R., and Burdick, S., *A new global model for P wave speed variations in Earth's mantle*, Geochemistry, Geophysics, Geosystems, 9(5), 2008. (cited on page 4, 40, 41, 75, 101, 103, 104, 112, 113, 123)

Li, X.-D. and Romanowicz, B., *Global mantle shear velocity model developed using nonlinear asymptotic coupling theory*, Journal of Geophysical Research: Solid Earth, 101(B10):22245–22272, 1996. (cited on page 5)

Liu, Q. and Tromp, J., *Finite-frequency sensitivity kernels for global seismic wave propagation based upon adjoint methods*, Geophys. J. Int., 174:265–286, 2008. (cited on page 5, 40)

Loper, D. E. and Lay, T., *The core-mantle boundary region*, Journal of Geophysical Research: Solid Earth, 100(B4):6397–6420, 1995. (cited on page 112)

Marquering, H., Nolet, G., and Dahlen, F. A., *Three-dimensional waveform sensitivity kernels*, Geophys. J. Int., 132:521–534, 1998. (cited on page 5, 9, 75, 113)

Masters, G., Laske, G., Bolton, H., and Dziewonski, A., *The relative behavior of shear velocity, bulk sound speed, and compressional velocity in the mantle: implications for chemical and thermal structure*, Earth's Deep Interior: Mineral Physics and Tomography from the Atomic to the Global Scale, pages 63–87, 2000. (cited on page 40, 42, 53, 103, 112, 113)

Megies, T., Beyreuther, M., Barsch, R., Krischer, L., and Wassermann, J., *ObsPy - What Can It Do for Data Centers and Observatories?*, Annals Of Geophysics, 54(1):47–58, apr 2011, doi: 10.4401/ag-4838. (cited on page 21)

Mégnin, C. and Romanowicz, B., *The three-dimensional shear velocity structure of the mantle from the inversion of body, surface and higher-mode waveforms*, Geophys. J. Int., 143(3):709–728, 2000. (cited on page 41, 42, 53, 70, 103, 112, 113)

Mercerat, E. D. and Nolet, G., *On the linearity of cross-correlation delay times in finite-frequency tomography*, Geophysical Journal International, 192(2):681–687, 2013. (cited on page 7, 51)

Mohorovičić, A., *Earthquake of 8 October 1909 (Potres od 8. X 1909; Das Beben vom 8. X. 1909)*, Yearly Report of the Zagreb Meteorological Observatory for the Year, 1909. (cited on page 2)

Montelli, R., Nolet, G., Masters, G., Dahlen, F., and Hung, S.-H., *Global P and PP traveltime tomography: rays versus waves*, Geophysical Journal International, 158(2):637–654, 2004a. (cited on page 86)

Montelli, R., Nolet, G., Dahlen, F. A., Masters, G., Engdahl, E. R., and Hung, S.-H., *Finite-frequency tomography reveals a variety of plumes in the mantle*, Science, pages 338–343, 2004b. (cited on page 3, 5, 9, 75, 101, 115)

Montelli, R., Nolet, G., Dahlen, F. A., and Masters, G., *A catalogue of deep mantle plumes: New results from finite-frequency tomography*, Geochemistry, Geophysics, Geosystems, 7(11), 2006. (cited on page 8, 42, 53, 101, 103, 106, 108, 112, 113, 117, 120, 131)

Morgan, W. J., *Convection plumes in the lower mantle*, Nature, 230:42–43, 1971. (cited on page 115)

Morgan, W. J., *Deep mantle convection plumes and plate motions*, AAPG bulletin, 56(2):203–213, 1972. (cited on page 120)

Morozov, I. B. and Pavlis, G. L., *Management of large seismic datasets: I. Automated building and updating using BREQ_FAST and NetDC*, Seismol. Res. Lett., 82(2):211–221, 2011a. (cited on page 19)

Morozov, I. B. and Pavlis, G. L., *Management of large seismic datasets: II. Data center-type operation*, Seismol. Res. Lett., 82(2):222–226, 2011b. (cited on page 19)

Mosca, I., Cobden, L., Deuss, A., Ritsema, J., and Trampert, J., *Seismic and mineralogical structures of the lower mantle from probabilistic tomography*, Journal of Geophysical Research: Solid Earth, 117(B6), 2012. (cited on page 6)

Nissen-Meyer, T., Dahlen, F. A., and Fournier, A., *Spherical-earth Fréchet sensitivity kernels*, Geophys. J. Int., 168:1051–1066, 2007. (cited on page 5, 48)

Nissen-Meyer, T., van Driel, M., Stähler, S., Hosseini, K., Hempel, S., Auer, L., Colombi, A., and Fournier, A., *AxiSEM: broadband 3-D seismic wavefields in axisymmetric media*, Solid Earth, 5(1):425–445, 2014. (cited on page 33, 42, 48, 49)

Nolet, G., *A Breviary of Seismic Tomography: Imaging the Interior of the Earth and the Sun*, Cambridge University Press, Cambridge, 2008. (cited on page 3, 84)

Nolet, G., *Solving or resolving inadequate and noisy tomographic systems*, Journal of computational physics, 61(3):463–482, 1985. (cited on page 95)

Nolet, G. and Dahlen, F. A., *Wave front healing and the evolution of seismic delay times*, Journal of Geophysical Research, 105(19):043–19, 2000. (cited on page 53)

Nolet, G. and Montelli, R., *Optimal parametrization of tomographic models*, Geophys.J.Int., 161:365–372, 2005. (cited on page 7, 89)

Obayashi, M. and Fukao, Y., *P and PcP travel time tomography for the core-mantle boundary*, Journal of Geophysical Research: Solid Earth (1978–2012), 102(B8):17825–17841, 1997. (cited on page 3, 4, 75)

Obayashi, M., Yoshimitsu, J., Nolet, G., Fukao, Y., Shiobara, H., Sugioka, H., Miyamachi, H., and Gao, Y., *Finite frequency whole mantle P wave tomography: Improvement of subducted slab images*, Geophysical Research Letters, 40(21):5652–5657, 2013. (cited on page 123)

Oldham, R. D., *The constitution of the interior of the Earth, as revealed by earthquakes*, Quarterly Journal of the Geological Society, 62(1-4):456–475, 1906. (cited on page 1)

Paige, C. C. and Saunders, M. A., *LSQR: An algorithm for sparse linear equations and sparse least squares*, ACM Transactions on Mathematical Software (TOMS), 8(1):43–71, 1982. (cited on page 95)

Panning, M. and Romanowicz, B., *A three-dimensional radially anisotropic model of shear velocity in the whole mantle*, Geophysical Journal International, 167(1):361–379, 2006. (cited on page 41)

Pavlis, G. L., Sigloch, K., Burdick, S., Fouch, M. J., and Vernon, F. L., *Unraveling the geometry of the Farallon plate: Synthesis of three-dimensional imaging results from USArray*, Tectonophysics, 532:82–102, 2012. (cited on page 41, 104)

Persson, P.-O. and Strang, G., *A Simple Mesh Generator in MATLAB*, SIAM Review, 46(2):329–345, 2004. (cited on page 89)

Poli, P. and Prieto, G., *Global and along-strike variations of source duration and scaling for intermediate-depth and deep-focus earthquakes*, Geophysical Research Letters, 41(23):8315–8324, 2014. (cited on page 133)

Ren, Y., Stutzmann, E., Van Der Hilst, R. D., and Besse, J., *Understanding seismic heterogeneities in the lower mantle beneath the Americas from seismic tomography and plate tectonic history*, Journal of Geophysical Research: Solid Earth (1978–2012), 112(B1), 2007. (cited on page 41, 104, 128)

Ribe, N. M., Stutzmann, E., Ren, Y., and Van Der Hilst, R., *Buckling instabilities of subducted lithosphere beneath the transition zone*, Earth and Planetary Science Letters, 254(1):173–179, 2007. (cited on page 123)

Rickers, F., Fichtner, A., and Trampert, J., *The Iceland–Jan Mayen plume system and its impact on mantle dynamics in the North Atlantic region: evidence from full-waveform inversion*, Earth and Planetary Science Letters, 367:39–51, 2013. (cited on page 117)

Ritsema, J. and van Heijst, H., *Constraints on the correlation of P and S-wave velocity heterogeneity in the mantle from P, PP, PPP and PKPab traveltimes*, Geophys. J. Int., 149(2):482–489, 2002. (cited on page 40, 42, 71, 103, 112, 113)

Ritsema, J. and Van Heijst, H. J., *Seismic imaging of structural heterogeneity in Earth's mantle: Evidence for large-scale mantle flow*, Science Progress, 83:243–259, 2000. (cited on page 3)

Ritsema, J., van Heijst, H. J., and Woodhouse, J. H., *Complex shear wave velocity structure imaged beneath Africa and Iceland*, Science, 286(5446): 1925–1928, 1999. (cited on page 3, 117)

Ritsema, J., Van Heijst, H., Woodhouse, J., and Deuss, A., *Long-period body wave traveltimes through the crust: implication for crustal corrections and seismic tomography*, Geophysical Journal International, 179(2):1255–1261, 2009. (cited on page 57)

Ritsema, J., Deuss, A., van Heijst, H. J., and Woodhouse, J. H., *S40RTS: a degree-40 shear-velocity model for the mantle from new Rayleigh wave dispersion, teleseismic traveltime and normal-mode splitting function measurements*, Geophys. J. Int., 184(3):1223–1236, 2011, doi: doi: 10.1111/j.1365-246X.2010.04884.x. (cited on page 8, 41, 53, 70, 124)

Ritsema, J. and Allen, R. M., *The elusive mantle plume*, Earth and Planetary Science Letters, 207(1):1–12, 2003. (cited on page 120)

Ritsema, J., van Heijst, H. J., and Woodhouse, J. H., *Global transition zone tomography*, Journal of Geophysical Research: Solid Earth (1978–2012), 109(B2), 2004. (cited on page 41)

Sacks, S., *Diffracted wave studies of the Earth's core: 1. Amplitudes, core size, and rigidity*, Journal of Geophysical Research, 71(4):1173–1181, 1966. (cited on page 43)

Schaeffer, A. and Lebedev, S., *Global shear speed structure of the upper mantle and transition zone*, Geophysical Journal International, page ggt095, 2013. (cited on page 8)

Scheingraber, C., Hosseini, K., Barsch, R., and Sigloch, K., *ObsPyLoad: A Tool for Fully Automated Retrieval of Seismological Waveform Data*, Seismological Research Letters, 84(3):525–531, 2013, doi: 10.1785/0220120103. (cited on page 19, 59)

Scherbaum, F., *Of poles and zeros*, volume 15, Springer Science & Business Media, 1996. (cited on page 27)

Schuberth, B. S. A., Bunge, H.-P., and Ritsema, J., *Tomographic filtering of high-resolution mantle circulation models: Can seismic heterogeneity be explained by temperature alone?*, Geochem. Geophys. Geosyst., 10(5): Q05W03, may 2009a, doi: 10.1029/2009GC002401. (cited on page 3)

Schuberth, B. S. A., Bunge, H.-P., Steinle-Neumann, G., Moder, C., and Oeser, J., *Thermal versus elastic heterogeneity in high-resolution mantle circulation models with pyrolite composition: High plume excess temperatures in the lowermost mantle*, Geochem. Geophys. Geosyst., 10(1): Q01W01, jan 2009b, doi: 10.1029/2008GC002235. (cited on page 3)

Sengör, A., Natal'In, B., and Burtman, V., *Evolution of the Altaid tectonic collage and Palaeozoic crustal growth in Eurasia*, Nature, 364:299–307, 1993. (cited on page 124)

Shapiro, N. M. and Campillo, M., *Emergence of broadband Rayleigh waves from correlations of the ambient seismic noise*, Geophysical Research Letters, 31(7):n/a–n/a, 2004, ISSN 1944-8007, doi: 10.1029/2004GL019491, L07614. (cited on page 26)

Sigloch, K. and Nolet, G., *Measuring finite-frequency body wave amplitudes and travel times*, Geophys. J. Int., 167:271–287, 2006. (cited on page 5, 9, 10, 48, 50, 51, 55, 57, 58, 59, 75, 79, 82, 112)

Sigloch, K., McQuarrie, N., and Nolet, G., *Two-stage subduction history under North America inferred from multiple-frequency tomography*, Nature Geoscience, 1:458–462, 2008. (cited on page 3, 8, 9, 58, 75, 105, 123, 128)

Sigloch, K., *Multiple-frequency body-wave tomography*, Ph.d. thesis, Princeton University, mar 2008. (cited on page 33, 58, 123)

Sigloch, K., *Mantle provinces under North America from multifrequency P wave tomography*, Geochemistry, Geophysics, Geosystems, 12(2), 2011. (cited on page 123)

Sigloch, K. and Mihalynuk, M. G., *Intra-oceanic subduction shaped the assembly of Cordilleran North America*, Nature, 496(7443):50–56, 2013. (cited on page 3, 41, 75, 104, 105, 123, 128)

Simmons, N. A., Forte, A. M., Boschi, L., and Grand, S. P., *GyPSuM: A joint tomographic model of mantle density and seismic wave speeds*, J. Geophys. Res., 115(B12310):1–24, 2010. (cited on page 70, 113)

Simons, F., Nolet, G., Babcock, J., Davis, R., and Orcutt, J., *A future for drifting seismic networks*, Eos, 87(31):305–307, 2006. (cited on page 122, 135)

Stähler, S. C. and Sigloch, K., *Fully probabilistic seismic source inversion–Part 1: Efficient parameterisation*, Solid Earth, 5(2):1055–1069, 2014. (cited on page 50, 69)

Stähler, S. C., Sigloch, K., Hosseini, K., Crawford, W. C., Barruol, G., Schmidt-Aursch, M. C., Tsekhmistrenko, M., Scholz, J.-R., Mazzullo, A., and Deen, M., *Performance report of the RHUM-RUM ocean bottom seismometer network around La Réunion, western Indian Ocean*, Advances in Geosciences, 41:43–63, 2016, doi: 10.5194/adgeo-41-43-2016. (cited on page 135)

Stähler, S. C., van Driel, M., Auer, L., Hosseini, K., Sigloch, K., and Nissen-Meyer, T., *MC Kernel: Broadband Waveform Sensitivity Kernels for Seismic Tomography*, Geophys. Res. Abstracts, 18:Abstract EGU2016–7020, 2016. (cited on page 137)

Stähler, S. C., Sigloch, K., and Nissen-Meyer, T., *Triplicated P-wave measurements for waveform tomography of the mantle transition zone*, Solid Earth, 3(2):339–354, 2012, doi: 10.5194/se-3-339-2012. (cited on page 49)

Steinberger, B., *Plumes in a convecting mantle: Models and observations for individual hotspots*, Journal of Geophysical Research: Solid Earth, 105 (B5):11127–11152, 2000. (cited on page 118, 121, 131)

Su, W.-j. and Dziewonski, A. M., *Simultaneous inversion for 3-D variations in shear and bulk velocity in the mantle*, Physics of the Earth and Planetary Interiors, 100(1):135–156, 1997. (cited on page 40)

Sumy, D. F., Lodewyk, J. A., Woodward, R. L., and Evers, B., *Ocean-Bottom Seismograph Performance during the Cascadia Initiative*, Seismological Research Letters, 2015. (cited on page 135)

T. J. Owens, C. G., H. P. Crotwell and Oliver-Paul, P., *SOD: Standing Order for Data*, Seismol. Res. Lett., 75:515–520, 2004. (cited on page 19)

Tape, C., Liu, Q., Maggi, A., and Tromp, J., *Adjoint tomography of the southern California crust*, Science, 325:988–992, 2009. (cited on page 5)

Tape, C., Liu, Q., and Tromp, J., *Finite-frequency tomography using adjoint methods—Methodology and examples using membrane surface waves*, Geophysical Journal International, 168(3):1105–1129, 2007. (cited on page 6)

Tarantola, A., *Inverse Problem Theory*, Society for Industrial and Applied Mathematics, Philadelphia, 2005. (cited on page 6)

Thomas, C., Garnero, E., and Lay, T., *High-resolution imaging of lowermost mantle structure under the Cocos plate*, J. Geophys. Res., 109:B08307, doi:10.1029/2004JB003013, 2004. (cited on page 112, 124)

Thorne, M. S., Zhang, Y., and Ritsema, J., *Evaluation of 1-D and 3-D seismic models of the Pacific lower mantle with S, SKS, and SKKS traveltimes and amplitudes*, Journal of Geophysical Research: Solid Earth, 118(3): 985–995, 2013. (cited on page 53)

Tian, Y., Hung, S.-H., Nolet, G., Montelli, R., and Dahlen, F., *Dynamic ray tracing and traveltime corrections for global seismic tomography*, J. Comp. Phys., 226:672–687, 2007a. (cited on page 84)

Tian, Y., Montelli, R., Nolet, G., and Dahlen, F. A., *Computing traveltime and amplitude sensitivity kernels in finite-frequency tomography*, Journal of Computational Physics, 226(2):2271–2288, 2007b. (cited on page 5, 86, 87)

Tian, Y., Sigloch, K., and Nolet, G., *Multiple-frequency SH-wave tomography of the western US upper mantle*, Geophysical Journal International, 178 (3):1384–1402, 2009. (cited on page 58, 105)

Tkalčić, H., Young, M., Muir, J. B., Davies, D. R., and Mattesini, M., *Strong, Multi-Scale Heterogeneity in Earth's Lowermost Mantle*, Scientific reports, 5, 2015. (cited on page 115)

Toomey, D. R., Allen, R. M., Barclay, A. H., Bell, S. W., Bromirski, P. D., Carlson, R. L., Chen, X., Collins, J. A., Dziak, R. P., Evers, B., Forsyth, D. W., Gerstoft, P., Hooft, E. E., Livelybrooks, D., Lodewyk, J. A., Luther, D. S., McGuire, J. J., Schwartz, S. Y., Tolstoy, M., Tréhu, A. M., Weirathmueller, M., and Wilcock, W. S., *The Cascadia Initiative: A Sea Change In Seismological Studies of Subduction Zones*, Oceanography, 27, June 2014. (cited on page 135)

Trabant, C., Hutko, A. R., Bahavar, M., Karstens, R., Ahern, T., and Aster, R., *Data products at the IRIS DMC: Stepping stones for research and other applications*, Seismological Research Letters, 83(5):846–854, 2012. (cited on page 23)

Trampert, J., Deschamps, F., Resovsky, J., and Yuen, D., *Probabilistic tomography maps chemical heterogeneities throughout the lower mantle*, Science, 306:853–856, 2004. (cited on page 6)

Tromp, J., Tape, C., and Liu, Q., *Seismic tomography, adjoint methods, time reversal and banana-doughnut kernels*, Geophys. J. Int., 160:195–216, 2005. (cited on page 5, 6)

Vallée, M., Charléty, J., Ferreira, A. M., Delouis, B., and Vergoz, J., *SCARDEC: a new technique for the rapid determination of seismic moment magnitude, focal mechanism and source time functions for large earthquakes using body-wave deconvolution*, Geophysical Journal International, 184(1): 338–358, 2011. (cited on page 50)

van der Hilst, R. H., de Hoop, M. V., Wang, P., Shim, S.-H., Ma, P., and Tenorio, L., *Seismostratigraphy and Thermal Structure of Earth's Core-Mantle Boundary Region*, Science, 315:1813–1817, 2007. (cited on page 112)

Van der Hilst, R., Engdahl, E., Spakman, W., and Nolet, G., *Tomographic imaging of subducted lithosphere below northwest Pacific island arcs*, Nature, 353:37–42, 1991. (cited on page 3)

van der Hilst, R., Widiyantoro, S., and Engdahl, E., *Evidence for deep mantle circulation from global tomography*, Nature, 386:578–584, 1997. (cited on page 3, 4, 75, 123)

Van der Meer, D., Torsvik, T., Spakman, W., Van Hinsbergen, D., and Amaru, M., *Intra-Panthalassa Ocean subduction zones revealed by fossil arcs and mantle structure*, Nature Geoscience, 5(3):215–219, 2012. (cited on page 128)

van der Meer, D. G., Spakman, W., van Hinsbergen, D. J. J., Amaru, M. L., and Torsvik, T. H., *Towards absolute plate motions constrained by lower-mantle slab remnants*, Nature Geoscience, 3(1):36–40, 2010. (cited on page 3, 41, 104, 105, 128)

Van der Voo, R., Spakman, W., and Bijwaard, H., *Mesozoic subducted slabs under Siberia*, Nature, 397(6716):246–249, 1999a. (cited on page 3, 41, 128)

Van der Voo, R., Spakman, W., and Bijwaard, H., *Tethyan subducted slabs under India*, Earth and Planetary Science Letters, 171(1):7–20, 1999b. (cited on page 41, 104, 124, 128)

van Driel, M., Krischer, L., Stähler, S. C., Hosseini, K., and Nissen-Meyer, T., *Instaseis: instant global seismograms based on a broadband waveform database*, Solid Earth, 6(2):701–717, 2015, doi: 10.5194/se-6-701-2015. (cited on page 19, 33, 68, 69)

van Driel, M. and Nissen-Meyer, T., *Optimized viscoelastic wave propagation for weakly dissipative media*, Geophysical Journal International, 199(2): 1078–1093, 2014a. (cited on page 48)

van Driel, M. and Nissen-Meyer, T., *Seismic wave propagation in fully anisotropic axisymmetric media*, Geophysical Journal International, 199 (2):880–893, 2014b. (cited on page 48)

van Hinsbergen, D. J. J., Hafkenscheid, E., Spakman, W., Meulenkamp, J., and Wortel, R., *Nappe stacking resulting from subduction of oceanic and continental lithosphere below Greece*, Geology, 33(4):325–328, 2005. (cited on page 105)

Weber, M. and Davis, J., *Evidence of a laterally variable lower mantle structure from P-and S-waves*, Geophysical Journal International, 102(1): 231–255, 1990. (cited on page 112)

West, J. D. and Fouch, M. J., *EMERALD: A web application for seismic event data processing*, Seismological Research Letters, 83(6):1061–1067, 2012. (cited on page 19)

Woodhouse, J. H. and Dziewonski, A. M., *Seismic modelling of the Earth's large-scale three-dimensional structure*, Phil. Trans. R. Soc. A: Mathematical, Physical and Engineering Sciences, 328(1599):291–308, 1989. (cited on page 42, 53, 103, 112, 113)

Woodhouse, J. and Deuss, A., 1.02 - Theory and Observations – Earth's Free Oscillations, In Schubert, G., editor, *Treatise on Geophysics*, pages 31–65. Elsevier, 2007, doi: http://dx.doi.org/10.1016/B978-044452748-6.00002-X. (cited on page 8)

Woodhouse, J. H., Efficient and stable methods for performing seismic calculations in stratified media, In Dziewonski, A. and Boschi, E., editors, *Proc. Enrico Fermi Int. Sch. Phys., Course LXXVIII*, pages 127–151, Amsterdam, North Holland Publishing Company, 1980. (cited on page 48)

Wortel, M. and Spakman, W., *Subduction and slab detachment in the Mediterranean-Carpathian region*, Science, 290(5498):1910–1917, 2000. (cited on page 105, 123)

Wysession, M. E., *Large-scale structure at the core-mantle boundary from diffracted waves*, Nature, 382(6588):244–248, 1996a. (cited on page 41, 71, 92, 112)

Wysession, M., Fischer, K., Al-eqabi, G., Shore, P., and Gurari, I., *Using MOMA Broadband Array ScS-S data to image smaller-scale structures at the base of the mantle*, Geophysical research letters, 28(5):867–870, 2001. (cited on page 124)

Wysession, M. E., *Imaging cold rock at the base of the mantle: the sometimes fate of slabs?*, Subduction top to bottom, pages 369–384, 1996b. (cited on page 128)

Yang, T., Shen, Y., van der Lee, S., Solomon, S. C., and Hung, S.-H., *Upper mantle structure beneath the Azores hotspot from finite-frequency seismic tomography*, Earth and Planetary Science Letters, 250(1):11–26, 2006. (cited on page 75)

Zaroli, C., Sambridge, M., Lévêque, J.-J., Debayle, E., Nolet, G., et al., *An objective rationale for the choice of regularisation parameter with application to global multiple-frequency S-wave tomography*, Solid Earth, 4: 357–371, 2013. (cited on page 96, 99)

Zaroli, C., Lambotte, S., and Lévêque, J.-J., *Joint inversion of normal-mode and finite-frequency S-wave data using an irregular tomographic grid*, Geophysical Journal International, 203(3):1665–1681, 2015. (cited on page 7, 8, 33)

Zhao, D., *Global tomographic images of mantle plumes and subducting slabs: insight into deep Earth dynamics*, Physics of the Earth and Planetary Interiors, 146(1):3–34, 2004. (cited on page 3, 4, 75)

Zhao, L., Jordan, T., and Chapman, C. H., *Three-dimensional Fréchet differential kernels for seismic delay times*, Geophys. J. Int., 141:558–576, 2000. (cited on page 9)

Zhou, H.-w., *A high-resolution P wave model for the top 1200 km of the mantle*, Journal of Geophysical Research: Solid Earth (1978–2012), 101 (B12):27791–27810, 1996. (cited on page 3, 4, 74)

Zhou, Y., Dahlen, F. A., and Nolet, G., *3-D sensitivity kernels for surface-wave observables*, Geophys. J. Int., 158:142–168, 2004. (cited on page 5)

Zhou, Y., Nolet, G., and Dahlen, F., *Surface sediment effects on teleseismic P wave amplitude*, Journal of Geophysical Research: Solid Earth (1978–2012), 108(B9), 2003. (cited on page 57)

Zhu, H., Bozdağ, E., Peter, D., and Tromp, J., *Structure of the European upper mantle revealed by adjoint tomography*, Nature Geoscience, 5(7): 493–498, 2012. (cited on page 8, 105)

Zielhuis, A. and Nolet, G., *Shear-wave velocity variations in the upper mantle beneath central Europe*, Geophysical Journal International, 117(3):695–715, 1994. (cited on page 105)